THE MANUFACTURE AND APPLICATION OF JOINT-ON-A-CHIP *VIA* 3D BIOPRINTING

CHONGJIAN GAO

MPhil

The Hong Kong Polytechnic University

2025

The Hong Kong Polytechnic University

Department of Biomedical Engineering

The Manufacture and Application of Joint-on-a-Chip *via* 3D Bioprinting

Chongjian Gao

A thesis submitted in partial fulfilment of the requirements for the degree of Master of Philosophy

May 2024

CERTIFICATE OF ORIGINALITY

I hereby declare that this thesis is my own work and that, to the best of my knowledge and belief, it reproduces no material previously published or written, nor material that has been accepted for the award of any other degree or diploma, except where due acknowledgement has been made in the text.

_____ (Signed)

_____Chongjian Gao_____ (Name of student)

The Manufacture and Application of Joint-on-a-Chip via 3D Bioprinting

Abstract

Osteoarthritis (OA), the commonest joint disorder, is a primary cause of chronic disability and pain in the elderly. OA affects over 500 million people worldwide; unluckily, there is no cure for OA till now. With the development of tissue engineering technology, *in vitro* three-dimensional (3D) model provides a new approach for understanding of OA pathology and paves a road for drug discovery. Among these 3D tissue model, organ-on-a-chip attracts lots of research interest due to its high-throughput and reproducible characters. However, pre-existing joint-on-a-chip systems are lacking a circulation system comprising of a blood flow circulation system (nutrient transportation for bone) and a synovial flow circulation system (nutrient transportation for cartilage).

Herein, we design and bio-fabricate a novel prototype of double-circulation joint-on-a-chip *via* 3D bioprinting. To set up this joint-on-a-chip device, we purposely design and synthesize two kinds of bioinks, these are bone/cartilage bioink [methacrylated Alg (AlgMA)/methacrylated ε-polylysine (ε-PLMA)] and blood vessel bioink [granular methacrylated gelatin (G-GelMA)].

1) **Bone/cartilage bioink:**

   The incorporation of ε-PLMA in AlgMA bioinks enhances their operability and stability because of the covalent bonding and electrostatic interaction link between the two components. This improvement surpasses the performance of using single molecular Ca^{2+} or large molecular methacrylated gelatin as a pre-crosslinker. Moreover, the AlgMA/PLMA constructs regulate a charged microenvironment (from -345.25 mV to 121.55 mV) and

exhibit enhanced hydrophilicity (26.64° to 52.00°). As a result, cells within the plotted AlgMA/PLMA structures demonstrate enhanced viability and vitality.

2) **Blood vessel bioink:**

Due to the intermolecular bridge force between each independent microgel, the G-GelMA gain a great rheological property which significantly improve its printability. Furthermore, this physical modification does not change the chemical structure of the polymer chain. In other words, it remains the high biocompatibility of gelatin to provide a cell benefit environment.

After the design of bioink system, we use Rhinoceros to establish the 3D model and related G-code of this joint-on-a-chip. We put bone/cartilage bioink and blood vessel bioink into single-nozzle channel and coaxial-nozzle channel, respectively. Controlled by a computer, the bioprinter process the movement and the pressure on/off to fabricate this chip layer by layer according to the G-code. To support the joint tissue and provide a seamless perfusable chip system, we further design a flow chamber for long-time culture. Finally, through using multichannel bioprinting and coaxial bioprinting techniques, we successfully set up this joint tissue system and correlated flow chamber *in vitro*.

In the future, we will use this joint-on-a-chip system to discover the relationship between endothelial dysfunction and OA pathophysiology. Furthermore, we will conduct drug screening test for potential compounds. We believed that this joint model is a promising start for joint disease study and could be used as a high throughput drug screening platform in future.

Acknowledgements

First, I'd like to show my deepest respect and gratitude to my advisor Dr. Chunyi Wen for his mentoring during my M.Phil. study. I am always inspired by Dr. Wen's creativity and encouraged by his passion. Thanks for his hands-off advising style which allows me to explore my research interest independently. I also grateful for my lab mates: Mr. Jun Liu, Mr. Zhan Li and Ms. Zhou Zou for helping me to start my academic life at PolyU.

Besides my supervisor, I also want to thank my collaborators – Prof. Changshun Ruan for the academic support on my project, taking time to meet with me and also helpful suggestions on my research. Furthermore, I'd like to thank other collaborators in his lab, Dr. Huawei Qu, Dr. Pinpin Wang, Dr. Zhengwei Li, Dr. Kaizheng Liu, Dr. Juan Liu, Ms. Lan Tang and Mr. Shun Li for their technical support on my research project.

Finally, I want to appreciate my parents for their unconditional support. For the last two years, I am too busy to spend enough time chatting with them online. I hope I will be able to share my life with them more often in the future.

Table of Contents

List of Figures

List of Tables

Chapter 1: Introduction

Bone and joint pathology attract lots of research interest, such as osteoarthritis (OA) and rheumatism (RA). OA is among the most usual diseases causing chronic ache and disability, and there is currently no cure. It has been all along defined as a wear-and-tear disorder, but now is recognized to own a complicated pathophysiology influencing multiple joint structures.

In vitro three-dimensional (3D) organ models have received widespread attention for it can significantly reduce costs and shorten preclinical research time on drug screening and biological mechanisms. The Food and Drug Administration (FDA) of U.S. included organ-on-a-chip as a "non-animal" verification method into the relevant legislation of the independent non-clinical evaluation system of drugs in June 2022. Aiming to provide new strategies for OA's treatment, in recent years, researchers have begun to study the disease mechanism of OA in *in vitro* 3D joint models. Due to the complexity and diversity of joint tissues, there is still a big gap between the current joint organ model and its real microenvironment. Key scientific issue that needs to be solved is ***how to construct a highly bionic 3D joint models with dual circulation system, that are blood and synovial flow from two dimensions: structure and mechanics***.

For the construction of a highly bionic 3D joint model, reproduction of the complex joint microphysiological environment through appropriate technology is a major challenge. There are many types of *in vitro* models used in biomedical research, such as microfluidic-based organ-on-a-chip (2D), organoids (2.5D), and bioprinted tissue (3D). However, neither microfluidic chips nor organoids can be extended to 3D microenvironments and lack fluid mechanics stimulation, making them unable to be used for large-scale organ simulation of complex cellular microenvironments.

At present, the rapidly developing 3D bioprinting technology can realize the spatial distribution of multi-cells, providing new technical support for the construction of highly bionic in vitro 3D organ models. However, there are still huge challenges in how to use 3D bioprinting technology to build a highly bionic joint-on-a-chip (JOC) with ***dual circulation systems of blood and synovial flow***. The key lies in how to efficiently establish these two circulation systems and rationally plan ***independent zone*** and ***substance exchanging zone***. Blood and synovial fluid are efficient pathways for connecting bone tissues and cartilage tissues for JOC: On the one hand, vascular channels and synovial fluid chambers are the main nutrient supply pathways for bone tissue and cartilage tissue, respectively. Among them, compared with the penetration of nutrients from the blood vessels of the subchondral bone, the cartilage's direct nutrition from the synovial fluid is also very important. On the other hand, during the occurrence and development of OA, blood and synovial flow not only exchange nutrients and waste products through the synovial membrane, but also exchange biological signals.

In this thesis, we described a 3D bioprinted JOC system *in vitro* which could overcome key technical problems that we mentioned. First, we designed two kinds of bioinks for bone/cartilage tissue and blood vessel reconstruction. Second, we designed a JOC model with double flow system - blood flow and synovial flow. Third, we set up a multi-channel 3D printing system with multi-nozzle for bone/cartilage tissue and co-axial nozzle for vessel channel. In the future, this JOC model could be used for disease pathology research and drug screening applications.

1.1 Current Understanding of Osteoarthritis

Bone and joint disease pathology attracts lots of research interest, such as osteoarthritis (OA) and rheumatism (RA). OA is the most well-known joint disorder, plaguing appropriate more than 240 million individuals all over the world.[1] Not until the end of 18th century, OA was recognized as a new joint disease other than RA.[2] Now, OA has been recognized as a wear-and-tear disorder for a long time, but now is recognized to own a complicated pathophysiology influencing multiple joint structures [3] (**Figure 1-1A**), as concluded by the ***Osteoarthritis Research Society International definition of OA***: "The disease manifests first as a molecular derangement (abnormal joint tissue metabolism) followed by anatomic, and/or physiologic derangements (characterized by cartilage degradation, bone remodelling, osteophyte formation, joint inflammation and loss of normal joint function), that can culminate in illness."[4]

In summary, OA has been defined focusing on not only the changes in the articular cartilage, but also the alterations on subchondral bone/meniscus and osteophyte formation.[5] Development of OA is always slow and may take few years to form sensible pain. Therefore, the understanding of risk factors for OA and related prevention is important.

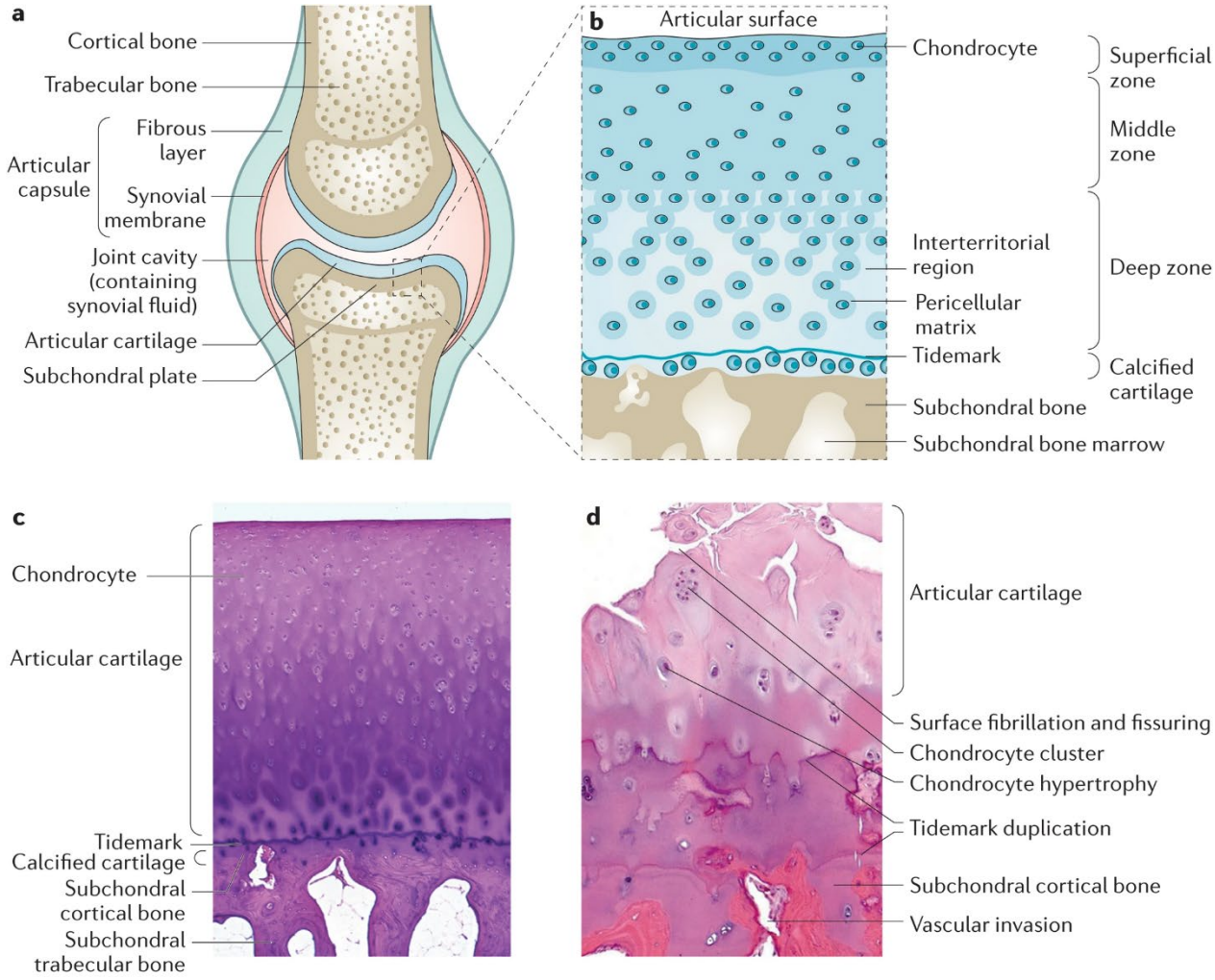

Figure 1-1. Health and OA Knee Joints. A) Schematic structure of the joint. **B)** Schematic view of articular surface cross-section. **C)** Histopathological view of a health articular surface's cross-section. **D)** Histopathological view of a OA articular surface's cross-section. Adapted with permission from reference [2].

1.1.1 Risk Factors of OA

Obesity: Fat is a well-known risk factor. For example, each individual having a body mass index (BMI) over 25 $kg \cdot m^{-2}$ may have a high risk ratio on hand OA, that is 1.9.[6] For a long time, the connection between obesity and OA has been seen as excessive joint bearing, especially for knee. In contrast, this can't explain the OA developing with non-weight-loading joints. For weight-loading joints, e.g., knee, the body fat has already been seen as a useful forecaster of alteration of

cartilage.[7] Furthermore, according to epidemiological analysis, individuals with higher BMI have a threefold to fourfold higher risk on knee and hip joint replacement.[8]

Physical Activity: Physical activity has been seen as a burden for weight-loading joints historically. However, more evidence has shown that the physical activity, particularly joint involving, plays a significant role on maintaining and developing healthy knee joints. For instance, a study showed that the physically active children had a larger cartilage volume than sedentary children.[9] In addition, the rapid loss of cartilage volume was investigated among adults with immobility.[10] Both of them show that moderate physical activity is good for joint.

It remains unclear that whether physical activity is bad or good for adults' joint. This is because current evidence from adults is conflicting, e.g., vigorous physical activities not only increase knee OA risk for patients with established OA, but also have a positive effect on knee articular cartilage in healthy people.[11, 12] Moreover, people with different baseline cartilage volume have different feedback under heavy physical activity. Individuals with higher baseline cartilage volume can slow the rate of their cartilage loss, while individuals with lower baseline cartilage volume may expedite their cartilage loss.[13]

Structural Factors: Structural abnormalities of hip bones are commonly found in OA patients. This abnormality is also grouped into hip dysplasia and femoroacetabular impingement which may cause a concentration of weight-bearing area.[14, 15] Not only the obvious dysplasia is a common recognized risk factor, even subtle degree of dysplasia may increase the risk of hip OA.

Besides the congenital structural abnormalities, structural joint damage by modifiable developmental exposure can also increase the risk of OA.[16] Clinical reports have shown that

over-sporting before the close of growth plates would highly increase the risk of femoroacetabular impingement which may leads to hip OA.[17-19] A theory has been developed for this phenomenon that repetitive joint loading on bones may cause rapid growth leading to a joint structural modification.[20] However, some research also showed that the importance of early occupational exposure. In a study, fewer structural changes of hip joint were observed in their late life, if they involved in heavy lifting when that are 18-30 years old.[21]

Genetics: For hand and spinal OA, strong evidence of genetic factors involving has been found [22, 23], while the evidence has not been found for knee OA.[24, 25] These classic twin studies and familial aggregation research indicated that, by controlling most common risk factors, the genetic susceptibility of structural OA is located between 40% and 65%.[24, 25] Recently, Genetic, epidemiological and genome-wide association studies have assisted us on identifying several genetic variants associated with hip or knee OA. These identified genes have been seen as an important role involving in molecular mechanisms of OA pathogenesis.

1.1.2 Pathophysiology of OA

Cartilage development and Degeneration: There is no proliferation for chondrocyte under a normal physiological period of an adult. The most important role of chondrocyte is to refresh the hydrophilic glycosaminoglycan (GAG) which could provide tensile strength.[26, 27] Chondrocytes are embedded in a mixture of matrix, e.g., type VI collagen, which could help them stay in a low-turnover state.[28-30] During the development of OA, the composition and structure of the matrix changes a lot. Starting from the appearance of surface fibrillations, the matrix breaks to show deep fissures and expose the underlying cartilage and subchondral bone.[31-33] Then, vascularization

happens in osteochondral interface, vascular network generate from bone marrow and pass through subchondral bone and invade into calcified cartilage.[32] This vascularization in cartilage will promote endochondral bone formation.[34, 35] To stop this degeneration progress, chondrocytes will increase its synthetic activity at early stage of OA.[36] However, the exposure of the chondrocyte to the deep-side matrix will deregulate the function of chondrocyte.[30] With the development of this disease, the collagen network is eroded and the whole disease get into an irreversible stage. This progress is associated with several kinds of enzyme [37, 38] and their related inflammatory pathways.[39, 40] After that, many senescent chondrocytes will increase the secretion of pro-inflammatory products, e.g., reactive oxygen species.[41] In the end, most of the chondrocytes will show characters related to hypertrophy.[42] These inflammatory factors will continuously stimulate other tissue zone in joint and form an OA physiological environment.

Subchondral Bone Homeostasis and Disorder: The structure and composition of bone maintain a balance throughout an individual's life by controlling two kinds of osteocytes, that are osteoblasts and osteoclast. Osteoblasts normally produce new bone, while osteoclasts absorb bone in reaction to biomechanical and biochemical factors in joint environment.[43-45] When OA happens, the volume of the cortical plate increases, and bone mineralization occurs.[46-48] Moreover, bone could be directly damaged from physical factors, and form microcracks which may enhance the process of OA.

It worth to note that evidence of anatomical relationship between bone changes and the development of cartilage OA has been found, mechanical and structural changes for both bone and cartilage are harmful.[49-51] For example, Radin *et al.* and Brown *et al.* proposed that the stiffness of subchondral bone acts an important role in the OA development.[51, 52] However, Day et al.

argued that owning to the lower bone mineral density, the stiffness of subchondral bone decreases instead of increasing.[53, 54] Their speculation is the reduction of bone modulus cause a cartilage deformation, contributing directly to the development of OA pathophysiology. This argument indicated that the complexity of their relationship, which are still an unclear question now.

Synovial Membrane/Fluid and Inflammation: The synovial membrane is a thin but compact cellular layer used to form a seamless and on-demand molecular joint environment. Cartilage gets nutrient and lubricant factors from synovial fluid through synovial membrane. One of OA common features is synovitis which is associated with diffusion and perivascular infiltration of T and B lymphocytes.[55] A positive correlation between synovitis and OA risk has been set up by using imaging studies based on MRI.[56-59]

The damage of cartilage has a close relation with the development of synovitis. As I just mentioned in previous section, the cartilage degradation products promote the production of pro-inflammatory molecules.[60] OA patients' protein and gene analysis indicated the upregulated expression of molecule associated with angiogenesis and inflammation. The Toll-like receptors (TLRs) are responsible for the immune system activation.[61] Inflammatory related proteins and cytokines could be found from synovial fluid, synovial membranes and cartilage in OA patients' tissue.[62, 63] Some marker, e.g., interleukin (IL) family and tumour necrosis factor (TNF), has been identified a increasing in synovial fluid and joint tissue from OA patients.[64] For instance, IL-8 which has a lot of receptors on chondrocytes is widely detected in OA patients' synovial fluid.[65-67] This implicates a potential relation between OA pathogenesis and synovial inflammation.

Adiposity and Inflammation: There is a speculation that adipokines induce pro-

inflammatory cytokines in synovial membrane and cartilage tissue. As we mentioned before, such pro-inflammation will lead to a cartilage damage and subchondral bone remodelling.[68] Studies have been conducted to support this hypothesis, increased injection of adipokines are associated with the cartilage loss.[69, 70] Besides the systemic effects, local effects of adiposity were also observed, such as the increased fat caused a strong knee cartilage loss.[71, 72]

Vascular Aetiology Hypothesis: Similar with the risk factor – mechanical loading, hypertension also contributes to the development of the OA pathogenesis.[73] Vascular network works as a transportation system in human body, the hypertension can break the homeostasis in joint environment (**Figure 1-2**). Hypertension may affect the perfusion of subchondral bone by increasing the intraosseous pressure which is negatively correlated with intraosseous blood flow.[74-76] The disruption of blood flow can also trigger hypoxia and nutrient deprivation which may affect the metabolic homeostasis of bone and cartilage.[77] Then irreversible damage will happen on bone and cartilage, such as osteonecrosis [78], bone marrow oedema [79], bone sclerosis [80], osteochondral junction modification [48, 81] and joint effusion [82]. Moreover, hypertension and OA shared some molecular pathways, such as Wnt–β-catenin signalling [83, 84]. The activation of Renin–angiotensin system [85, 86] and endothelin system [87] can potentially control the development of OA.

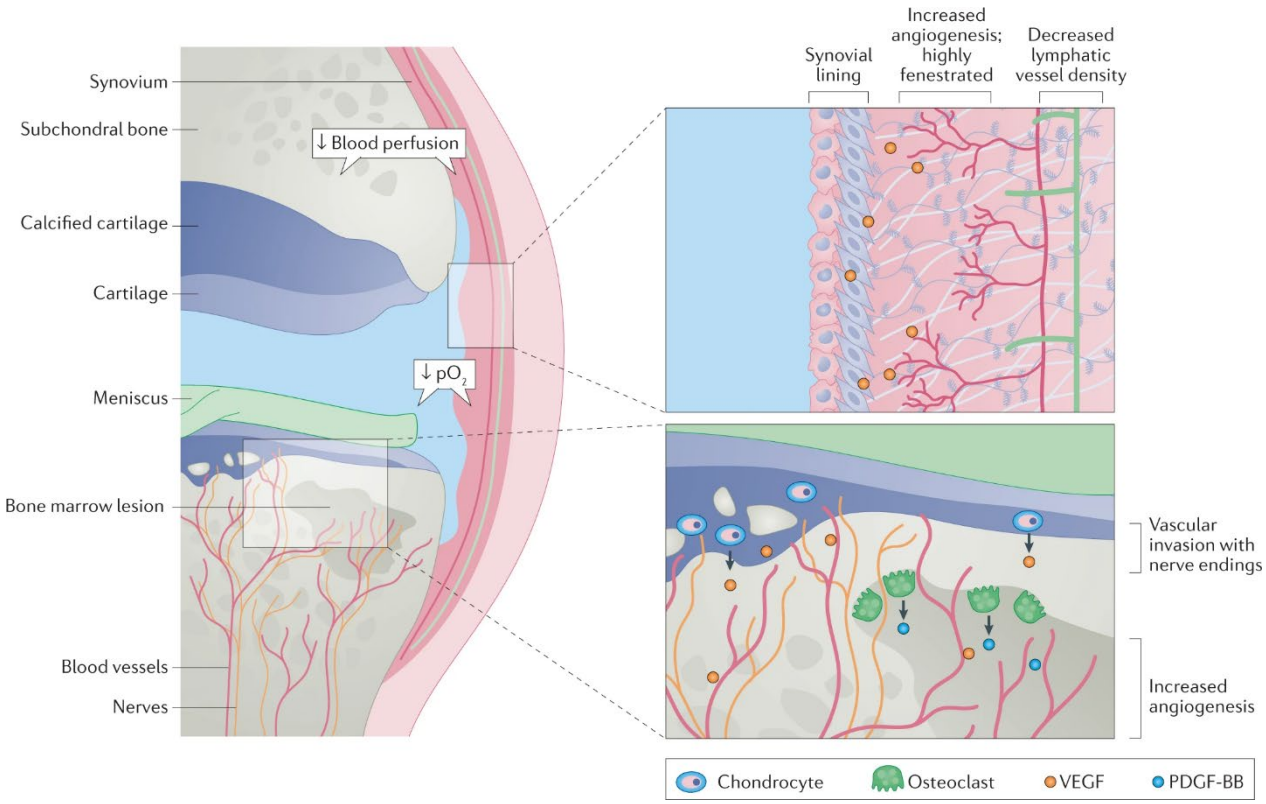

Figure 1-2. Vascular Aetiology Hypothesis: The Changing of Vasculature and Knee Osteoarthritis. Adapted with permission from reference [73].

1.2 Joint-on-a-Chip and Biofabrication Technology

To understand the pathology and find possible treatment, scientists start to study such disease in three-dimensional (3D) model. There are many types of 3D model for biomedical research, such as organ on a chip (based on microfluidics), organoid and so on.[88-94] However, for both organ on a chip and organoid, they both have weakness that could be not be used in large tissue mimicking which needs complex cell microenvironment.[95] For instance, the joint has a very complex cell distribution in microscale. Usually, the cartilage zone does not have blood vessels for nutrients, it gets nutrient from synovial flow for instead. To mimic the joint microenvironment, scientists should combine both synovial flow and blood flow simultaneously. This is impossible

for organoid which is basically a cell aggregate that is hard to introduce two external flows into it. And the lack of internal vascular network will also prevent the cell aggregate from growing bigger.[94, 96] Although for the organ on a chip which is based on microfluidics, the external flow could be easy to add. However, the cells in these chips are always located in 2D pattern which is quite different with the cells circumstance in vivo.[90, 91, 97] For example, the cartilage has three different zones, and each zone has their different cell distribution as shown in **Figure 1B**.

Recent years, 3D bioprinting, as one of the important branches of additive manufacturing technology, has made great achievements in the field of functional tissue/organ biological manufacturing (**Figure 1C**). 3D bioprinting is to use bio-ink composed of biomaterials, cells and biological factors to accurately control the spatial distribution of bio-ink through computers, aiming to print artificial tissues/organs with personalized macro and micro 3D structures and specific biological functions. It is a new field of interdisciplinary integration of life science, material science, manufacturing science and other disciplines, and has significant advantages in the manufacturing of tissues and organs.

For biomanufacturing organ in vitro, it is vitally important to mimic the vascular channel structure to enable its internal material transmission, maintain cell survival and function, and thus form tissue/organ function.[98] In the past decade, researchers have invent several methods to build the shape of blood vessel network for bioprinting, such as extrusion 3D printing[99-101], printing vascular frame injection mold[102, 103], light curing technology (stereolithography and laser ablation)[104-106], post processing of printing template[107], writing in support bath[108-112], coaxial extrusion printing[113] and so on.

Among them, light curing technology has the characteristics of high precision, and has

shown great potential in building micro sized complex organ structures.[114] However, due to the scattering of light and the diffusion effect of free radicals, it is necessary to slice the model into "ultra-thin" slices to eliminate the lamination in the manufacturing of irregular structures.[104] Not only that, due to the limitation of printing mode, “lift clean peel” and other repeated operations should be carried out after each layer is built, which often takes ten hours or more to manufacture large-size structures. When multi-component printing is involved, in addition to the above steps, each material of each layer needs to be cleaned and replaced with the next material after construction.[115] This will make the construction of multi-component structures take more time, which is often unacceptable in biological printing containing cells. In contrast, extrusion 3D printing technology has more advantages in the construction of large-scale biological manufacturing system composed of multi cells and multi materials, such as convenience, time-saving and space limitation. In the process of extrusion 3D printing, the layer height depends on the needle diameter and moving speed, and the next layer can be directly manufactured after one layer is built. Multi material printing can also be realized by quickly changing the printing channel, which greatly saves the manufacturing time. Prof. Jennifer A. Lewis of Harvard University proposed multi-material multi-nozzle 3D (MM3D) printing, which shows its ability to conduct multi-component 3D construction through MM3D printing heads with high switching frequency. The printing efficiency is improved by arraying needles, which further improves the efficiency of extrusion 3D printing. This printing technology can build a soft robot “millipede walker” in 17 minutes, but the possibility of biological printing still needs to be verified.[99]

Obviously, additive manufacturing based on traditional extrusion 3D printing can meet the needs of multi-component complex structure. However, when printing the radial multilayer

structure, it is necessary to frequently replace the material channel for filament deposit of different components, which will waste a lot of time and greatly reduce the viability of cells.[116] Therefore, the researchers further introduced the coaxial printing nozzle and proposed the extrusion coaxial printing method to construct the core-shell vascular like structure. Prof. He Yong's team from Zhejiang University constructed a stable scaffold with tubular structure connected through coaxial bioprinting technology.[117] By introducing a needle inside the existing needle, the coaxial form with two needle axes coincident is formed. From the cross-sectional view, the inner circular structure is added with a layer of ring structure around it, which naturally forms a "core-shell" structure in the extrusion process.

Here, in this research, we report a prototype of joint-on-a-chip *via* 3D bioprinting. We integrate both blood flow and synovial flow into this chip. Due to the use of coaxial 3D printing technology, we could establish the crosstalk between blood and synovial flow. This new type of joint on a chip could provide a new approach for joint disease research.

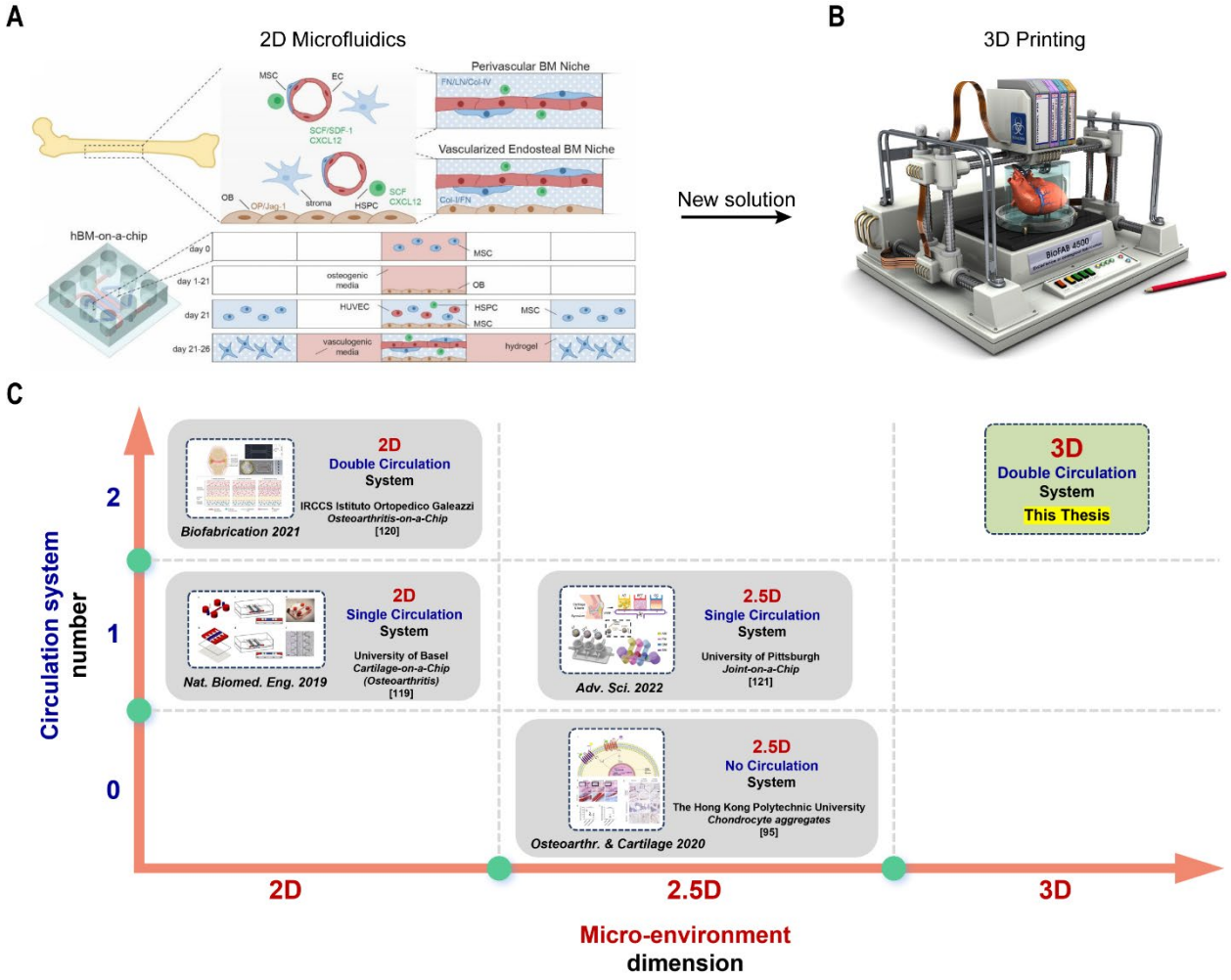

Figure 1-3. The Research Background of This Project. A) The traditional technology for manufacture 2D model of joint *in vitro*. **B)** The new technology for manufacture 3D model of joint *in vitro*. **C)** Current Milestone related to Joint-on-a-Chip. Adapted with permission from references [95] and [118-121].

Table 1. Current Milestone related to Joint-on-a-Chip.

No.	Institute	Milestone	References
1	University of Basel	2D “cell level” single circulation system	[118]
2	IRCCS Istituto Ortopedico Galeazzi	2D “tissue level” double circulation system	[120]
3	Georgia Institute of Technology	2.5D “cell level” single circulation system	[119]
4	University of Pittsburgh	2.5D “tissue level” single circulation system	[121]

Chapter 2: Design of Joint-on-a-Chip

2.1 Introduction

The 3D structure of the chip was designed through software. Normally, the design and arrangement of joint-on-a-chip starts from a single 2D pattern. After enough checking, the scheme of the joint-on-a-chip will be prompt into a detailed 3D structure with specific parameters.

2.2 Materials and Methods

In order to build up such a 3D printed chip model. First, we decided the Length, width and hight of the join-on-a-chip through the actual size parameter from human or experimental animals (**Figure 2**). Second, we chose the appropriate radius of the bone and cartilage zone (**Figure 2**). Third, we decided the diameter of the blood vessel channel. This step has a high related relationship with ***Flow Dynamic Analysis*** part in following research. Flow Dynamic Analysis part plays a feedback role in the chip design, if the diameter of the blood vessel is not appropriate, a new parameter will be generated until a suitable one is selected. The general method is shown as follow, based on the multi physical field simulation software ***COMSOL***, the fluid flow simulation of the blood vessel channel model was carried out: first, the 3D chip model was imported into ***COMSOL*** software as an STL file, and then the model was meshed. Then, the fluid flow mode was set as laminar flow, and the input and output ends of the vascular model were set respectively. Finally, the fluid flow simulation calculation of the model was completed; Through the simulation results, the overall and local flow effects of the vascular model were evaluated. Finally, the optimized

vascular network model was imported into the parametric design software Rhino, and the G-codes

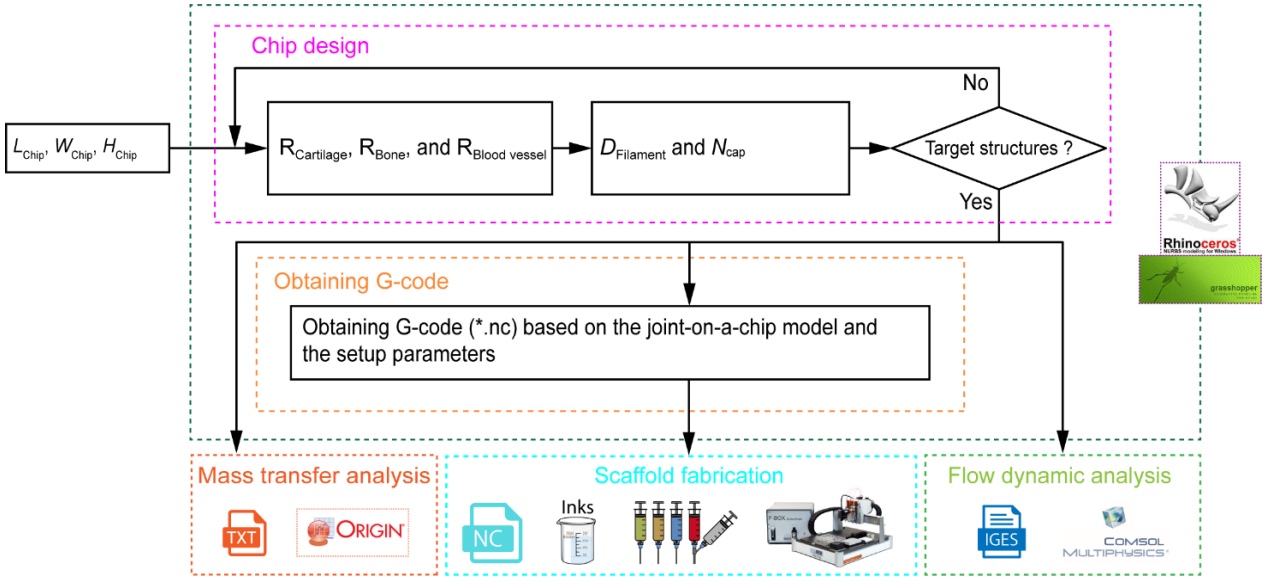

code is obtained for the construction of the joint on a chip.

Figure 2. The Design Protocol of the Joint-on-a-Chip.

2.3 Results and Discussion

2.3.1 Structure of Joint-on-a-Chip

To mimic the structure of the joint, we design a symmetrical chip as follow (**Figure 3A**). First, it has double circulation system, those are blood circulation system and synovial circulation system, for nutrient supply and providing shear force effect. The nutrient could diffuse from blood vessel and synovial flow to bone structure and cartilage structure, respectively. In addition, this double circulation system has a direct connection in the chip, which could mimic the mass transition (this zone is also called as "***Matter Exchange Zone***") in the synovial membrane between blood vessel and synovial flow (**Figure 3A**).

In order to avoid the direct connection between cartilage and blood vessel, we embedded

the blood vessel channel into the bone zone (this zone is also called as "***Independent Zone***"). In this situation, the cartilage zone could get most of its nutrient from synovial flow and few from the diffusion of blood vessel. And this is what real joint environment like.

After printing, this chip will be moved into a chamber which is link to a perfusion system. This chip will be cultured in the incubator for future experiment (see **Figure 3B**).

In addition, to mimic the structure of the cartilage [122], we design a three-zone printing area as shown in **Figure 3C**. Through using the extrusion-based printing technology, two parallel curvy filaments and a series of radial filaments could be deposited on the printing platform.

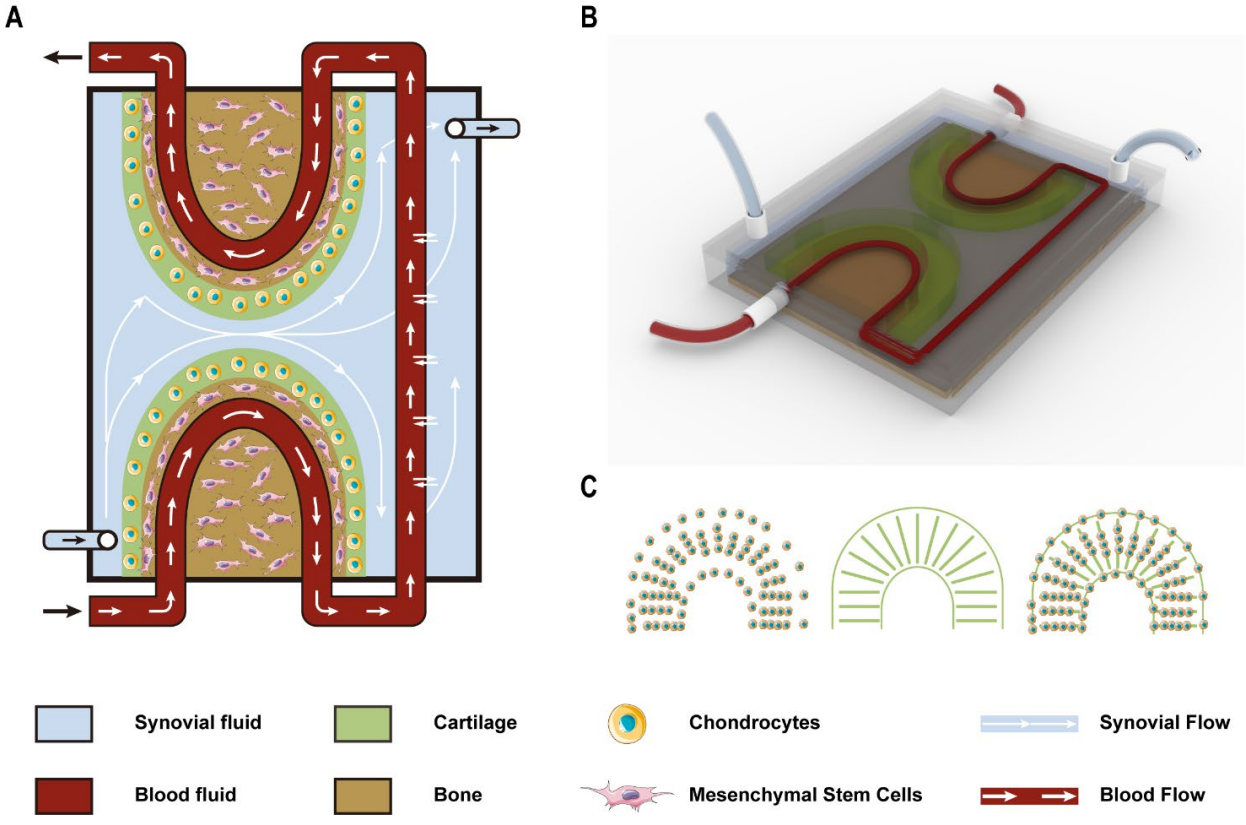

Figure 3. The Design of the Joint-on-a-Chip. A) The diagram of joint-on-a-chip. **B)** The different zones of this joint-on-a-chip (in a perfusable chamber). **C)** The three zones of Chondrocytes' distribution.

2.3.2 Flow status in Chip

Through using COMSOL Multiphysics, we analysed the flow condition of blood vessel channel and synovial flow chamber (**Figure 4**). The flow velocity in the blood vessel channel was stable and present laminar flow (**Figure 4A**). The flow distribution in synovial chamber were more complex. The flow velocity in the narrow gap between two cartilage zone was higher than the cartilage of other side. This could mimic the high shear force in the junction of femur bone and tibial bone (**Figure 4B**).

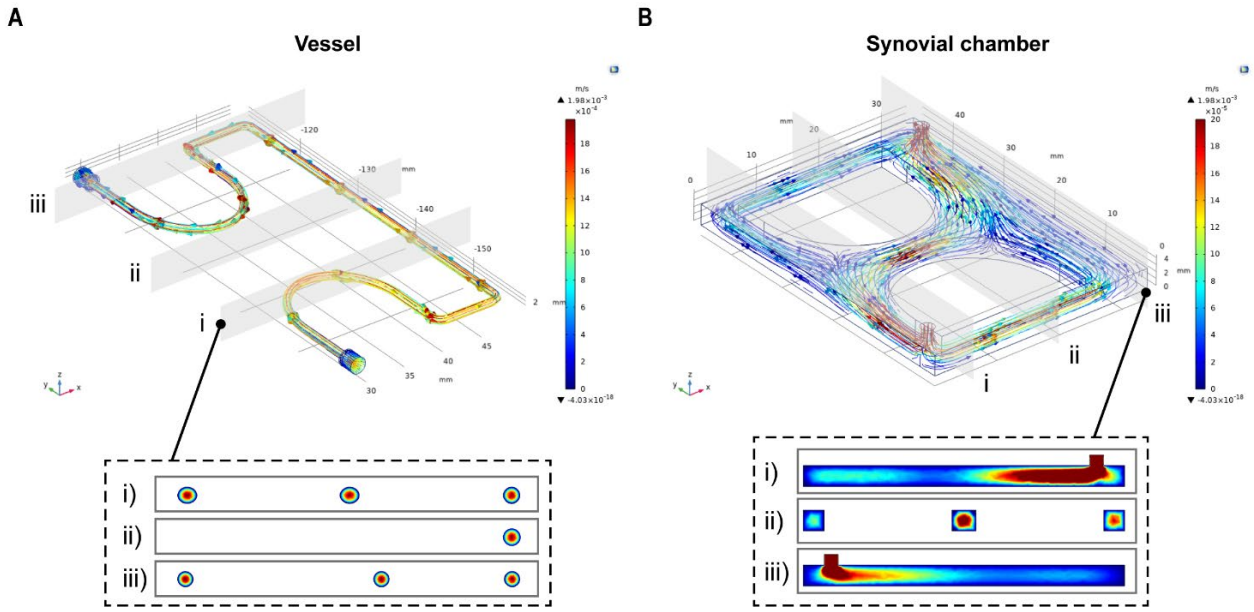

Figure 4. The Flow Simulation of Joint-on-a-Chip. A) Vessel channel flow simulation. **B)** Synovial chamber flow simulation.

Chapter 3: Biofabrication of Joint-on-Chip

3.1 Introduction

When it comes to biological additive manufacturing, the widely preferred method is extrusion-based bioprinting, primarily because of its ability to efficiently produce large-scale structures and quickly construct objects using multiple materials [99, 114, 123-125]. Printability and biocompatibility are considered the two crucial qualities of bioink, as it serves as a carrier and creates a biocompatible microenvironment for cells immediately post-plotting. Due to its good biocompatibility, hydrogel is a common ink material in bioprinting.[125] Moreover, most of the non-chemically crosslinked hydrogel precursors have the rheological properties required in extrusion 3D printing: shear thinning and self-healing properties. In this research, we designed two kinds of bioink for cartilage/zone part and blood vessel part, respectively. [Alginate (Alg) based bioink: Methacrylated Alg and methacrylated ε-polylysine (ε-PLMA) blend bioink; Gelatin (Gel) based bioink: Granular Methacrylated gelatin (G-GelMA) bioink.]

In the second part of this chapter, we described detailed protocol for bioprinting each part of the tissue zone. As we mentioned before, the vascular circulation system is constructed through coaxial bioprinting, and the joint synovial fluid circulation system is constructed through chip encapsulation. A sample was constructed for testing to verify the consistency between the double-circulation system. Through testing, it is confirmed whether the chip structure's material transmission capacity, mechanical response and other parameters are in line with expectations, and feedback is given to the design end for structural adjustment. Through multiple feedback adjustments and verifications, the bone joint chip construction of the dual circulation system is

realized and meets the needs of "***Independent Zone***" and "***Matter Exchange Zone***".

3.1.1 Bone and Cartilage Bioink

Thanks to their similar character to extracellular matrix (ECM), natural-sourced hydrogels, from plant or animal resources [e.g., alginate (Alg), silk, and gelatin (Gel)], are widely used as bone bioinks. Among them, Alg is widely used for its excellent mechanical properties and low price. Human bone marrow mesenchymal stem cells (hBMSCs) were encapsulated into Na-alginate ink by Fedorovich *et al.* [126], and the cell viability in the extrusion-bioprinted scaffolds can achieve more than 90%. To further expand the potential of using, Jeon *et al.* [127] cryopreserved hBMSCs by Alg microgel bioink. The freezing process did not affect the bioactivity and differentiation potential of hBMSCs after recovery. This means that the bioink does not need to be prepared and used straight away, realizing the need of long-period biological storing and bioink utility according to demand. Moreover, alginate has been selected to work as a thickening content in mixed bioink for its high printability. For example, Zhang *et al.* [128] bioprinted sodium alginate-based bioink which has human umbilical vein smooth muscle cells, and fabricated vasculature catheters *via* coaxial nozzles extrusion plotting. However, Alg-based bioinks' original bio-inertness inhibits cellular interactions in the bioprinted scaffolds [129].

To address these limitations, researchers have developed two types of approaches: incorporating bioactive units into the material through modification [130], and blending bioactive components [131-134]. The most commonly used method for bioactive modification is RGD-grafting, which effectively promotes cell adhesion and can selectively target specific cell lines, eliciting desired cell responses [135]. However, modifying RGD peptides does not alter the

rheological properties of alginate, which necessitates using high concentrations as bioink. Additionally, the low stability of Ca^{2+}-crosslinking over extended culture periods hinders the advancement of Alg-based bioinks. To overcome these challenges, researchers have explored blending bioactive pre-crosslinkers with alginate, with methacrylated gelatin (GelMA) being the most prevalent option. GelMA, a large molecule with bioactive sites like the RGD group, forms electrostatic forces and interpenetrating double networks with Alg, significantly enhancing the printability and mechanical properties of the bioink [136, 137]. However, the blending process requires an extended stirring time to achieve uniform cell distribution and prevent blockages in the nozzle due to the two large molecule polymers. Unfortunately, prolonged exposure to shear stress during this process inevitably reduces cell vitality and viability [138]. Consequently, the ability to fabricate large-scale structures is restricted by the production of a substantial volume of bioink in a single operation.

Recently, there is a hot focus on polyelectrolyte-based pre-crosslinking materials in the field of 3D bioprinting research. These materials involve the combination of cationic (+) and anionic (-) inks, allowing for the tuning of the polyelectrolyte ink's synergistic properties [139]. By adjusting the ratio of cationic and anionic components, the charges of the polyelectrolyte ink can be modified, creating a biologically friendly microenvironment. This is particularly promising for 3D bioprinting applications since many human organs and tissues, such as the skin, blood vessels, heart, and nerves, exhibit electrical sensitivity. For instance, Wang *et al.* [140] successfully created biodegradable and injectable hydrogel by blending opposite charged gelatin nanospheres. Inspired by this approach, our research group developed a polyelectrolyte ink using alginate and ε-polylysine (ε-PL) [141]. Through electrostatic interactions, the polyelectrolyte ink can be used to

fabricate huge self-supportable constructs at room temperature. Furthermore, the surface of the scaffold can be further enhanced by applying a coating of ε-PL which would improve cell adhesion. Alternatively, it is important to note that cells cannot be added within this polyelectrolyte bioink for its bio-toxic post-crosslinking process involving N-hydroxy-succinimide (NHS) and 1-ethyl-3-(3-dimethylaminopropyl) carbodiimide (EDC) treatments.

In this thesis, I have developed a bioink based on a photocrosslinkable polyelectrolytic methacrylated Alg (AlgMA), and I have introduced methacrylated ε-PL (ε-PLMA) as a polycationic small molecular crosslinker (**Figure 6A**). The use of photo-crosslinking enables precise control over the material's reaction behavior in both space and time, which is advantageous for fabricating 3D structures [142]. Additionally, light-based chemistries are known for their high efficiency and minimal byproduct formation, making them well-suited for fabricating biocompatible structures that contain alive cells [142]. The incorporation of ε-PLMA, with its small molecular weight and extremely good water solubility, allows for the preparation of the bioink with a fast stirring of no more than 10 seconds. Moreover, this bioink exhibits improved printability (**Figure 6B**) for the electrostatic correlation between ε-PLMA and AlgMA. After the bioink was printed, the cell-laden scaffolds could be reinforced through photo-crosslinking, resulting in enhanced shape stability compared to scaffolds crosslinked through ionic interactions. Subsequently, we systematically evaluated the AlgMA to ε-PLMA ratio based on electrical properties, mechanical properties, rheological properties, and most importantly, cytocompatibility. This comprehensive screening process led to the identification of the optimal formulation.

3.1.2 Vessel Bioink

For vessel bioprinting, the biomaterials' biocompatibility is very significant. Due to the high biocompatibility of natural sourced hydrogel, alginate/gelatin-based biomaterials are commonly used in vessel fabrication.[143-145] However, the low biocompatibility of alginate and low printability of gelatin makes it difficult to get a cell-laden hydrogel tube with high strength.[146] Blend bioink were carried out to solve the problem, for instance, Pi *et al.* used a blend bioink consisted of GelMA, alginate and poly(ethylene glycol) (PEG) acrylate with tripentaerythritol core (PEGOA) to build up a tough hydrogel tube.[143] However, the over-use of high concentration hydrogel will cause a high density of polymer network.[147] As a result, the transportation efficiency of nutrient and waste was limited by the compact hydrogel wall. Recently, granular materials attracted a lot of attention for its unique rheological behavior and high permeability. Granular gelatin-based bioink has been introduced and showed great increase on viscosity and shear-thinning behavior.[148] However, the lack of inner-crosslinking between different microgel affects the mechanical properties of this kind of bioink.[148]

Herein, we designed a new kind of granular GelMA (G-GelMA) bioink which has an excellent printability and high biocompatibility. GelMA microgel was dissolved into GelMA solution to form this granular bioink. The rheological test and mechanical test were performed to show the physical properties of this materials. Finally, we also reported the printability and biocompatibility on coaxial bioprinting of G-GelMA.

3.2 Materials and Methods

3.2.1 Synthesis of Bone/Cartilage and Vessel Biomaterials

Synthesis of AlgMA: Begin by dissolving Alg (from Sigma-Aldrich, Inc.) in phosphate

buffered saline (PBS). Next, while keeping the mixture in an ice bath, gradually add the MA solution to the Alg solution, ensuring the addition is done drop by drop, and allow the mixture to react in darkness for 48 hours. Throughout this reaction, maintain the pH value between 7 and 8 through carefully dropping NaOH solution. Upon completion of the mediation, introduce absolute ethanol to the mixture to cause the AlgMA to precipitate. Subsequently, collect the AlgMA through centrifugation, and redissolve it in double distilled water (ddH_2O). Transfer the AlgMA solution into a dialysis bag and subject it to dialysis for 72 hours. Following dialysis, freeze the AlgMA solution by placing it in an ultra-low temperature freezer for 12 hours. To finalize the process, lyophilize the solid AlgMA for 72 hours to acquire the final product — AlgMA.

Synthesis of ε-PLMA: Begin by preparing a solution of ε-PL (from Macklin, Inc.) in PBS. Next, while keeping the mixture in an ice bath, slowly add a solution of methacrylic anhydride (MA, from Sigma, Inc.) to the ε-PL solution, ensuring that the addition is done dropwise. Allow the mixture to react in the dark for 6 hours, maintaining a pH value between 7 and 8 throughout the reaction. Once the reaction is complete, centrifuge the solution to remove any precipitate formed. Transfer the clear reaction solution into a dialysis bag and subject it to dialysis for 72 hours. After dialysis, freeze the solution in a -80 °C freezer for 12 hours. Lastly, lyophilize the frozen solution for 72 hours to yield the final product, ε-PLMA.

Synthesis of GelMA: GelMA synthesis was conducted according to the procedures outlined in the referenced article [149]. In summary, porcine skin gelatin (type A) was dissolved at a concentration of 10% (w/v) with PBS and stirred at 50 °C until completely dissolved. After that, 8 mL (v/v) of methacrylic anhydride was gradually dropped to gelatin solution, and the reaction took place at 50 °C for 3 hours. The resulting solution was subsequently diluted and dialyzed against

distilled water using dialysis tubing with a cutoff of 12~14 kDa, at 40 °C for one week. Finally, the gel solution was freeze-dried for 4 days, resulting in white porous foam GelMA. The synthesized GelMA was stored at -80 °C for experimental purposes. The characterization of GelMA followed the same methodology as described in the previous study.

Synthesis of G-GelMA: GelMA was dissolved as 10% (w/v) into ddH_2O at 50 °C and stirred until it was completely dissolved. Then 0.3% (w/v) photoinitiator Lithium Phenyl (2,4,6-trimethylbenzoyl) phosphinate (TCI, Inc.) was added into the solution for inducing photo-crosslinking. Oil phase was preparing by stirring 300 ml dimethyl-silicone oil (Aladdin, Inc.) and 3.6 ml emulsifier (Span 80 : Tween 20 = 3 : 1, v/v) at 50 °C for 20 minutes. Then, the GelMA solution was dripped into the oil phase by syringes within 5 minutes. The water-in-oil mixture was stirred for 8 hours and poured into a dish for UV-crosslinking 13 minutes to transform into chemical cross-linked GelMA beads (B-GelMA). The mixture was then poured into ice acetone for separating G-GelMA and oil. G-GelMA are then dried in sand core funnel through vacuum filtration. The dried G-GelMA were washed by distilled water for five times and mixed into slurry. The slurry was eventually lyophilized for 4 days to generate G-GelMA in white porous foam. The made G-GelMA was kept at room temperature for further experimental use.

3.2.2 Characterization of Biomaterials

Water Contact Angle: The prepared hydrogel series inks were tested with a contact angle measuring instrument to analyze the surface hydrophilicity of the cell scaffolds. Prepare the sample into a film with a thickness of 1 mm, and it is completely crosslinked with an ultraviolet flashlight to obtain a hydrogel film, for testing. Test procedure: Under ambient temperature, water is used as

the detection liquid, and the hydrogel film is tested by the protractor method. Each group of hydrogel membranes was tested 3 times at different locations, and the results obtained were averaged.

Water Absorption (WA) test: Using the weighing method, the quality of the prepared hydrogel series materials was weighed by a precision analytical balance, and the water absorption and swelling properties of the cell scaffolds were analyzed. First cut the series hydrogel into a size of 8 × 8 × 8 mm (length × width × height), and place it in a 10 mL centrifuge tube; then, add 5 mL of PBS solution to make the solution completely cover the hydrogel block; finally, place the centrifuge tube on a shaker with 37 °C (60 r/min, and soak for 48 hours). Water absorption ratio data analysis: Weigh the initial stent with a precision analytical balance (ME204, China) to obtain the initial weight W_0 of the stent; On 1 h, 2 h, 3 h, 4 h, 8 h, 12 h, 24 h, 36 h, and 48 h, the bulk was taken out and the moisture on the surface of it was carefully wiped dry with filter paper, and then the weight W_n was obtained by weighing the hydrogel block. For each sample, 4 parallel samples are taken as a group, and the data obtained are averaged; and the sample's water absorption rate (WA) was analysed by the **Equation 1**:

$$WA = \frac{W_n - W_0}{W_0}, (1)$$

, where n = 1, 2, 3, 4, ……, n, reflecting the time point of test.

Degradation Test: The quality of the prepared hydrogel series rubber blocks was weighed by a precision analytical balance by weighing method, and the degradation performance of biomaterials was analyzed. First, make hydrogel into a size of 8 × 8 × 8 mm (length × width ×

height), freeze-dry and place in a 10 mL centrifuge tube; then, add 5 mL of PBS solution to make the solution completely cover the scaffold; Finally, place the centrifuge tube on a shaker with 37 °C (60 r/min, and soak for 7 days). Mass Remaining Ratio (MR) data analysis: Weigh the freeze-dried initial scaffold with a precision analytical balance (ME204, China) to obtain the initial weight M_0 of the scaffold; and during soaking, according to the predetermined time point, the 1 d, 2 d, 4 d, and 7 d after soaking, the scaffolds were taken out and freeze-dried, and then these scaffolds were weighed to obtain the weight M_n. For each sample, 4 parallel samples are taken as a group, and the obtained data results are averaged; and the sample's mass residual ratio (MR) was calculated according to the **Equation 2**:

$$MR = \frac{M_n}{M_0}, (2)$$

, where n = 1, 2, 3, 4, ……, n, reflecting the time point of test.

Kelvin Probe Force Microscopy (KPFM): By using the Kelvin probe on the atomic force microscope, and the surface potential and roughness of the hydrogel series scaffolds were analysed. The hydrogel series bioinks are spread into a film with a thickness of 1 mm, and it is fully photo-crosslinked with a UV flashlight; Then, the hydrogel films were freeze-dried, and a film with a size of 8 × 8 × 1 mm (length × width × height) was cut with a knife, and it was pasted on the sample stage with conductive adhesive for testing. The surface roughness of the material is tested first. Through the test, it is found that the surface roughness of different groups of materials is similar, and the subsequent surface potential test can be selected here, so that the influence of the difference in surface roughness on the surface potential result can be ruled out. For example, the test area selected in this paper is the material area with the surface roughness ranging from -80 to +80 nm.

Mechanical Compression Test: A mechanical testing machine was used to carry out mechanical compression tests on the prepared a series of ahydrogel materials to analyze the mechanical properties of the cell-laden hydrogel scaffolds. The hydrogel series bioinks were poured into an 8 × 8 mm (diameter × height) cylinder. Put it in a transparent cylindrical mold, and use a UV flashlight to make it fully photo-crosslinked to obtain a series of hydrogel block; then put the hydrogel block into dd H_2O, and take it out after reaching an equilibrium swelling state for testing. Test procedure for mechanical compression: Set the compression speed to 5 mm/min, and perform a compression test on the series hydrogel block until cracks appear in the hydrogel block. Each sample was taken as a group of 4 parallel samples, and the data obtained were averaged. The stress-strain curve of the material is analyzed by OriginPro software, and the compressive modulus of the sample is obtained according to the slope of the curve.

Scanning Electron Microscopy (SEM) analysis: The SEM test of the prepared hydrogel scaffold was carried out by field emission scanning electron microscope. The preparation steps of the SEM sample: The cell scaffold constructed into a large size and complex shape was first cultured to the 4th day, and after taking it out, the cell scaffold was dehydrated with ethanol gradient, and then freeze-dried. Finally, paste the dried cell scaffold on the sample stage with conductive glue, and spray gold for 30 s, ready for testing.

3.2.3 Preparation of Bone/Cartilage and Vessel Bioinks

The specific contents of different groups of inks are given a name, for example, an ink

containing 8 % AlgMA and 0 % ε-PLMA is named AlgMA8 bioink.

Preparation of AlgMA/PLMA Bioink: First, in a disposable centrifuge tube, 1% double-antibody penicillin-streptomycin (Penicillin-Streptomycin, P/S), 10% Australian fetal bovine serum (Fatal Bovine Serum, FBS), 89% α-MEM Culture media were mixed to prepare serum-containing α-MEM culture medium, hereinafter referred to as MEM culture medium. Next, dissolve the AlgMA and ε-PLMA sample into MEM culture solution containing 0.1% LAP photo-initiator.

Preparation of GelMA Bioink: First, GelMA sample was dissolved into MEM culture medium with 0.1% LAP. Next, dissolve the G-GelMA sample in the GelMA solution.

3.2.4 Printability and Rheological Properties of Bioinks

The prepared series of bioinks are tested by rotational rheometer, from viscosity-shear rate, modulus-strain, modulus-frequency, modulus-temperature, UV curing and cycling oscillation to comprehensively analyze their rheological properties. All tests are performed with a 25 mm flat plate (PP 25) and each group repeated at least three valid samples independently. All the test gap is 0.2 mm and the test temperature is 37 °C.

"Viscosity - Shear rate" Test: The shear rates were set to vary from 0.1 to 100 s^{-1} according to the logarithmic law, and a total of 46 data points are taken.

"Modulus - Strain" Test: The angular frequency (ω) is set at a constant value of 10 s^{-1}, and the shear strain varies from 0.01 to 1000 % according to the logarithmic law. A total of 41 data points is taken.

"Modulus - Frequency" Test: The shear strain is set to keep a constant value of 1%, the

frequency changes from 0.1 to 100 Hz according to the logarithmic law, and a total of 31 data points are taken.

"Modulus - Temperature" Test: The shear strain and frequency are set to keep a constant value of 1% and 1 Hz, the temperature changes from 4 to 40 °C, and a total of 41 data points are taken.

"Modulus – Photo-crosslinking Time" Test: Set the shear strain and frequency to be kept constant at 0.1% and 10 Hz, respectively. The first stage starts from the 10th second (s), the UV lamp is not turned on, the test duration is 40 s, and one point is taken every 2 s; in the second stage, the UV light is turned on for 100 s, and 128 points are taken according to the logarithmic law individual.

"Cyclic Oscillation" Test: In the first stage, the shear strain and frequency are set to keep a constant value of 1% and 1 Hz, respectively, and a total of 120 data points are taken; in the second stage, the shear strain and frequency are set to a constant value of 500% and 1 Hz, respectively, and a total of 180 data points are taken. Each cycle consists of Phase 1 and Phase 2 for total of 6 cycles, and ending with Phase 1.

Extrusion Properties: A transparent plastic printing syringe filled with series bioinks was installed on an extrusion 3D printer, driven by a pneumatic pump, and the state of the line when the ink passed through a 22-gauge (G) plastic needle was recorded.

Evaluation of Extrusion Pressure: By taking a reading on a computer connected to an extrusion 3D printer, the printing extrusion pressure required to just squeeze the different series bioinks out of the needle was recorded.

Evaluation of Photo-crosslinking Time: Pour series bioink into a transparent cylinder mold

with a size of 8 × 40 mm (diameter × height), irradiate UV light from bottom to top, and record the time used for curing the top of different cylinder samples duration.

Evaluation of Printed Filaments: A stereo microscope was used to evaluate the shape and structure of the printed hydrogel scaffold. First, use 3Ds max software to design a cube 3D bracket model, and import the model into the extrusion 3D printer. Then, the series bioink was extruded through the extrusion 3D printer to fabricate a cross-structured hydrogel scaffold, and each scaffold was printed with 3 layers. Finally, crosslink and soak the scaffolds in PBS solution for testing.

Preparation and Printing of Bioink: To create cell-laden bioink, a suspension of hBMSCs or RSCs was thoroughly mixed and incorporated. Each of the resulting bioink was loaded into a transparent plastic syringe, and a designed 3D scaffold model in the form of a cube was imported into an extrusion 3D bioprinter. Using a pneumatic pump, each of the ink was extruded through a 40# (400 μm) tapered nozzle into a Petri dish. The scaffold lines of each layer were printed with a 90° rotation to the adjacent layers, depositing the lines one layer at a time to construct a cellular scaffold. Subsequently, a UV light was employed to irradiate the printed cell-laden scaffolds, inducing UV-crosslinking and forming stable constructs. This process yielded a series of cell-laden scaffolds. Finally, each of the scaffold was put into a 12-well plate, and a suitable volume of medium was used to ensure the scaffold was adequately covered. The plate was then transferred to an incubator and maintained for seven days at 37 °C with a CO_2 concentration of 5%. The culture solution was refreshed per 2 days during this period.

Evaluation of Printability of Bionks: The structure and shape of those four bioprinted scaffolds were characterized *via* a high-definition camera.

1) Mesh size (MS) Analysis: The printed scaffolds were captured and documented using a

camera at three time points: 0 seconds (immediately after printing), 10 seconds, and 5 minutes, prior to their crosslinking. To calculate the Mesh Spacing (MS), the software ImageJ was utilized, in which the size of thirty-six meshes in the central region of each scaffold was labelled and measured.

2) Printability (Pr.) Analysis: Under ideal gelation conditions, the extruded filament of the bioink exhibits a distinct morphology characterized by a smooth surface and consistent width. As a result, the fabricated constructs feature regular square meshes [150]. However, when the bioink experiences insufficient gelation, the printed filaments assume a more fluid-like status. Consequently, the higher layer tends to merge or fuse with the lower layer, leading to the creation of approximately circular meshes within the constructs [150].

Circularity (C) of a mesh pole was defined through **Equation 3**:

$$C = \frac{4\pi A}{L^2}, (3)$$

And referring to Ouyang *et al.*, Pr. was evaluated through **Equation 4**:

$$Pr = \frac{\pi}{4} \times \frac{1}{C}, (4)$$

where, L represents perimeter and A represents area. It is well-known that circles own a highest circularity (C) as 1. When the C value is near to 1, the shape of the mesh is closer to a circle.

3) Shape Maintenance (SM) Analysis: To determine Strain Maintenance (SM) at ten seconds and five minutes, the Mesh Size (MS) at these time points was divided by MS at zero seconds. The calculation for the SM at 10 seconds involved dividing the MS at 10 seconds by the MS at 0 seconds. Similarly, the SM at 5 minutes was calculated by dividing the MS at five minutes *via* MS at zero seconds. The sample's SM was computed using **Equation 5**, where 'n' represents the time elapsed post-printing:

$$SM_n = \frac{MS_n}{MS_0}, (5)$$

, where n = 10 s, 5 min, meaning the interval time point of this test.

4) Printing Stability (PS) Analysis: The PS was determined by analysing a minimum of three scaffolds, each containing 36 meshes. In an ideal scenario with excellent printing stability, the mesh size within a single scaffold would be steady. However, if the bioink exhibited poor PS, there could be a significant variation in mesh sizes within a single scaffold. To evaluate the PS, both the Average Mesh Size (A_{MS}) and the Standard Deviation of the Average Mesh Size (S_{MS}) need to be measured. A_{MS} will be calculated through **Equation 6**:

$$A_{MS} = \frac{\sum_{i=1}^{n} MS_i}{n}, (6)$$

And S_{MS} can be calculated as **Equation 7**:

$$S_{MS} = \sqrt{\frac{\sum_{i=1}^{n}(MS_i - A_{MS})^2}{n-1}}, (7)$$

, where n = 1, 2, 3, 4, ……, n, reflecting the number of meshes.

And PS was calculated through the division of A_{MS} to S_{MS}, which could be defined as **Equation 8**:

$$PS = \frac{S_{MS}}{A_{MS}}, (8)$$

Evaluation of Crosslinking Stability of Alg-based Inks: Similar to section 4.7.2, the printed scaffolds underwent immediate crosslinking. They were placed in 6-well plates on a shaker at 37 °C (60 r/min) and soaked for 28 days. A high-resolution camera was utilized to assess the structure and shape of these four types of scaffolds at various time points: 0 days (immediately after crosslinking), 1 day, 7 days, 14 days, and 28 days. To evaluate the crosslinking stability (CS), the size of the scaffolds (SS) was measured. The CS at 7 days was determined by dividing the SS at 7

days by the initial scaffold size (SS_0). The changing of scaffold size (CSS) can be calculated as **Equation 9**:

$$CSS_n = \frac{SS_n}{SS_0}, (9)$$

And CS can be defined through **Equation 10**:

$$CS_n = \ln CSS_n, (10)$$

, where n = 1, 7, 14, 28, reflecting the interval time point of this test.

The highest CS is zero. Shrink or swell of scaffolds reflects on an either negative or positive value.

3.2.5 Biocompatibility of Bioinks

To create a cell-laden bioink, a suspension of hBMSCs at a density of 1×10^6/mL was added and thoroughly mixed. The resulting bioink was then loaded to a plastic syringe. Next, a designed cube 3D model was input to an extrusion 3D bioprinter. With the assistance of a pneumatic pump, the bioink was extruded through a 22 G plastic needle into a Petri dish. The scaffold lines of each layer were printed with a 90° rotation to the adjacent layers, gradually depositing the lines layer by layer and forming a cellular bio-scaffold. Subsequently, a UV torch was used to irradiate the fabricated bio-scaffold, inducing UV-crosslinking and enabling the formation of a stable structure. This process results in the creation of the cell scaffold. Finally, the scaffold was put in a 12-well plate, and a suitable volume of medium was introduced to ensure the scaffold was adequately covered. The plate was then transferred to a cell culture incubator and maintained for seven days at 37 °C with a CO_2 concentration of 5%. During this period, the MEM culture solution was refreshed every 2 days.

Live/Dead Test: After the completion of printing, the 12-well plate containing the cultivated bio-scaffold was taken out. The medium in each 12-well plate was refreshed, and scaffolds were immersed with PBS for three times, and each time is 5 mins. Subsequently, at ambient temperature, 2 mL of the prepared PI-FDA dual pigments were introduced to each well plate, ensuring the dye fully covered the scaffold, and the staining was conducted in darkness for 20 minutes. Following the staining process, scaffolds were moved out and rinsed with PBS to eliminate any extra pigment. Finally, the set of bio-scaffolds were positioned on glass slides and detected under the fluorescent upright microscope, and photographed for documentation purposes.

In order to investigate the impact of extrusion pressure on cell viability during printing, the following steps were carried out: Bioink was printed using extrusion pressures of 60, 80, and 100 kPa to produce cell scaffolds. After a period of 4 hours from the completion of printing, the bio-scaffolds were subjected to cyto-live/dead staining to assess their cellular viability.

CCK-8 Test: The cell proliferation/toxicity kit was used to detect CCK-8 on the prepared series of cell scaffolds, and the cell proliferation ability of the cell scaffolds was analysed by a full-wavelength microplate reader. Before each CCK-8 test experiment, drip 1 mL of CCK-8 stock solution to 10 mL of α-MEM medium to prepare CCK-8 working solution, store it in the dark, and prepare it for immediate use.

At 4 h, 1 d, 4 d, and 7 d after cell printing, take out the cell culture well plate for culturing series of cell scaffolds, discard the MEM culture medium in 12-well plate, and replace it with PBS solution. Dip the scaffolds 3 times, and each time is 5 mins. Then, drip 2 mL of prepared CCK-8 working solution to each well of the plate, so that the dye has covered the sample; each sample is used as a group of 3 parallel samples, and a set of blanks with cell-free scaffolds sample. Then,

place the well plate with the scaffolds into the incubator and maintain 37 °C and 5% CO_2 environment for two hours in the dark. After the incubation, each sample was pipetted into a 96-well plate with 100 μL of liquid per well. Finally, put the 96-well plate containing the solution into a full-wavelength microplate reader for testing at a wavelength of 450 nm. Absorbance value (Optical Density, OD) data analysis: Set 5 holes for each parallel sample, and take the average value of the obtained data results; read the absorbance E_n of the sample and the absorbance E_0 of the blank group, and calculate the internal density of the sample according to the **Equation 11**:

$$OD\ value = E_n - E_0\ , (11)$$

OD value is the optical density value of cells, where n = 1, 2, 3, ……, n, meaning the interval time point of this test.

DAPI/F-actin Staining: Immunofluorescence staining was used to observe the fibrous actin and nuclei of the cells inside the prepared series of cell scaffolds, and the morphology of the cells inside the cell scaffolds was observed by laser confocal microscopy.

After bioprinting of 4 days, the 12-well plate was taken out, and the MEM medium was removed; and bio-scaffolds were soaked in PBS for 3 times, and each time is 5 mins. After that, add 2 mL of immunostaining fixative to each well, fix the condition at 4 °C for 30 min, and then discard; and wash the scaffold with PBS solution. Subsequently, 0.25% Trition X-100 solution was added to submerge scaffolds to permeabilize the cell membrane, treated at room temperature for 10 min, then suck the solution out and wash them with PBS solution. Next, block the scaffolds with 5% goat serum at room temperature for 2 h and then discard; add the primary antibody-Anti-Collagen II antibody working solution to soak the scaffolds, and suck the solution away after overnight at 4°C; and wash the scaffolds with PBS solution at ambient temperature. Afterwards,

the secondary antibody—goat anti-rabbit IgG H&L working solution was added to immerse the scaffolds, and they were treated at room temperature in the dark for 2 hours, and then suck the solution out; then, scaffolds were washed with PBS solution. Next, add the phalloidin dye working solution to soak the stents, treat them at ambient temperature in the darkness for 30 min, and then suck the solution out; then wash the stents with PBS solution. Then, add DAPI solution to soak the stent, treat it at ambient temperature in the darkness for 10 min, and then suck the working solution out; then wash the stents with PBS solution. Finally, the stained cell scaffolds were placed in a confocal special culture dish, observed and recorded *via* a confocal laser microscope. The excitation wavelengths are 488 nm and 594 nm.

3.2.6 Design of the G-code and Printing Process

According to the previous description, we first constructed the 3D model in rhino and wrote the G-code for controlling the movement of the printer, *e.g.*, nozzle movement and pressure channel on/off.

To build up this joint on a chip, we chose four channels to fabricate the chip, as shown in **Figure 5A**:

a) Channel 1: Bioink (AlgMA/PLMA) with hBMSCs.

b) Channel 2: Bioink (AlgMA/PLMA) with hBMSCs.

c) Channel 3: Supporting ink with GelMA and Nano-clay (thickening agent).

d) Channel 4: Co-axial printing with core channel (supporting ink: sacrificial material) and shell channel (bioink: G-GelMA).

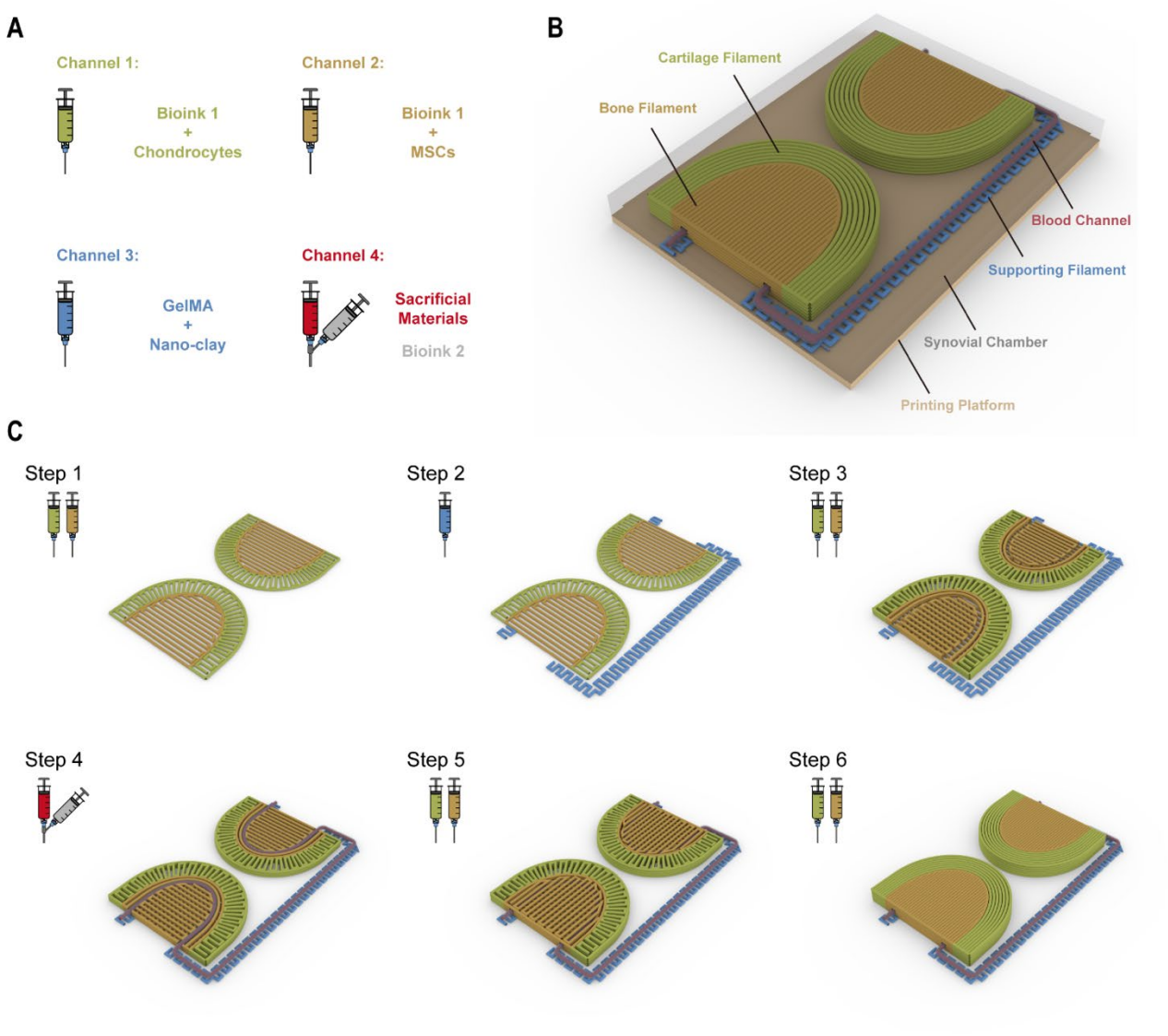

Figure 5. The Manufacture of the Joint-on-a-Chip. A) Different bio-inks from different printing channels used in this joint-on-a-chip. **B)** The rendered structure of printed structure. **C)** The logic order of steps used in the chip manufacture.

The chip has six-layer filaments and a core-shell perfusable channel. It will be printed on a piece of glass (printing platform), and then be put into a mode and sealed for perfusable culture (**Figure 5B**).

In addition, in order to realize the cell distribution in cartilage zone. We specially designed

the filling topology in the cartilage zone. As shown in **Figure 5C**, this six-layer structure will be fabricated in 6 steps.

a) Step 1: Bone and cartilage manufacture. The bone structure was printed with parallel filament and the cartilage structure was printed in two directions. The outside and inside curvy filaments are parallel, while the middle part is radial pattern. In this way, the Chondrocytes were distributed like the cells in **Figure 1B**.

b) Step 2: Supporting structure manufacture. In order to fabricate the blood vessel in second layer, a supporting layer (blue part) should be printed in the first layer.

c) Step 3: Bone and cartilage manufacture. The second bone pattern is similar to the first layer with a 90° rotation and the third layer is same as the first layer. The second and third cartilage pattern is same as the first layer.

d) Step 4: Blood vessel manufacture. This tubular structure was printed by a coaxial nozzle which had a sacrificial core and a hydrogel wall. This filament was printed through the bone filaments and on the supporting filaments.

e) Step 5: Bone and cartilage manufacture. The bone pattern is similar to the first layer with a 90° rotation. The cartilage pattern is same as the first layer.

f) Step 6: Bone and cartilage cap manufacture. The bone and cartilage pattern are parallel tightly stacked to seal the bone part avoiding the fluid directly leaking into the cartilage and synovial part.

3.2.7 Statistical Analysis

All data were visualized through software - Origin Pro, and the data were expressed as mean

± SD; CCK-8 data and some data were analysed *via* one-way analysis of variance using Tukey's post hoc test, and P values for significant differences were *P < 0.05, **P < 0.01, ***P < 0.001, where *P represents significant difference in data, **P and ***P represent extremely significant difference.

3.3 Results and Discussion

3.3.1 Bone/Cartilage Bioink – AlgMA/PLMA

By comparing the findings with previously published studies [151, 152], successful synthesis of AlgMA (**Figure S1**) and ε-PLMA (**Figure S2**) was achieved. **Figure S1A** and **S2A** demonstrated the light-crosslinking characters of AlgMA and ε-PLMA, respectively. As illustrated in **Figure S1B-E** and **Figure S2B-D**, the methylacrylation of alginate and ε-Polylysine was measured as degree of substitutions (DS) of 28.2 ± 0.6% and 30.7 ± 1.4% (calculated by **Equation S1** and **S2**), respectively. The number average molecular weight (Mn) of AlgMA and ε-PLMA is 273 kDa and 0.8 kDa, respectively (**Equation S3**, **Figure S1F**, and **S2E**). According to previous report from Tabriz *et al*., used 8% (w/v) Alg bioink to bioprint large-scale constructs [153]. To confirm a appropriate printing window for the mixed AlgMA/PLMA bioink [154], a set of ratio on solid contents of these two materials were evaluated (**Figure S3**). The results suggested that a minimum of 8% (w/v) AlgMA is necessary for extrusion and AlgMA/ε-PLMA ratio should below 1:2 (**Figure S3**). Consequently, in further observation, sets of polyelectrolytes AlgMA/PLMA bioinks through fixing AlgMA concentration to 8% (w/v) while improving ε-PLMA concentration from 0% (w/v) to 16% (w/v) were carried out. After that, the mixture of these two kinds of hydrogels were tested to confirm their stability which ensures no basic characters change within

them during the mixture of the bioink. According to the analysis of thermogravimetric (TGA) and X-ray diffraction (XRD), no crystal structure changing was found after the modification (**Figure S4A-D**), also confirming their steady chemical/physical characters during synthesis procedure. Moreover, these results from FTIR spectra analysis (**Figure S4E**), TGA analysis (**Figure S4F**), and XRD analysis (**Figure S4G**) proved that the blending behavior did not cause changes on crystal structure.

In **Figure 6**, we present a comparison between our proposed AlgMA/PLMA bioink, and other three traditional Alg-based bioinks to highlight its advantages. The three bioinks selected for comparison are as follows: Alg/Ca^{2+}, which consists of pure alginate crosslinked *via* Ca^{2+} (single molecule) after printing; AlgMA/Ca^{2+}, which involves AlgMA post-crosslinked *via* UV and Ca^{2+}; and AlgMA/GelMA, which is a mixture of AlgMA and larger molecular pre-crosslinker GelMA *via* electrostatic interaction before printing and further post-crosslinked *via* light stimuli. In previous reports, the operability of blend bioinks during the preparation process has often been overlooked, despite its importance. Therefore, achieving a stable printing state by using an even blend bioink was prioritized. To contrast the capacity of homogenization and preparation efficiency of the bioink, a blending-time test was initially conducted. In the case of AlgMA/GelMA bioink, the entanglement of long chains of AlgMA and GelMA resulted in a longer homogenization time compared to other three Alg-based inks. In order to further confirm this observation, semi-quantitative experiments were performed. GelMA-Rho (with red fluorescent) and ε-PLMA-FITC (with green fluorescent) were separately mixed with AlgMA to investigate the micro-interactions between these biomaterials. After stirring for 10 seconds, the small-molecule ε-PLMA could be uniformly mixed with AlgMA, as depicted in **Figure 6A** and **Figure S5**. However, achieving a

relatively uniform state required at least 10 minutes of stirring when mixing AlgMA with the large-molecule GelMA (**Figure 6A**). The AlgMA/PLMA series bioinks' uniformity was further evaluated by investigating the emerging Nitrogen (N) element blended with ε-PLMA referring to EDS analysis (details in **Table S1**). The element N of blend bioinks had an even distribution and presented a clear growth by increasing the ε-PLMA (**Figure S6**). The shorter stirring time, the less harmful to cells, therefore, the mixing time is important for bioinks. Small-molecular pre-crosslinkers have significant advantages over large-molecular one, due to the composites' homogenized dynamics.

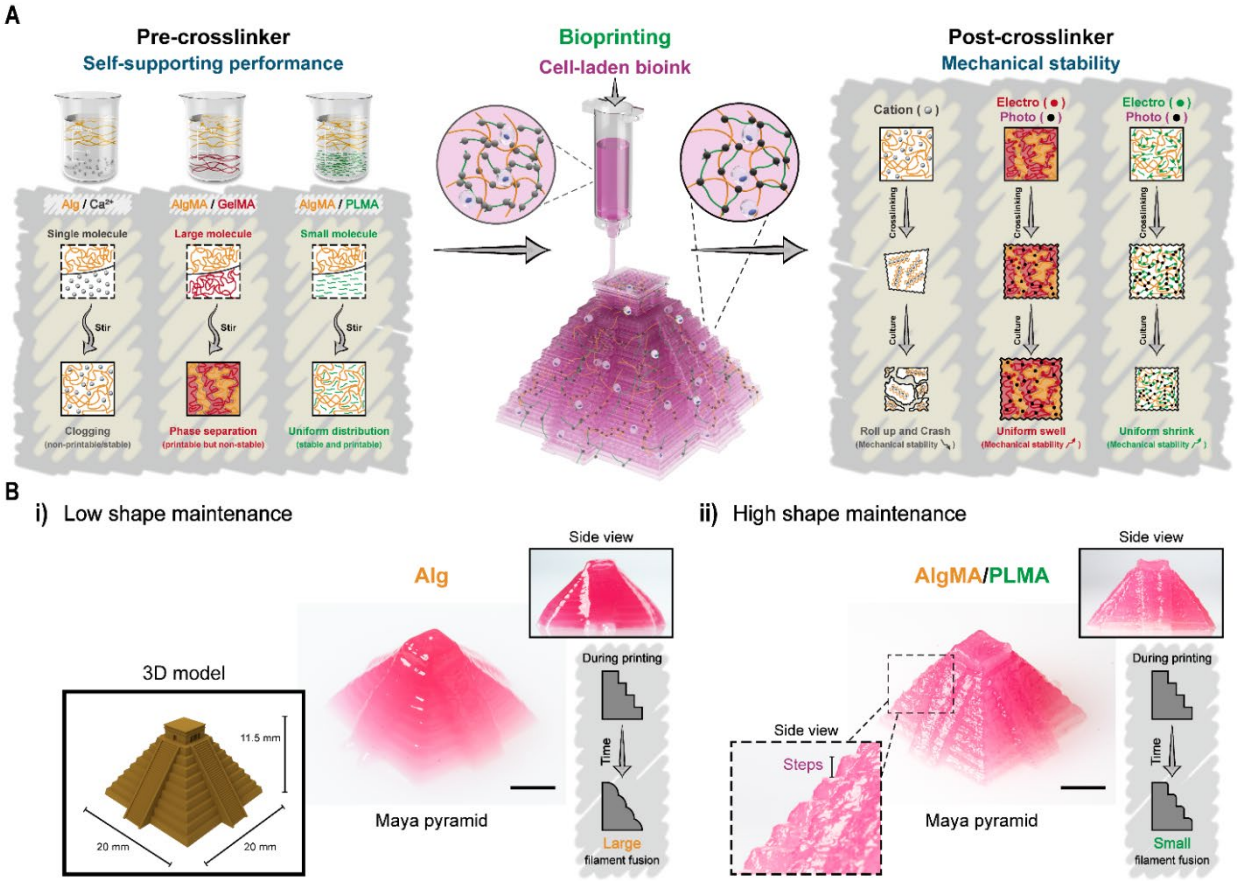

Figure 6. The Schematic Illustration of PLMA Used as Crosslinker of Bioink. **A)** The bioink design consists of AlgMA and ε-PLMA. **B)** The AlgMA/PLMA bioink exhibits self-supporting characteristics and maintains its shape, enabling the successful creation

of intricate scaffolds, such as the Maya pyramid shown in the image. The dimensions of the pyramid are 17 × 17 × 11 mm (length × width × height). Scale bar in **B**, 5 mm.

Moreover, we devised a nested "Ring-Hive" structure characterized by neatly arranged hexagons surrounded by a ring, in order to assess the crosslinking stability and printability. The structures printed using AlgMA/GelMA bioinks and AlgMA/PLMA bioinks exhibited precise hexagonal outlines. Furthermore, even after crosslinking (**Figure 6B**), the distances between the ring and hexagons remained visible. In contrast, the structure printed using ionic crosslinking displayed an indistinct shape, indicating the crucial role of pre-crosslinking in maintaining the fidelity of the Alg-based bioink. To evaluate the stability of four types of bio-scaffolds, an extended observation of the shape was conducted while the scaffolds were immersed in PBS. As depicted in **Figure 6C**, the scaffolds printed through ionic crosslinking exhibited significant deformation, whereas those subjected to photo post-crosslinking and electrostatic pre-crosslinking did not. The physical structure of a single-crosslinked network using Ca^{2+} ions experienced crushing within just one day of culture, leading to shrinkage in the AlgMA/Ca^{2+} scaffold due to Ca^{2+} loss. On the other hand, the two photo-crosslinked scaffolds exhibited minimal structural changes over a period of 28 days (**Figure 6C**). Therefore, for Alg-based scaffolds to meet long-term requirements, a stable post-crosslinking process is crucial, particularly in tissue engineering applications. As illustrated in **Figure 6B**, the utilization of ε-PLMA improved the printing accuracy of the Alg-based ink. However, it remains unclear to what extent this enhancement can be achieved. To investigate this, we designed and printed a four-layer “Criss-Cross” cubic scaffold composed of filaments rotated at 90° in each layer. **Figure 3A** illustrates that the pre-crosslinked grid-like scaffolds created using Alg/Ca^{2+} and AlgMA/Ca^{2+} bioinks experienced significant structural collapse over time. It worth

to note that the printed Alg/Ca^{2+} and AlgMA/Ca^{2+} filaments fused together no more than 10 seconds and 5 minutes just after printing, respectively. Conversely, the AlgMA/GelMA and AlgMA/PLMA filaments were able to maintain their shape for more than 5 minutes. This result demonstrates that pre-crosslinkers hold greater potential for large-scale Alg-based bio-manufacturing endeavors.

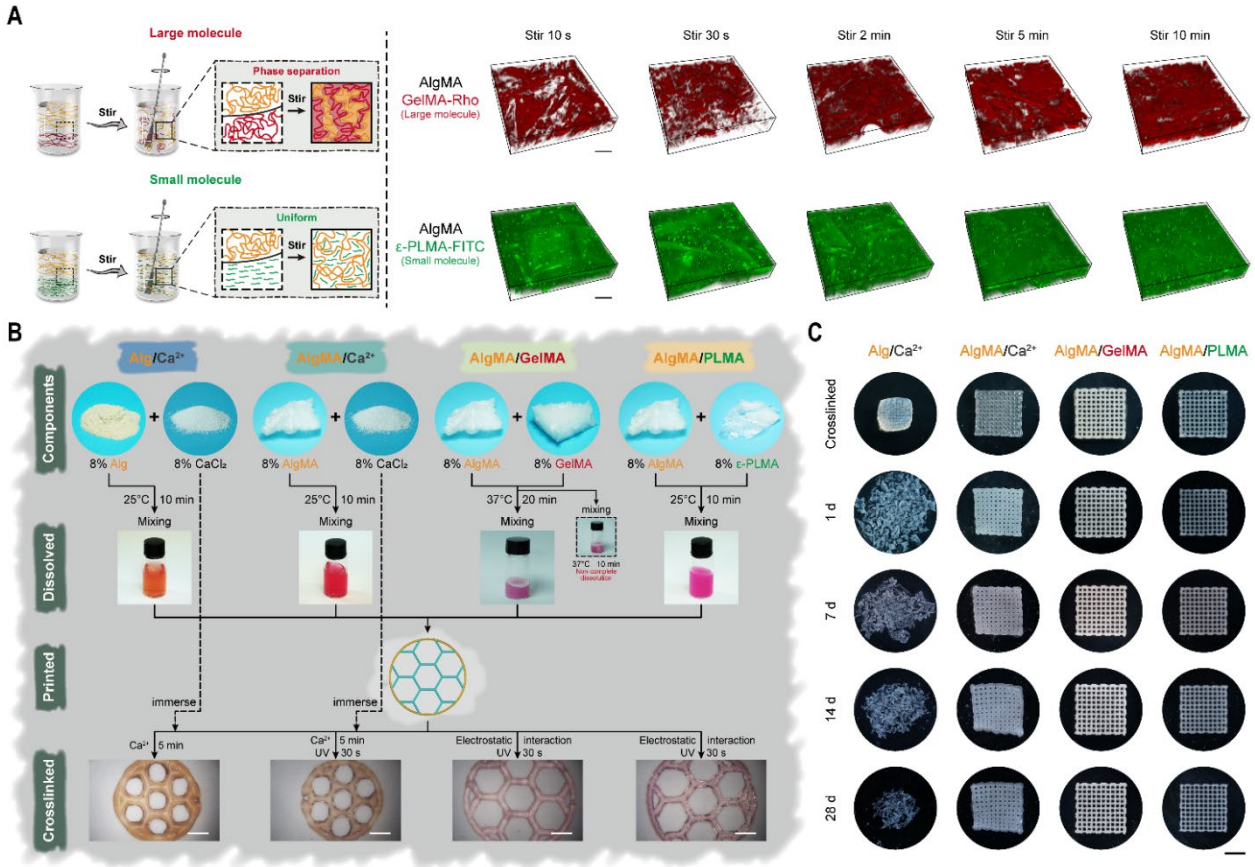

Figure 7. The Preparation and Crosslinking Stability of Alg-based Bioinks. A) Pre-gelation AlgMA gels with different molecule weight pre-crosslinkers exhibit significant behaviors during the blending process. Scale bar in A, 50 μm. **B)** The four types of Alg-based bioinks are prepared and displayed in a 2D plot. Scale bar in B, 2.5 mm. **C)** Macroscopic appearance of 3D-plotted bio-scaffolds at crosslinked (day 0), day 1, day 7, day 14 and day 28 of immersion in PBS (37 °C, 60 rpm) for Alg/Ca2+, AlgMA/Ca2+, AlgMA/GelMA bio-scaffolds and AlgMA/PLMA bio-scaffolds. Scale bar in **C**, 5 mm.

In a previous study [146, 148] (**Figure S7A**), the fidelity of 3D printing was defined as the

degree of resemblance, also called the outline resolution which is the length * width * height of the construct, between the designed model and the actual printed object. To assess the manufactured structure outline, a metric called Printability (Pr.) was employed to evaluate the behavior of printing [150]. However, when it comes to the detailed characterization of feature resolution (**Figure S7B**), such as the pyramid steps (**Figure 6B**), lots of analysing approaches were qualitative in nature. To realize a more specialized characterization of the printability of Alg-based hydrogels, several quantitative indices were introduced, containing Shape Maintenance (SM), Printing Stability (PS), and Crosslinking Stability (CS). Among these, SM and PS were measured during the pre-crosslinking phase. Specifically, SM measured the shrinkage of the fabricated mesh size during printing time, while PS assessed the uniformity of the mesh size. In comparison, CS was analysed during the post-crosslinking phase and measured the deformation of the printed mesh with time.

First, calculated by **Equation 3** and **4**, Pr. was carried out to illustrate the printing performance of different bioinks. In a former record [150], the bioprinted structure will have excellent filament shape when Pr. is between 0.9 and 1.1. As shown in **Figure 8A**, different mesh shapes have been found on these four printed grids. The Pr./mesh shapes of Alg/Ca^{2+} and AlgMA/Ca^{2+} were 0.79/circle and 0.83/rectangle with chamfers (**Figure 8B**), respectively. While the Pr./mesh shapes of AlgMA/GelMA scaffolds and AlgMA/PLMA scaffolds were 1.09/irregular polygon and 0.93/clear rectangle (**Figure S8A** and **Figure 8B**), respectively. Although AlgMA/GelMA and AlgMA/PLMA bioinks achieved excellent Pr., AlgMA/PLMA filaments represented a smoother surface comparing with AlgMA/GelMA filaments (**Figure S8A**).

In order to achieve the manufacturing of large-scale structures, it is essential for the filaments to maintain their shape throughout the entire manufacturing process. Otherwise,

displacement occurs, leading to a mismatch between the printed filaments. To further characterize this property, a new characterization parameter called Shape Maintenance (SM) was introduced, calculated using **Equation 5**. By analysing and quantifying the mesh size of these four kinds of scaffolds, it was found that AlgMA/GelMA and AlgMA/PLMA bio-scaffolds exhibited superior performance in terms of SM (**Figures 8C** and **8D**). After 10 seconds of printing, both polyelectrolyte bioinks achieved a nearly 97% SM, while it was 37% or 74% for the Alg or AlgMA electrolyte, respectively (**Figure 8D**). As the printing time extended to 5 minutes, the SM values for these four bioinks were 33.5%, 6.1%, 96.3%, and 84.4%, respectively. It is worth noting that the slight change in Alg/Ca^{2+} between 10 seconds and 5 minutes was due to the immediate fusion of filaments during printing. Due to the physical crosslinking of GelMA at room temperature, the AlgMA/GelMA bioink exhibited a slight advantage over the AlgMA/PLMA bioink.

Ensuring the triumphant manufacture of a large-scale construct goes beyond just the SM of the bioinks; the uniformity of each filament is also crucial. This implies that the mesh size should have similar values across the construct. Another parameter, Printing Stability (PS), was employed to analyse the variation in the scaffold mesh, which shows the permanence of the printed scaffolds. The uniformity evaluation of the printed scaffold mesh size involved rating the ratio of the average mesh size (A_{MS}) to the standard deviation of the mesh size (S_{MS}), as described in **Equations 6**, **7**, and **8**. As depicted in **Figure 8E**, the PS values for these four bioinks were 1.45, 9.28, 11.37, and 20.29, respectively. This indicates that the AlgMA/PLMA bioink exhibited the best PS comparing with other alginate-based bioinks.

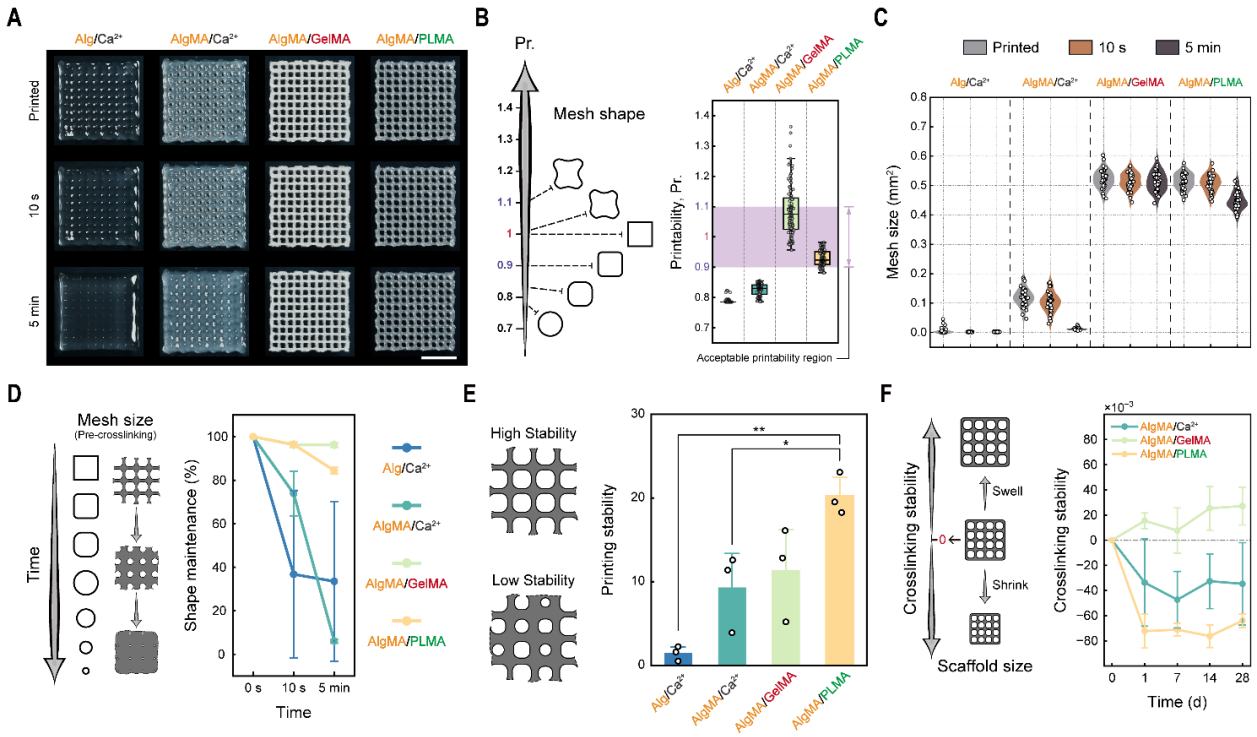

Figure 8. The Printing Performance of Alg-based Bioinks. A) The evolution of filament shape over time following the manufacturing of alginate-based scaffolds. Scale bar in **A**, 5 mm. **B)** Printability (Pr.) of four Alg-based scaffolds. **C)** Mesh size measurements of four Alg-based scaffolds immediately after printing, 10 seconds after printing, and 5 minutes after printing. **D)** Assessment of SM for four types of alginate-based bioinks. **E)** Evaluation of PS for four types of alginate-based bioinks. **F)** Examination of CS in AlgMA/GelMA and AlgMA/PLMA bio-scaffolds.

After the manufacture of a large-scale structure, two important questions arise: How accurately can the object maintain its shape, and for how long? To address this, a new parameter called Crosslinking Stability (CS) was introduced to assess the object's ability to maintain its shape after crosslinking. We conducted a long-term observation of the shape of the PBS-immersed scaffolds to evaluate the performance of these post-crosslinkers. By using **Equations 9** and **13**, we analysed the CS values of the ion post-crosslinker (Ca^{2+}) and the covalent post-crosslinker (MA) respectively. As depicted in **Figure 8F**, **S8B**, and **S8C**, the AlgMA/Ca^{2+} bioinks and AlgMA/PLMA bioinks exhibited an insignificant size shrinking, reflected by CS values ranging from 0 to -0.034 and -0.072, respectively, on the first day after printing. On the other hand, the AlgMA/GelMA

scaffolds experienced a slight increase in size which has a CS value between 0 and 0.015. Subsequently, all other three bioinks demonstrated a steady scaffold size during long-term immersion.

Taken together, the findings suggest that the small-molecular blend AlgMA bioink, utilizing a pre-crosslinker PLMA, exhibits the most favorable printing performance compared to the other three bioinks. Additionally, we observed that the AlgMA/PLMA scaffold demonstrated an isometric size shrinkage while maintaining its original shape, making it suitable for high-precision 3D bioprinting [155]. In fact, we have successfully utilized AlgMA/PLMA to print intricate structures with exceptional accuracy, including large-sized bone/cartilage tissues with specific shapes on a chip.

For direct printing of large-scale structure with a high-fidelity contour, in addition to the basic requirement that the material has a certain shear-thinning and self-healing performance, the bioink also needs to have a strong self-supporting performance to prevent structural dislocation during printing.

Because of its excellent printability and potential use in tissue engineering, we conducted further analysis on the physicochemical characters of various AlgMA/PLMA bioinks based on small molecular pre-crosslinkers. As previously stated, we created a range of AlgMA/PLMA bioinks by maintaining an 8% (w/v) AlgMA concentration and gradually increasing the ε-PLMA concentration from 0% to 16% (w/v) for research purposes.

The property of charge plays a crucial role in biomaterials as different types of cells exhibit distinct preferences for surface potential. Upon analysing this property, we made an unexpected discovery that the AlgMA/PLMA materials' surface potential increased as the ε-PLMA content

increased, while maintaining a similar surface roughness (refer to **Figures 9A** and **9B**). Specifically, the surface potential rose from -345.25 mV to 121.55 mV when the content of ε-PLMA escalated from 0% to 16%. It is clear that the introduction of the positively charged, small compound ε-PLMA can alter the electrical microenvironment within alginate-based materials. Hydrophilicity is another characteristic that greatly affects cellular behavior. As depicted in **Figure 9C**, the water contact angles (WCA) of the surface on materials rise from 26.64° to 52.00° when comparing AlgMA8 with AlgMA8-PLMA16. These measurements still indicate that the materials are hydrophilic, which is conducive to cell proliferation, as referenced in study [156]. Nonetheless, an excessively hydrophilic nature may lead to the distortion of the hydrogel's structure due to the absorption of large volume of water. In tissue engineering, scaffolds are often required to be cultured for extended periods, making stability in an aqueous environment a critical attribute. To assess the endurance of the AlgMA/PLMA materials, we conducted tests on water absorption (WA) and degradation, as shown in **Figures 9D** and **9E**. **Figure 9D** reveals that the AlgMA8 hydrogel experienced significant swelling upon immersion in PBS for 1 hour, and it did not reach a state of swelling equilibrium until after 36 hours, culminating in a WA rate of 13.06% in the end. This swelling is attributed to the -COOH groups' ionization within the molecular chain of AlgMA, which encourages water to permeate the network of polymer, causing the AlgMA to expand. In contrast, hydrogels that included ε-PLMA achieved swelling equilibrium in just 2 hours. Moreover, as the content of the cationic crosslinker ε-PLMA was increased, the balance water swelling rate of the AlgMA/PLMA hydrogel correspondingly went down. Notably, after 3 hours of incubation, there was a reduction in all AlgMA/PLMA material weight.

Beyond the neutralization of hydrophilic groups, the composite material features an

increased number of crosslinking sites and a more compact network, which limits the ingress of water and reduces swelling. This could further explain the observed decrease in hydrophilicity. As presented in **Figure S9**, SEM results corroborate this theory, showing that the porous construct of the material begins to contract following the addition of cationic crosslinker ε-PLMA. When the positive/negative charging ratio rises, the crosslinking density within AlgMA/PLMA series hydrogels also increases, leading to a tighter network and smaller pores. Specifically, for AlgMA8-PLMA16, the pore size collected from its cross-sectional view reduced to less than 20 μm, which could hinder proliferation cell and nutrient exchange. Nevertheless, ε-PLMA's role extends beyond merely crosslinking with AlgMA; it undergoes self-crosslink, too. Scaffolds with a progressive positive/negative charging ratio contain more pre-crosslinker, resulting in self-crosslinked ε-PLMA nanoparticles accumulating on the scaffold's surface, as depicted in **Figure S9A**. These particles are then agitated by PBS, causing a reduction in weight. Subsequently, the scaffold stabilizes at a new swelling balance (see illustrated in **Figure 9D**). Consequently, the reduced water absorption endows the AlgMA/PLMA ink with superior structural integrity and dimensional stability. The findings demonstrate that AlgMA/PLMA ink exhibits low water absorption, which not only preserves the structural precision achieved through 3D printing but also prevents potential damage to the tissue defect area, thereby avoiding secondary injuries.

Another crucial aspect to consider when assessing a biomaterial's performance is its degradation profile, particularly in terms of preserving its structural integrity over extended periods of use. **Figure 9E** displays the degradation patterns of each AlgMA/PLMA material under a 7-day culture. The data indicates that the AlgMA8 hydrogel exhibited minimal degradation initially, with a gradual onset of degradation commencing on the fourth day. The hypothesis is that the AlgMA

material, after undergoing UV photo-crosslinking, forms a singular network structure that initially exhibits stability. However, in later stages, it becomes susceptible to vibrations and its high hydrophilicity allows a significant influx of water molecules into the scaffold's network structure early on. This leads to AlgMA hydrolysis, resulting in a reduction in the mass of AlgMA8 scaffolds. On the other hand, scaffolds incorporating ε-PLMA showed a loss in mass within the first two days, followed by a stabilization phase; furthermore, the AlgMA/PLMA scaffold underwent more rapid degradation in the initial phase as the amount of ε-PLMA increased, as illustrated in **Figure 9E**. The initial reduction in mass can be attributed to the ε-PLMA small molecule self-crosslinking network that formed on the scaffold's surface, which was gradually removed by the PBS solution through continuous shaking until it completely detached. Subsequently, the impact of ε-PLMA on the mechanical properties of AlgMA hydrogels was evaluated. The stress-strain curve of compression reveals that an increase in the ratio of positive/negative charge led to a corresponding enhancement in the hydrogel's compressive strength (**Figure 9F**). The AlgMA/PLMA hydrogel's mechanical properties are significantly influenced by electrostatic interactions between the opposite charges. It was observed that the AlgMA8 hydrogel exhibited the highest compressive strain. When examining the compressive modulus data, it was noted that there was a progressive increase in the compressive modulus of the scaffold as the content of ε-PLMA was raised, with values of 0.317, 0.454, 0.751, 0.916, and 0.926 MPa for AlgMA8 to AlgMA8-PLMA16, respectively, as shown in **Figure 9G**. Upon calculation, the toughness values for the AlgMA/PLMA hydrogel were determined to be 1731, 1218, 4583, 3152, and 4210 $KJ \cdot m^{-3}$, respectively (**Figure 9G**). This trend can be interpreted by the fact that a higher crosslinking density in the polymer results in stronger intermolecular forces, making the material more resistant to deformation from

external forces.

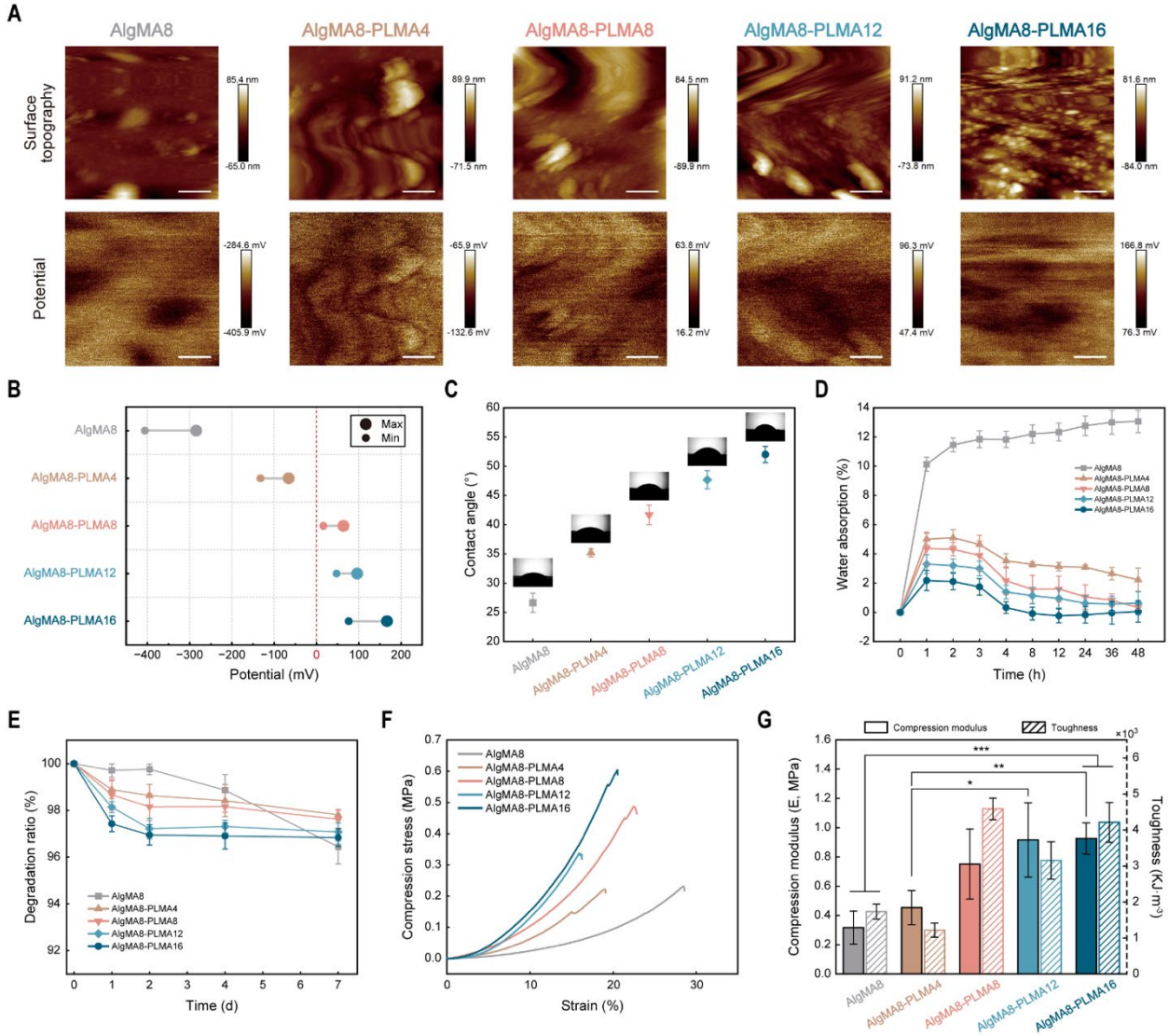

Figure 9. The Physical Properties of AlgMA/PLMA Bioink. A) Analysis of surface topography and potential of AlgMA/PLMA materials. Scale bar in **A**, 400 μm. **B)** Investigation into the impact of ε-PLMA content on the potential range of AlgMA/PLMA materials. **C)** Diagram depicting water contact angle variations for different ratios of AlgMA/PLMA. **D)** Assessment of water absorption ratios for different ratios of AlgMA/PLMA over a 48-hour period. **E)** Study on the degradation of different ratios of AlgMA/PLMA within 7 days. **F)** Evaluation of compression mechanical properties for different ratios of AlgMA/PLMA. **G)** Analysis of compression modulus and toughness for different ratios of AlgMA/PLMA. (*P < 0.05, **P < 0.01, ***P < 0.001)

For extrusion printing, printability of ink is highly influenced by their rheological properties, using to set printing parameters. We conducted the rheological test to find the appropriate printing window of AlgMA/PLMA bioinks. **Figure 10A** displays the shear-thinning behavior of AlgMA/PLMA bioinks. When subjected to a poor shear rate as 0.1 s^{-1}, the incorporation of ε-PLMA caused the composites' viscosity to rise significantly, from 810 to 21948 Pa·s. As the shear rate increased, the viscosity of the mixtures initially experienced a minor uptick before undergoing a steady decrease, indicative of their excellent shear-thinning characteristics. The initial slight increase in viscosity is largely attributed to the unwinding of long-chain AlgMA's polymers. Typically, the strain is necessary for the ink to realize a transition from solid-like phase to liquid-like phase is associated with the printing pressure. As depicted in **Figure 10B**, the modulus of all AlgMA/PLMA inks exhibited a decrease with increasing strain, leading to a phase transition which suggests the bioink will shift from a solid-like to a liquid-like state under extrusion pressure, as indicated by the condition where the storage modulus (G') represents less than the loss modulus (G"). By closely examining the modulus-strain curve within the 35% to 350% strain range, the AlgMA/PLMA series bioinks' phase changing point could be identified. The figure also shows that the yield strain of the AlgMA/PLMA bioinks improved when the cationic crosslinker ε-PLMA was continuously added. In relation with the printing procedure, the pressure required for the bioink extrusion increased as positive/negative charging ratio rose. However, overall, AlgMA/PLMA series bioinks's phase changing points for the were all below 300% strain, suggesting that the inks could be extruded at pressures that are tolerable for cells. To examine how the frequency of the printing air pressure affects the extrusion behavior of the non-Newtonian fluid, we performed a rheological test - "modulus-frequency". As shown in **Figure 10C**, the frequency had a noticeable

impact on the modulus of the AlgMA/PLMA bioinks, which reflects how printing intervals can influence the rheological properties of the inks. In other words, at lower frequencies, the bioink is extruded fewer times within a given time frame. **Figure 10C** indicates that for most bioinks, the transition from a liquid-like to a solid-like phase occurred at a poor frequency, around 1 Hz. This means that during the typical 3D bioprinting process, where gas pressure is applied and released (usually taking less than 1 s to switch the gas pressure), the phase changing of the AlgMA/PLMA bioink proceeds as expected. To identify the ideal printing temperature window, a "modulus-temperature" evaluation was conducted. As depicted in **Figure 10D**, the modulus of the AlgMA/PLMA series bioinks was largely unaffected by temperatures ranging from 4 °C to 40 °C, indicating that the inks maintain stable printing properties across this temperature range (**Figure 10D**). It's widely recognized that having the ability to print across a broad temperature spectrum significantly benefits bioprinting. This flexibility allows for printing at room temperature in the absence of a plug-in heater, or at specific temperatures like 4°C or 37°C to either improve viability or metabolism of cells, tailored to the objectives of the study. During the process of pneumatic extrusion printing, the ink is subjected to cycles of "pressure on/off". To replicate this scenario, a "Cyclic Oscillation" test was conducted. According to the results shown in **Figure 10E**, under high strain, all AlgMA/PLMA series bioinks demonstrated liquid-like characters (G' < G"), aligning with the findings from **Figure 10B**; upon removal of stress, all bioinks promptly reverted to exhibiting solid-like behavior. Furthermore, as the cycle count increased, the modulus of all bioinks remained within a specific range, suggesting that the AlgMA/PLMA series bioinks possess self-healing and self-supporting qualities, alongside robust printing stability.

Following the assessment of the printability of AlgMA/PLMA series bioinks through

rheological test, we conducted an on-machine test to verify these findings. This involved extruding bioinks using a 3D plotter and documenting the filament quality and printing pressure for subsequent analysis. **Figure 10F** illustrates that ε-PLMA on its own was not printable, and the same was true for AlgMA4 and AlgMA4-PLMA4 bioinks. The reason for this is that these bioinks were too fluid; when loaded into a vertical printing syringe, the inks would flow out of the nozzle without any applied pressure. Consequently, only AlgMA/PLMA bioinks with ε-PLMA concentrations of 8%, 12%, and 16% (w/v) were suitable for the manufacturing process. **Figure 10G** illustrates that the printing pressure is predominantly determined by the AlgMA content. Notably, when the AlgMA concentration is fixed at 8% (w/v), the pressure remains consistent, irrespective of variations in ε-PLMA content. To further verify the quantitative character of post-crosslinkers (i.e., methacrylate, MA), we conducted a rheological test using a "UV cure" mode to assess the bioink's light curing efficiency. As indicated in **Figure 10H**, all AlgMA/PLMA bioinks were capable of rapid photocrosslinked no more than 10 seconds, with the elastic modulus increasing as the ε-PLMA content rose. Interestingly, after this initial increase, moduli of the AlgMA8-PLMA12 and AlgMA8-PLMA16 materials experienced a reduction over the subsequent 20 seconds. This decrease may be due to the denser networks formed by AlgMA-PLMA12 and AlgMA-PLMA16 during UV crosslinking, which expelled more water, potentially creating a water-based-mediated lubricated layer that affected measurement against flat plate of the rheometer. The presence of ε-PLMA enhances the crosslinking density of the AlgMA/PLMA series bioinks, resulting in a stiffer hydrogel. The time required for crosslinking was reduced for higher densities of double bonds, as shown in **Figures 9H**, **9I**, and **Figure S3D**.

Using an extrusion-based 3D printer, scaffolds were fabricated with AlgMA/PLMA bioinks,

and the effect of varying charging ratios on the precision of the scaffold structure was investigated. From **Figure 10J**, it is evident that all scaffold groups, with the exception of the AlgMA8-PLMA8 group, were able to retain high fidelity in their cross-structure. Furthermore, as the positive/negative charging ratio grew, the pore size enlarged. This suggests that incorporation of the cationic coupling component ε-PLMA results in more effectively cured scaffold lines. However, AlgMA8-PLMA4 bioink exhibited poor viscosity, which sometimes promoted to the crash of pores during the construction of scaffolds. The original addition of the cationic crosslinker ε-PLMA disrupts the steady of the ink's negatively charged environment, leading to charge neutralization, which in turn causes a reduction in the bioink's viscosity. However, as the positive/negative charging ratio increases further and reaches equilibrium, the environment within the ink starts to become positively charged (as shown in **Figure 9A**). Consequently, the viscosity of the bioink progressively rises in tandem with the growth in solid component concentration. Through mixing procedure, it was found that AlgMA8-PLMA4 bioink was effortless to mix compared to AlgMA8 bioink, whereas AlgMA8-PLMA8 required more effort, aligning with the results from the viscosity-shear rate rheological tests.

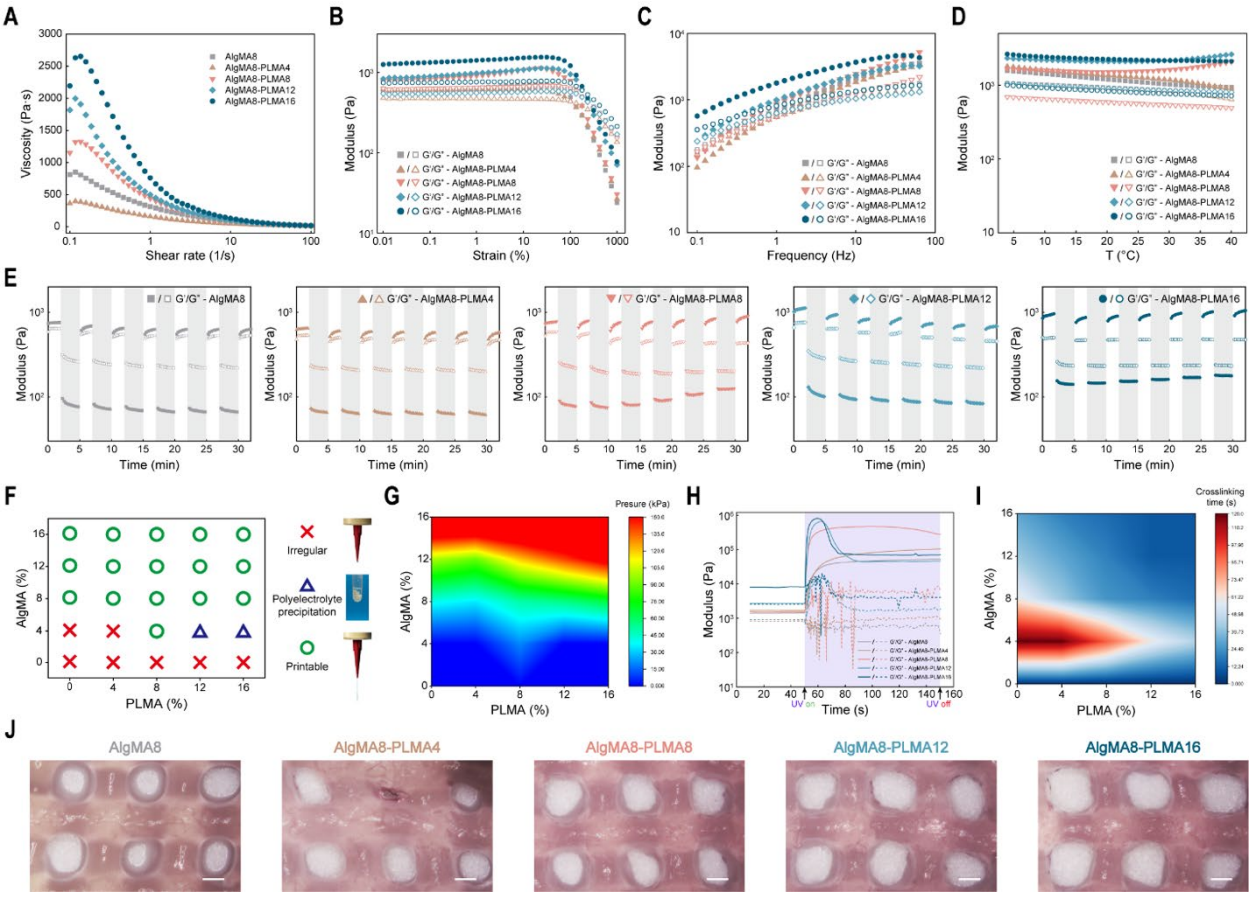

Figure 10. The Printability of AlgMA/PLMA Bioink. A) Assessment of the impact of shear rate (0.1-100 s^{-1}) on the AlgMA/PLMA viscosity. **B)** Examination of the influence of strain (0.01-1000%) on the AlgMA/PLMA's storage and loss modulus (G' and G"). (1 Hz, 25 °C) **C)** Investigation into the effect of frequency (0.1-100 Hz) on the storage and loss modulus (G' and G") of AlgMA/PLMA. (1% strain, 25 °C) **D)** Analysis of the influence of temperature (4-40 °C) on the storage and loss modulus (G' and G") of AlgMA/PLMA. (1% strain) **E)** Testing the shear-thinning and self-healing behavior. Evaluation of the influence of strain cycles (low: unshaded area, 1% strain, 1 Hz; high: shaded area, 500% strain, 1 Hz) on the storage/loss modulus (G'/G") of AlgMA/PLMA. **F)** Analysis of the extrusion status for different ratios of AlgMA/PLMA. **G)** Visualization of the extrusion pressure for different ratios of AlgMA/PLMA using a heat map. **H)** Examination of the influence of UV exposure time (1-100 s, 1% strain) on the storage and loss modulus (G' and G") of AlgMA/PLMA. **I)** Presentation of the photo-crosslinking time for different ratios of AlgMA/PLMA using a heat map. **J)** Evaluation of the effect of different ratios on the structural fidelity of AlgMA/PLMA bio-scaffolds. Scale bar in **J**, 400 μm.

As solid content in the bioink increases, there is a notable rise in the printing pressure

required, while the time needed for crosslinking significantly decreases. When used for cell printing, the high shear force combined with UV light irradiation can lead to cell membrane damage, as well as the potential for DNA mutation and fragmentation. For instance, if AlgMA component concentration is extremely low, the bioink becomes unprintable, as shown in **Figure 10F**. Conversely, as AlgMA component concentration rises, the extrusion pressure increases markedly. Additionally, if the positive/negative charging ratio is excessively high, a polyelectrolyte precipitation can happen. On the other hand, a lower ratio leads to longer photo-crosslinking times for the ink. Through rheological testing and printing pressure assessments, including evaluations of shear-thinning behavior and the determination of a cell-friendly printing range, the most suitable bioinks for 3D bioprinting were identified to be within the range of AlgMA8-PLMA4 to AlgMA8-PLMA12.

In biomedical fields such as organoid development and tissue engineering, the ECM is pivotal in determining cyto-destiny. As a bioink developed for bioprinting, AlgMA/PLMA has demonstrated its proficiency in accurate fabrication. The next critical phase is to explore its interactions with cells. AlgMA/PLMA was combined with bone marrow stromal cells (BMSCs) and then bioprinted into a specific pattern. Subsequently, the viability and proliferation of the cells were monitored over time and in relation to the printing pressure, as shown in **Figure 11** and **Figure S10**.

At the onset of the post-printing period (day 0), cell viability within the AlgMA8-PLMA series scaffolds was recorded at 71.05%, 75.69%, 84.80%, 85.87%, and 83.21%, respectively, as illustrated in **Figures 11A** and **11B**. By day 4, live/dead staining revealed that nearly all cells within the AlgMA8 scaffold had perished (**Figure 11A**). However, the addition of the cationic crosslinker

ε-PLMA enhanced cell viability within the scaffold, with a modest number of cells remaining alive in the AlgMA8-PLMA4 scaffold. Furthermore, as the level of positive charges increased, a greater number of cells were observed to proliferate and disperse within the scaffolds, as shown in **Figures 11C** and **11D**. After a 7-day culture period, there was a noted reduction in cell numbers within the AlgMA8-PLMA16 scaffold compared to day 4, whereas the AlgMA8-PLMA8 and AlgMA8-PLMA12 scaffolds did not exhibit a decrease in cell numbers (**Figure 11A**).

In agreement with the live/dead staining observations, both the CCK8 assay and EdU staining confirmed that a substantial number of cells within the AlgMA8 cell scaffolds perished on the first day of culture, with minimal cell proliferation observed during the assessment period (**Figure 11A** and **11E**). However, the introduction of the cationic crosslinker ε-PLMA markedly enhanced cell survival in the scaffolds; notably, in scaffolds with a positive to negative charging ratio exceeding 1:1, cell proliferation surged on the fourth day, with AlgMA8-PLMA8 scaffolds showing the highest level of cell growth. On comparing the fourth day results, the optical density (OD) values for AlgMA8-PLMA12 and AlgMA8-PLMA16 cell scaffolds declined, with AlgMA8-PLMA16 scaffolds experiencing a more pronounced decrease in living cell numbers; AlgMA8-PLMA8 cell scaffolds, however, continued to exhibit signs of cell proliferation (**Figure 11E**). The experimental findings from this section indicate that the cationic crosslinker ε-PLMA significantly enhances cell viability in bioinks containing 8% sodium alginate.

To investigate the impact of ε-PLMA on cell morphology within the printed scaffolds, immunofluorescence (IF) staining was conducted on the fourth day after printing to visualize the fibrous actin and nuclei of cells embedded in AlgMA/PLMA bio-scaffolds, as shown in **Figure 11A**. Observations from **Figure 11A** revealed that the AlgMA8 cell scaffold contained a very low

number of cells, all of which appeared round in shape. This round shape is attributed to the biologically inert nature of the polyanionic AlgMA, which lacks cell adhesion motifs, thereby hindering cellular processes such as spreading and proliferation. However, with the addition of the cationic crosslinker (ε-PLMA), cells within the AlgMA/PLMA cell scaffolds adopted an elongated, spindle-like shape, indicating the onset of cell spreading. This suggests that ε-PLMA effectively counteracts the biological inertness of AlgMA and enhances cell adhesion within the scaffold, as depicted in **Figures 11A** and **11D**. In the AlgMA8-PLMA12 and AlgMA8-PLMA16 scaffolds, there was a noted decrease in cell numbers by day 7, which is likely due to the reduced pore size illustrated in **Figure S9**, leading to constraints on nutrient and oxygen exchange.

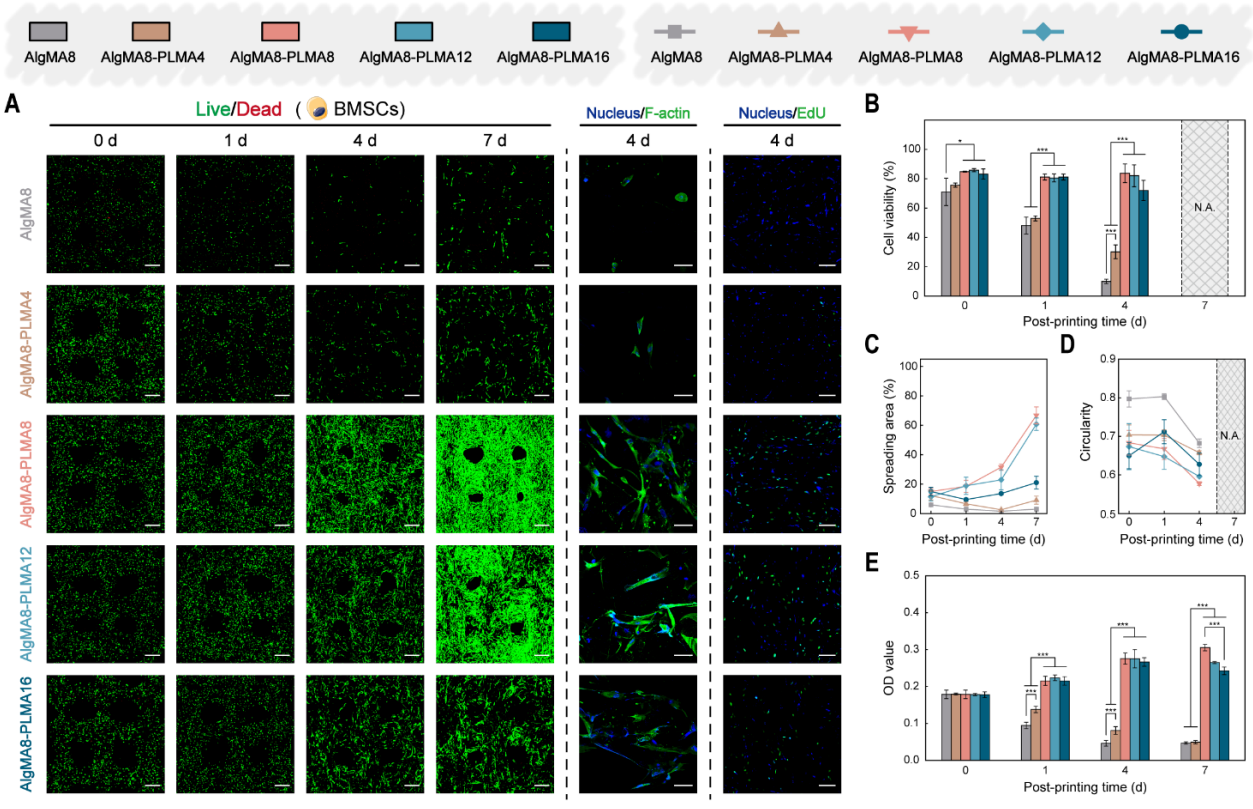

Figure 11. The Cell Behavior Regulation of AlgMA/PLMA Bioink. A) Live/dead fluorescent images depicting hBMSCs printed in AlgMA/PLMA scaffolds with various ratios over a 7-day period (green: live cells, red: dead cells). Scale bar, 400 μm. Cell morphology

of hBMSCs in different ratios of AlgMA/PLMA scaffolds on day 4 is shown (green: F-actin, blue: nucleus). Scale bar, 50 μm. Cell proliferation of hBMSCs in different ratios of AlgMA/PLMA scaffolds on day 4 is displayed (green: EdU, blue: nucleus). Scale bar, 100 μm. **B)** Evaluation of cell viability for hBMSCs printed in AlgMA/PLMA scaffolds with different ratios over a 7-day period. **C)** Analysis of cell spreading area for hBMSCs printed in AlgMA/PLMA scaffolds with different ratios over a 7-day period. **D)** Assessment of circularity for hBMSCs printed in AlgMA/PLMA scaffolds with different ratios over a 7-day period. **E)** Measurement of cell proliferation (cck-8 assay) for hBMSCs in AlgMA/PLMA scaffolds with different ratios over a 7-day period. (*P < 0.05, **P < 0.01, ***P < 0.001)

Overall, incorporating the cationic crosslinker ε-PLMA significantly enhances cell survival and adhesion within the AlgMA/PLMA scaffold. This effect, observed with the use of ε-PLMA, associates with findings from other research groups' prior investigations [141, 157]. In previous studies, we discovered that ε-PL modified alginate can facilitate protein adsorption and cell attaching/spreading. Nevertheless, thanks to the use of EDC-NHS for crosslinking, the biomaterial was unsuitable for use as a cell-printing ink [141]. The role of electrostatic forces is pivotal in facilitating cell attachment, which promotes cell bonding and initiates the interaction with focal adhesion molecules on biomaterials. Moreover, proteins serve as crucial intermediaries in the direct interaction between cells and materials. Under physiological conditions, proteins typically carry a negative charge and tend to accumulate on surfaces that are positively charged [158]. Tan and colleagues enhanced a poly(ethylene glycol)-diacrylate (PEGDA) hydrogel by incorporating the positively charged monomer 2-(methacryloyloxy)ethyl-trimethylammonium chloride (MAETAC) [159]. This adjustment in the microenvironment led to a 2.6-fold increase in protein adsorption, which, in turn, significantly improved the adhesion of MC3T3-E1 cells and their osteogenic differentiation [159]. Multiple mechanisms that influence cellular responses have been linked to changes in the hydrophilicity of hydrogels, as well as potential alterations, as indicated in **Figure 11C**. Previous studies have suggested that a moderately hydrophilic surface on biomaterials can

promote cell proliferation and offer improved biocompatibility [160, 161]. Research on cell adhesion to hydrophilic substrates has identified an optimal water contact angle (WCA) range of 40° to 70° for cell attachment [162, 163]. This implies that the surface free energy of a material must fall within a specific range to be conducive to cell growth. In other words, excessive hydrophilicity may lead to cell detachment [162, 163], and the WCA of AlgMA8 at 26.64° is significantly lower than this optimal range. One of the contributing factors to the biological passivity of AlgMA is the presence of numerous hydrophilic groups, such as -COOH and -OH, which can impede cell adhesion [141]. The addition of the cationic crosslinker ε-PLMA has markedly ameliorated this issue.

3.3.2 Vessel Bioink – G-GelMA

For direct printing of vascular structure, in order to form a hollow structure with high fidelity shape, in addition to certain shear thinning and self-healing properties of materials, there is also a certain requirement for the speed of thinning and healing, that is, high thixotropy. At the same time, the construction of large vascular networks requires ink to have a certain self-supporting performance to prevent structural dislocation during the fabrication process.

To fulfil the requirement, G-GelMA bioink were selected (**Figure 12A**). The GelMA bioink also showed great rheological behavior for extrusion bioprinting (**Figure 12B-F**). Similar with AlgMA/PLMA bioinks, we also tested the best printing range for G-GelMA series bioinks (**Figure 12G** and **12F**). Also, the printed structure showed clear filament and mesh size which reflected the high printability of G-GelMA (**Figure 12I** and **12J**).

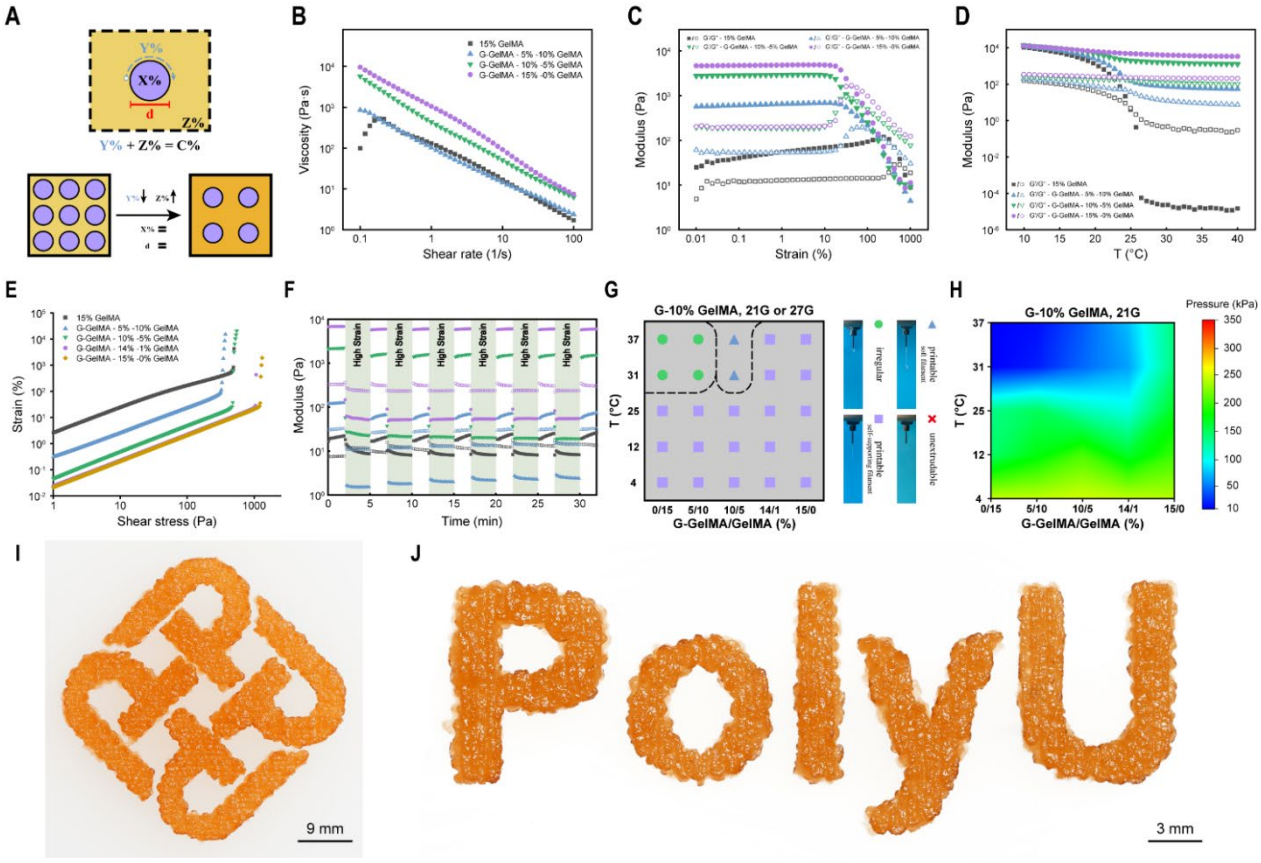

Figure 12. The Printability of the Vessel Bioink. A) The diagram of granular gelatin-based photo-crosslinking materials. **B)** The shear-thinning property of series of G-GelMA. **C)** The relationship between storage/loss modulus (G'/G") and strain. **D)** The relationship between G'/G" and temperature. **E)** The relationship between strain and shear stress. **F)** Shear-thinning and self-healing behavior analysis. Influence of strain-cycle (low: unshaded, 1% strain, 1 Hz and high: shaded, 500% strain, 1 Hz) on the (G'/G") of G-GelMA. **G)** The analysis of extrusion status of different ratio of G-GelMA. **H)** The extrusion pressure of different ratio of G-GelMA in heat map. **I)** and **J)** The real picture of printed PolyU Logo scaffold (I) and alphabet "PolyU" (J). Scale bar in **I** and **J**, 9 mm and 3mm, respectively.

Furthermore, we also tested the basic physical properties of G-GelMA. The high water-absorption behavior could provide a high-water-content environment to improve the biocompatibility (**Figure 13A**). However, the existence of microgel would break the consistency of the polymer network resulting in a decrease in hydrogel's mechanical properties (**Figure 13B**

and **13C**). The high printability and biocompatibility of G-GelMA were also confirmed (**Figure 13D** and **13E**).

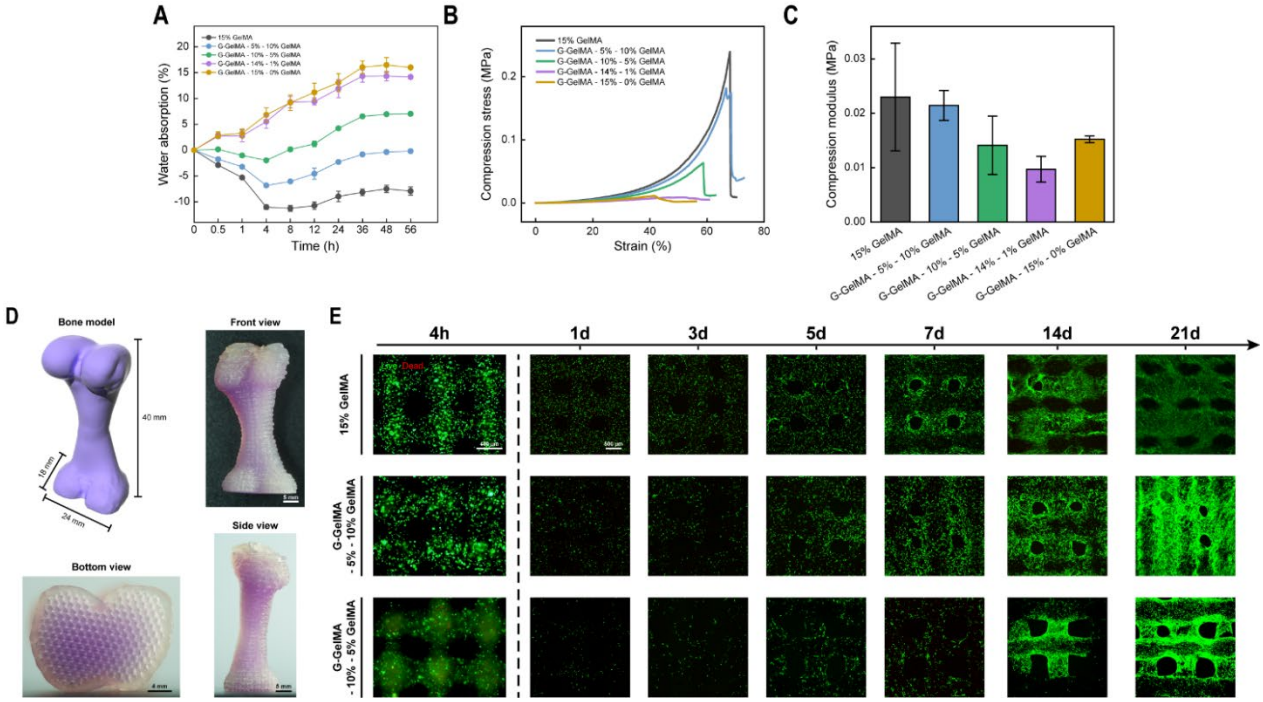

Figure 13. The Mechanical Properties and Biocompatibility of the Vessel Bioink. A) Water absorption ratio of different ratio of G-GelMA within 48 hours. **B)** Compression mechanical properties of different ratio of G-GelMA. **C)** Compression modulus of different ratio of G-GelMA. **D)** The real picture of printed bone-like scaffold. **E)** The cell viability on after printing and culture by 4 hours, 1, 3, 5, 7, 14 and 21 days. Scale bar, 400 μm.

Furthermore, we proved the printability and biocompatibility of GelMA bioink for coaxial bioprinting (**Figure 14**). After a 14d culture, the hBMSCs have proliferated and fulfilled the surface of the hydrogel tube (**Figure 14A**). However, the proliferation inside the hydrogel was slow, due to the limitation on nutrient diffusion from the hydrogel wall thickness.

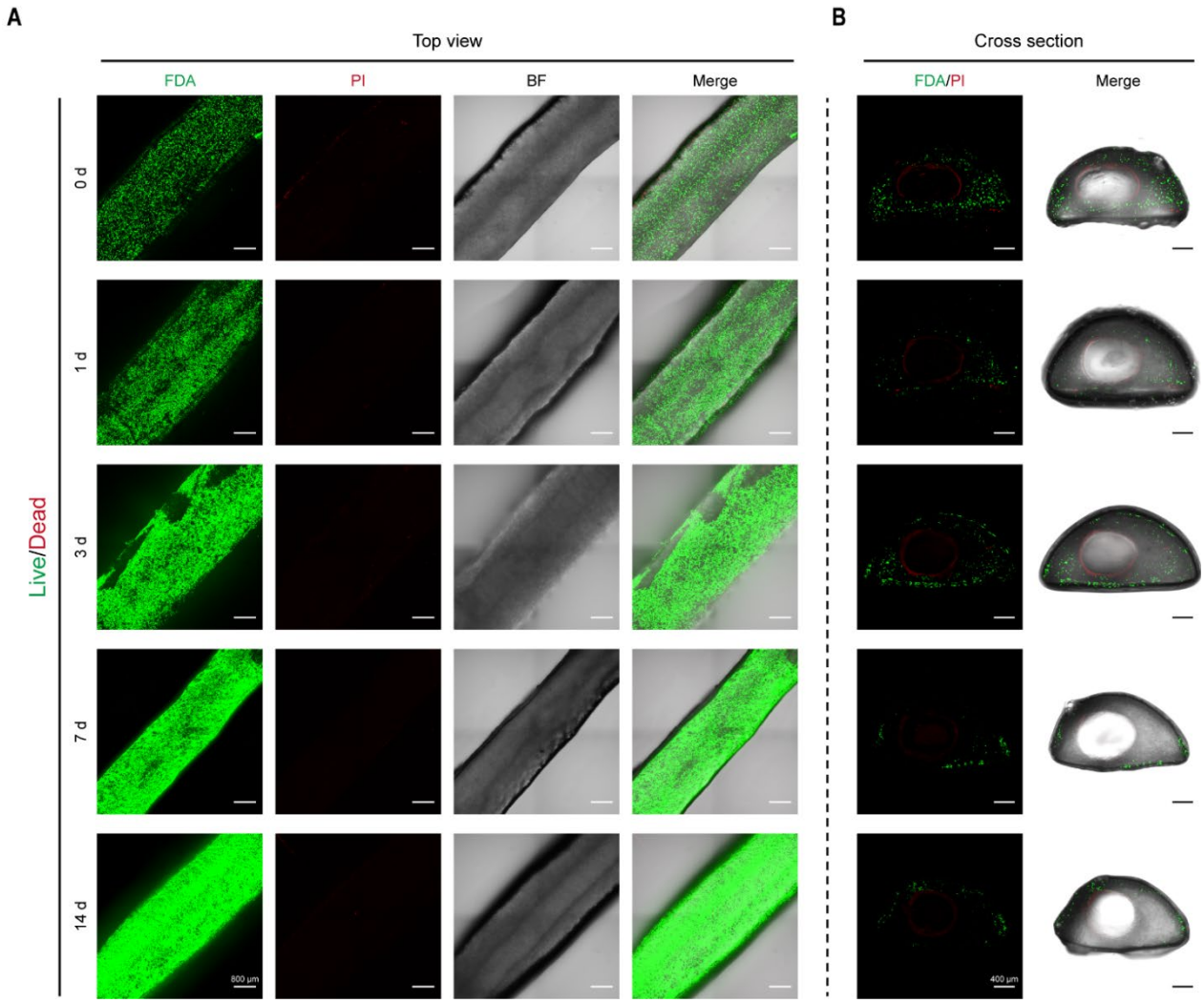

Figure 14. The Biocompatibility of Coaxial Bioprinting. A) The top view of live/dead staining of coaxial bioprinting. **B)** The cross section of live/dead stained bio-tubule. Scale bar, 400 µm.

3.3.3 Biofabrication of Joint-on-a-Chip

The real printed cartilage zone, bone zone and blood vessel channel were showed in **Figure 15A**. By using SLA, chip chamber for synovial flow was printed (**Figure 15B**). through printing a single hollow channel in synovial chamber, we checked the perfusablility and seamless of the chip (**Figure 15C**). Furthermore, the chip was designed to be integrated into confocal microscopy for future analysis (**Figure 15D**).

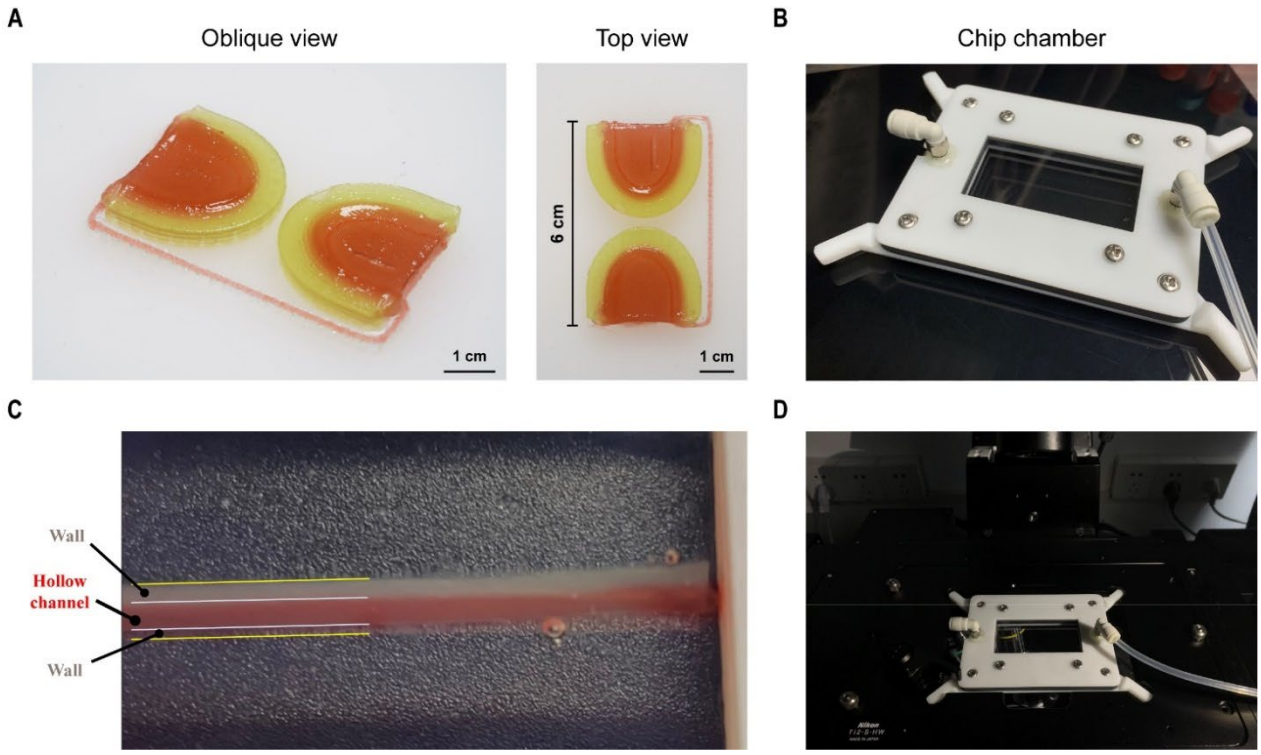

Figure 15. The Assemble of Joint-on-a-Chip. A) Real printed cartilage zone (green), bone zone (brown) and blood vessel (red). **B)** Real printed synovial chamber for flow culture. **C)** Perfusable vessel channel with permeable wall. **D)** Integration of joint-on-a-chip and confocal microscopy.

Chapter 4: Conclusions and Perspective for Future Research

4.1. Limitations and Perspectives

In this thesis, we have made a first step on the manufacture of the joint-on-a-chip model. However, there are still a few limitations in current study. First, the long-time culture viability still needs to be confirmed. We will directly print several cell types in to this joint-on-a-chip and investigate the cell activity. Second, the relationship between biomaterials and cell activity still needs to be clarified *via* a time-lapse investigation on the cytoskeletal and biomarkers. Finally, to further use this joint-on-a-chip for drug screening, an OA disease model should be set up for comparable analysis with healthy joint-on-a-chip model. A possible plan of this research is listed as below:

4.1.1 Test of Functional Unit (Single-cell-type Model)

As mentioned in former section, there are many OA risk factors. By using our joint-on-a-chip system, we can do high throughput screening for these factors. In **Figure 16**, we selected three potential risk factors, those are High shear force, inflammation, obesity (diabetes). To mimic such environment, we will introduce high synovial flow velocity, IL-1β, and high glucose condition into the joint system vis those double circulation system, respectively.

To characterize the function of our joint system, several tools will be used, as below:

Doppler ultrasound – Flow dynamics

Micro-CT – Osteophytes

Calcium signaling – Shear force

PCR – OA Markers; Western blot – OA Markers; ELISA – Fluid components analysis

Test markers in synovial/blood fluid:

biochemical analysis (TNF-α, IL-1β, IL-2, IL-6, IL-10, INF-γ, TGF-β)

Biomarker from cells and double fluids:

CRP, pyridinoline, YKL-40, NF-κB, MMP-3, MMP-13, and TIMP-1

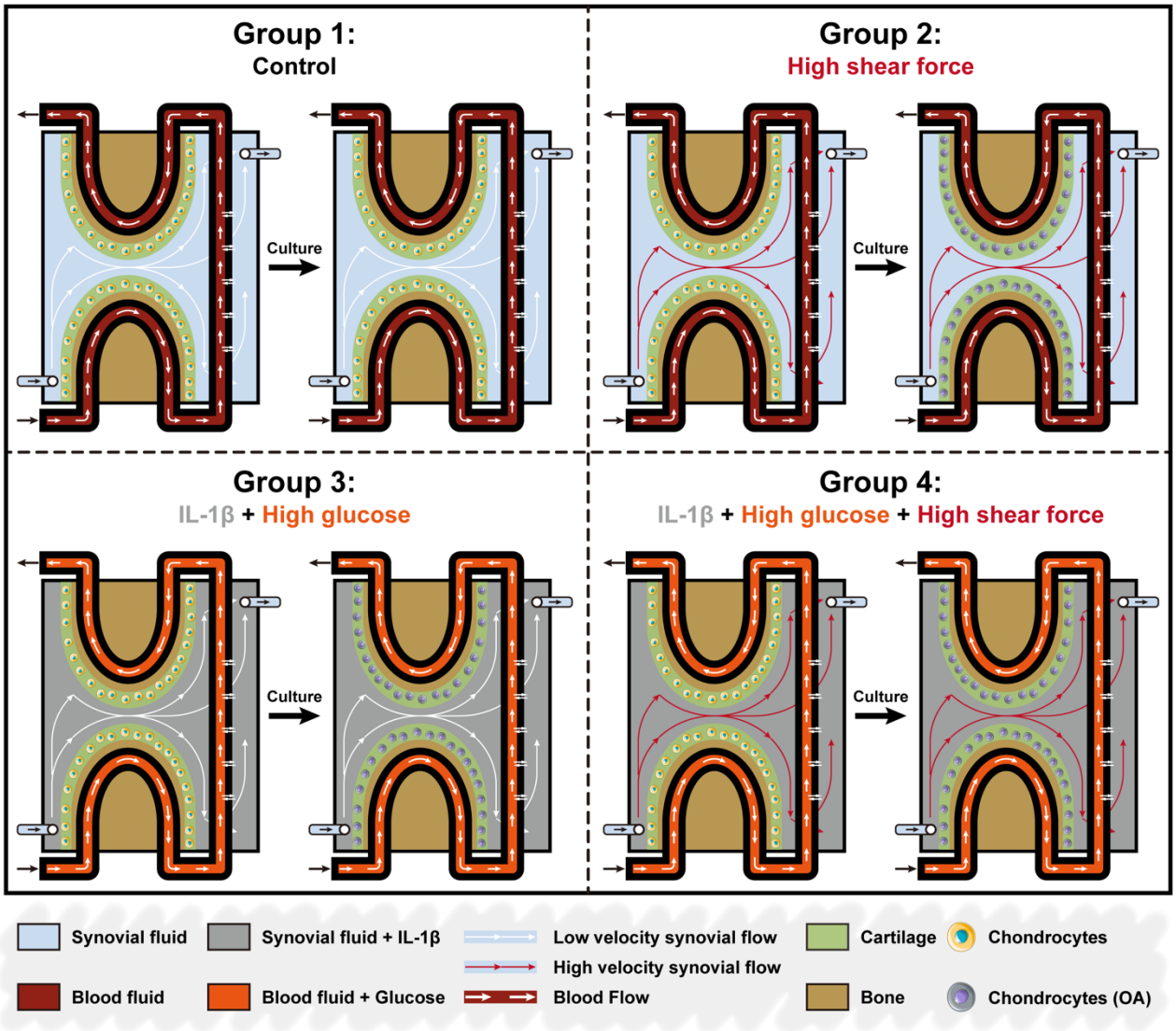

Figure 16. Test of Functional Unit. The OA risk factors screening.

4.1.2 Test of Microphysiological System (Multi-cell-type Model)

To test the microphysiological system of joint-on-a-chip, we can introduce multi-cell tissue into this joint system. For example, we can seed OA synovial fibroblast cells in the synovial chamber beside the healthy chondrocyte (**Figure 17**). After a long-time co-culture, the phenotype of the chondrocyte can be characterized to verify the function of the joint-on-a-chip.

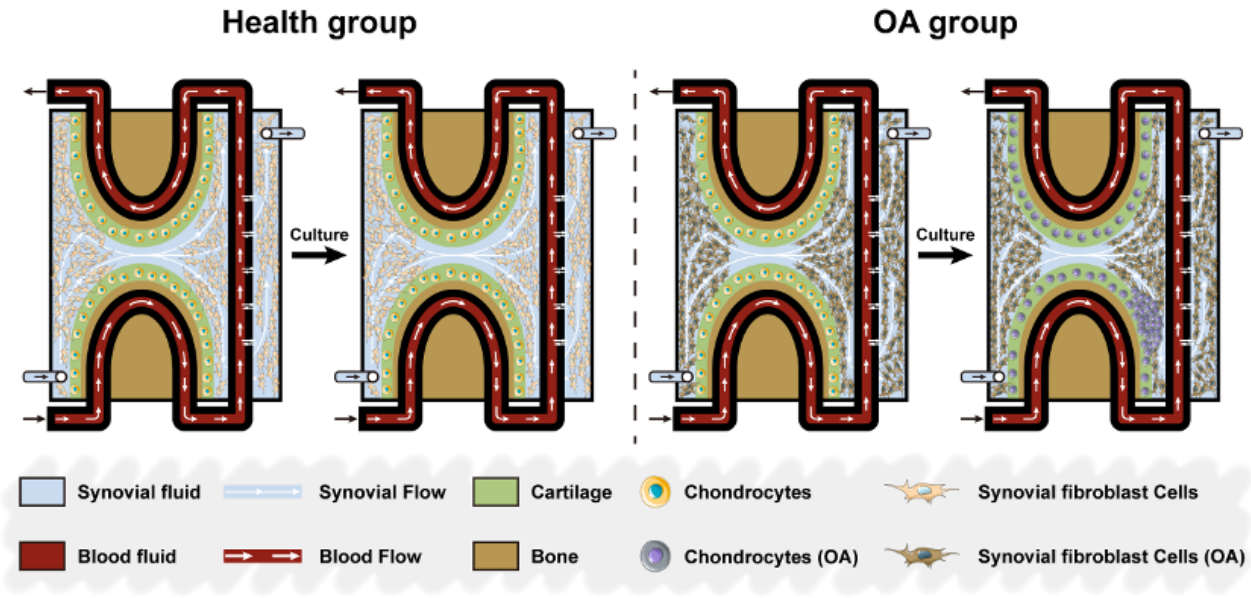

Figure 17. Test of Microphysiological System. Multi-cell interaction.

4.1.3 Disease model

As reported by some articles, the lifetime risk of symptomatic knee OA is greater in obese persons (body mass index ≥ 30) than in nonobese persons (19.7% vs 10.9%).[164] Further, some research have reported that high glucose environment could increase the risk of OA.[165]

Since this joint-on-a-chip has a double circulation channel, we can add more glucose in the blood vessel to obtain a high glucose microenvironment (**Figure 18A**). In this situation, the osteocytes and chondrocytes may show pathological characters. The disease model or even the OA

model could be built for further research.

To build up the disease model successfully, a back-up plan was made on the disease model construction. We chose a factor called IL-10 which could be added into the blood or synovial flow for chondrocytes to show aging and apoptosis, arthritis phenotype. This is a common protocol for generating OA disease model in vitro.

Aging phenotype: *β-Galactosidase Staining:* Senescent cells express β-galactosidase in a pH-dependent manner, specifically detectable at pH = 6.[166] It is ideal for quick and easy detection of multiple cell populations or tissue samples, with straightforward orientation and bright, clear blue staining.

Apoptosis phenotype: *DAPI/Hoechst 33342 Staining:* These two kits could stain cell nuclear. The apoptotic cells could be verified by analysing the nuclear morphology, if there is any nuclear membrane damage and spill out; *Caspase-3:* The apoptosis pathway is regulated layer by layer by a set of well-defined signalling pathways. In most cases, all apoptotic signals will converge to the final executor of apoptosis, Caspase-3. The upstream apoptotic signal cleaves Caspase-3, making it enzymatically active and executing the final apoptotic program. Using antibodies to do Western blot, immunohistochemistry or immunofluorescence for qualitative or relative quantification.

Osteoarthritis phenotype: A 'burden of disease' marker assesses the severity or extent of OA, typically at a single time point, among affected individuals. Levels of MMP-3, IL-6 and TNF-α could be detected as increase in OA phenotype.[167, 168]

Step 1: Disease inducing factor selection

Step 2: Disease inducing factor concentration selection

Step 3: Perfusion culture: Control group (health model) and Experimental group (disease model)

Step 4: Pathological characters detection: Aging, Apoptosis and Osteoarthritis. If there is any increase in these properties.

4.1.4 Drug Screening Model

New drug could be verified in this drug test model by mix it into blood flow or synovial flow (**Figure 18B**). If the pathological characters could be removed or reduced, this drug could be seen as a promising solution for OA or other joint disease. In this research, we will test several kinds of drug from small molecule drugs to gene therapy drugs.

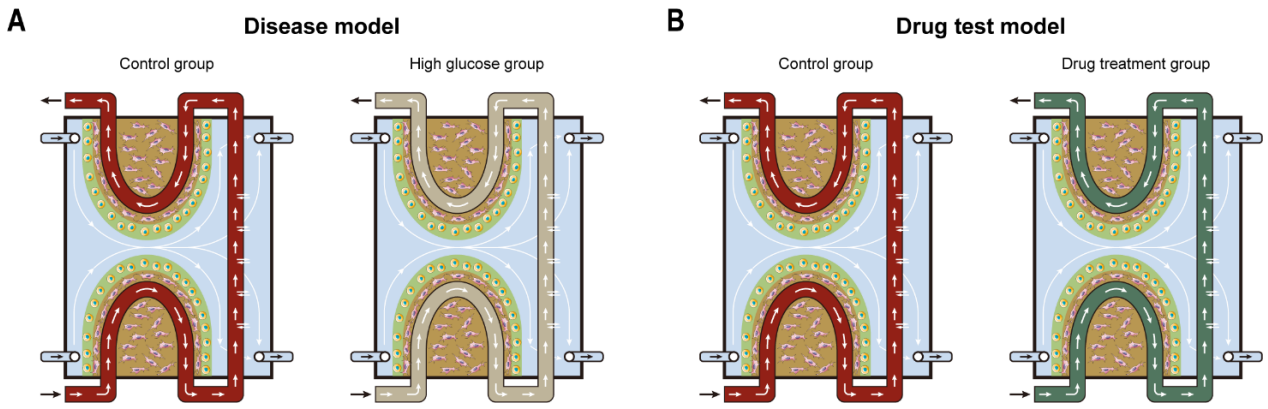

Figure 18. The Possible Application Joint-on-a-Chip in Future. A) The diagram of disease model establishment. **B)** The diagram of drug screening model establishment.

Step 1: Drug selection

Step 2: Drug dose confirmation

Step 3: Perfusion culture: Control group (disease model) and Experimental group (drug treatment model)

Step 4: Pathological characters detection: Aging, Apoptosis and Osteoarthritis. If there is any decrease in these markers or properties.

4.2. Conclusions

In conclusion, we have designed a joint-on-a-chip model with double circulation system. To manufacture this joint tissue *in vitro*, we developed AlgMA/PLMA bioink and G-GelMA bioink for cartilage/bone and blood vessel fabrication, respectively. These two kinds of bioinks have shown good printability and biocompatibility. In our future work, we will integrate hBMSCs and chondrocytes in Bioink 1 and HUVECs in Bioink 2 to fabricate cell-laden joint-on-a-chip for OA pathology research and drug screening. Through using this chip, we will try to evaluate the OA *in vitro*.

Appendices

Fourier Transform Infrared Spectrometer (FTIR): Sample preparation steps: under the infrared drying lamp, the dried Alg, AlgMA, ε-PL and ε-PLMA samples were mixed with potassium bromide (KBr) and ground evenly, and pressed into thin slices for testing. The scanning wavelength range was from 400 to 4000 cm^{-1}. Each sample was scanned for 64 times. The resolution was 2 cm^{-1}.

^{1}H and ^{13}C Nuclear Magnetic Resonance (^{1}H and ^{13}C NMR): The original Alg/ε-PL and synthesized AlgMA/ε-PLMA samples were tested by ^{1}H NMR or ^{13}C NMR with a nuclear magnetic resonance spectrometer (AVANCE III 400, Bruker, Inc.) [169]. NMR sample preparation steps: Using D_2O as solvent, the dried samples were fully dissolved respectively, then transferred into NMR tubes, and covered with NMR caps for testing. The dissolved concentration is 10 mg/mL and 15mg/ml for ^{1}H NMR and ^{13}C NMR, respectively.

Calculation of AlgMA and ε-PLMA Double Bond Substitution Degree: It can be seen from **Figure S1A** that due to the double bond substitution of -OH on Alg, that is, the hydrogen proton of -OH on the C2 or C3 position was replaced by C7-10, forming AlgMA. Therefore, through the ^{13}C NMR test, the C1-6 position of the original compound Alg and the carbon atom characteristic peaked at the C7-10 position of the substituted compound AlgMA can be integrated to calculate the double bond substitution degree DS of the synthesized AlgMA. The specific calculation process was shown in **Equation S1**:

$$DS\ (AlgMA) = \frac{Integral\ sum\ of\ C7\sim10/6}{Integral\ sum\ of\ C1\sim6/4}, \text{(S1)}$$

It can be seen from **Figure S2A** that due to the double bond substitution of -NH_2 on ε-PL,

that is, a hydrogen proton at position 11 was replaced by C12-15, forming ε-PLMA. Therefore, through the ^{1}H NMR test, the C4-6 position of the original compound ε-PL and the hydrogen atom characteristic peaked corresponding to the C15 position of the substituted compound ε-PLMA can be integrated to calculate the double bond DS of the synthesized ε-PLMA. The specific calculation process was shown in **Equation S2**:

$$DS\ (\varepsilon - PLMA) = \frac{Integral\ sum\ of\ C12/2}{Integral\ sum\ of\ C3{\sim}5/6}, \text{(S2)}$$

Gel Permeation Chromatography (GPC): The original Alg/ε-PL and synthesized AlgMA/ε-PLMA samples were tested by GPC using gel permeation chromatography, and the molecular weights of Alg, AlgMA, ε-PL and ε-PLMA samples were analyzed. Preparation steps of GPC samples: Firstly, samples were dissolved in ddH_2O to prepare solutions. The concentration of each polymer was 1.00 mg/ml; then, ddH_2O was used as mobile phase for GPC test. The sample was tested under a 1.00 mL/min mobile phase flow rate, and the temperature was 37 °C. GPC data analysis: Through GPC testing, the number-average molecular weight (Number-average Molecular Weight, Mn) and weight-average molecular weight (Mass-average Molecular Weight, Mw) of the sample can be obtained, respectively, and the polymer dispersion index (PDI) can be calculated as **Equation S3**:

$$PDI = \frac{Mw}{Mn}, \text{(S3)}$$

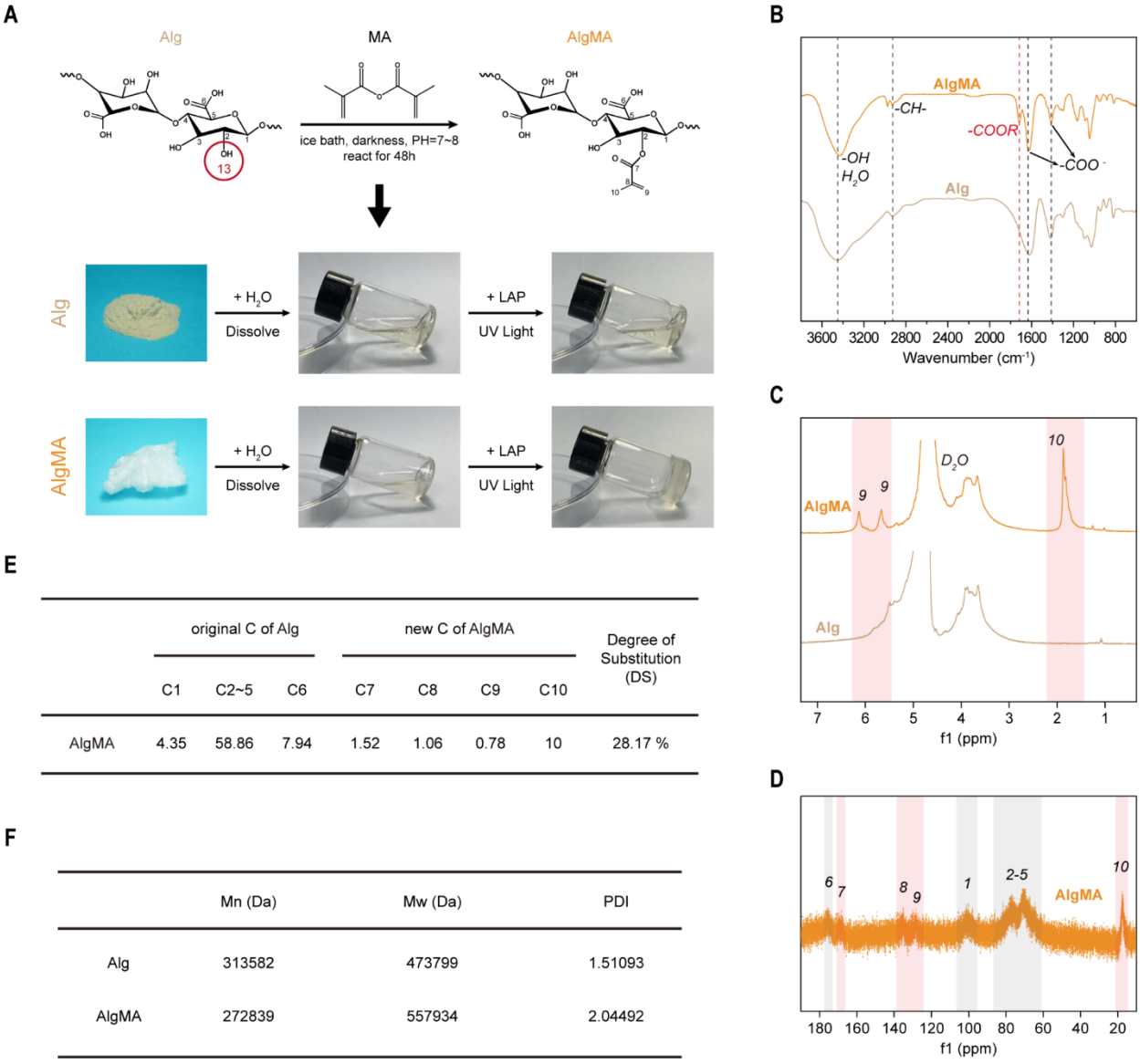

E

	original C of Alg			new C of AlgMA				Degree of Substitution (DS)
	C1	C2~5	C6	C7	C8	C9	C10	
AlgMA	4.35	58.86	7.94	1.52	1.06	0.78	10	28.17 %

F

	Mn (Da)	Mw (Da)	PDI
Alg	313582	473799	1.51093
AlgMA	272839	557934	2.04492

Figure S1. The Synthesis and Characterization of AlgMA. A) The synthesis process of AlgMA from Alg and the show of successful modified polymer with double-bond. **B)** FTIR spectrum of Alg and AlgMA. **C)** ^{1}H NMR spectrum of Alg and AlgMA. **D)** ^{13}C NMR spectrum of AlgMA. **E)** The overview of the signal integrations and degree of substitution (DS) for AlgMA. **F)** The molecular weights of Alg and AlgMA.

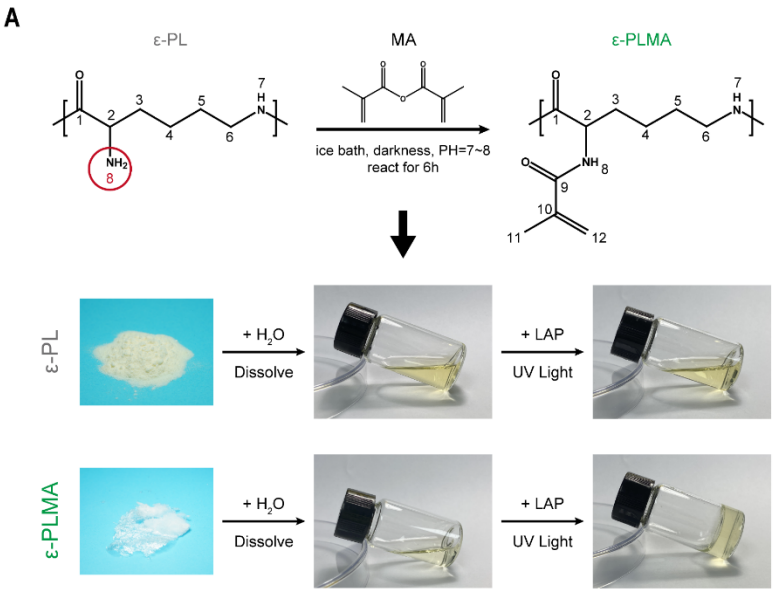

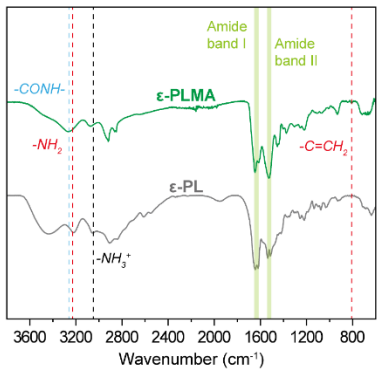

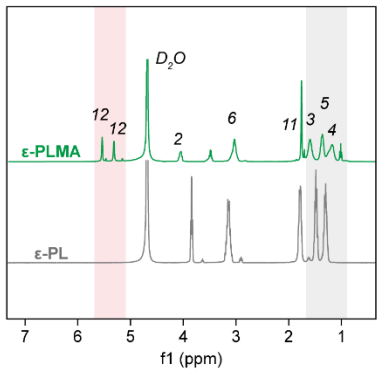

D

	original H of ε-PL	new H of ε-PLMA		Degree of Substitution (DS)
	H on C3~5	H_1 on C12	H_2 on C12	
ε-PLMA	196.53	10	10.08	30.65 %

E

	Mn (Da)	Mw (Da)	PDI
ε-PL	575	578	1.00522
ε-PLMA	821	824	1.00365

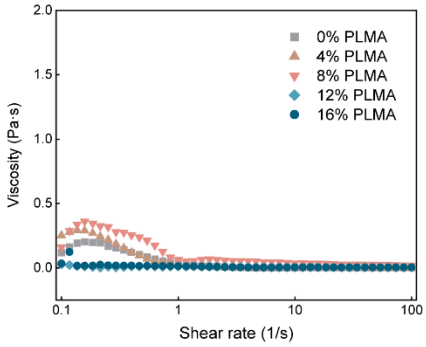

Figure S2. The Synthesis and Characterization of ε-PLMA. A) The synthesis process of ε-PLMA from ε-PL and the show of successful modified polymer with double-bond. **B)** FTIR spectrum of ε-PL and ε-PLMA. **C)** ^{1}H NMR spectrum of ε-PL and ε-PLMA. **D)** The overview of the signal integrations and degree of substitution (DS) for ε-PLMA. **E)** The molecular weights of ε-PL and ε-PLMA. **F)** Influence of shear rate (0.1-100 s^{-1}) on the viscosity of ε-PLMA.

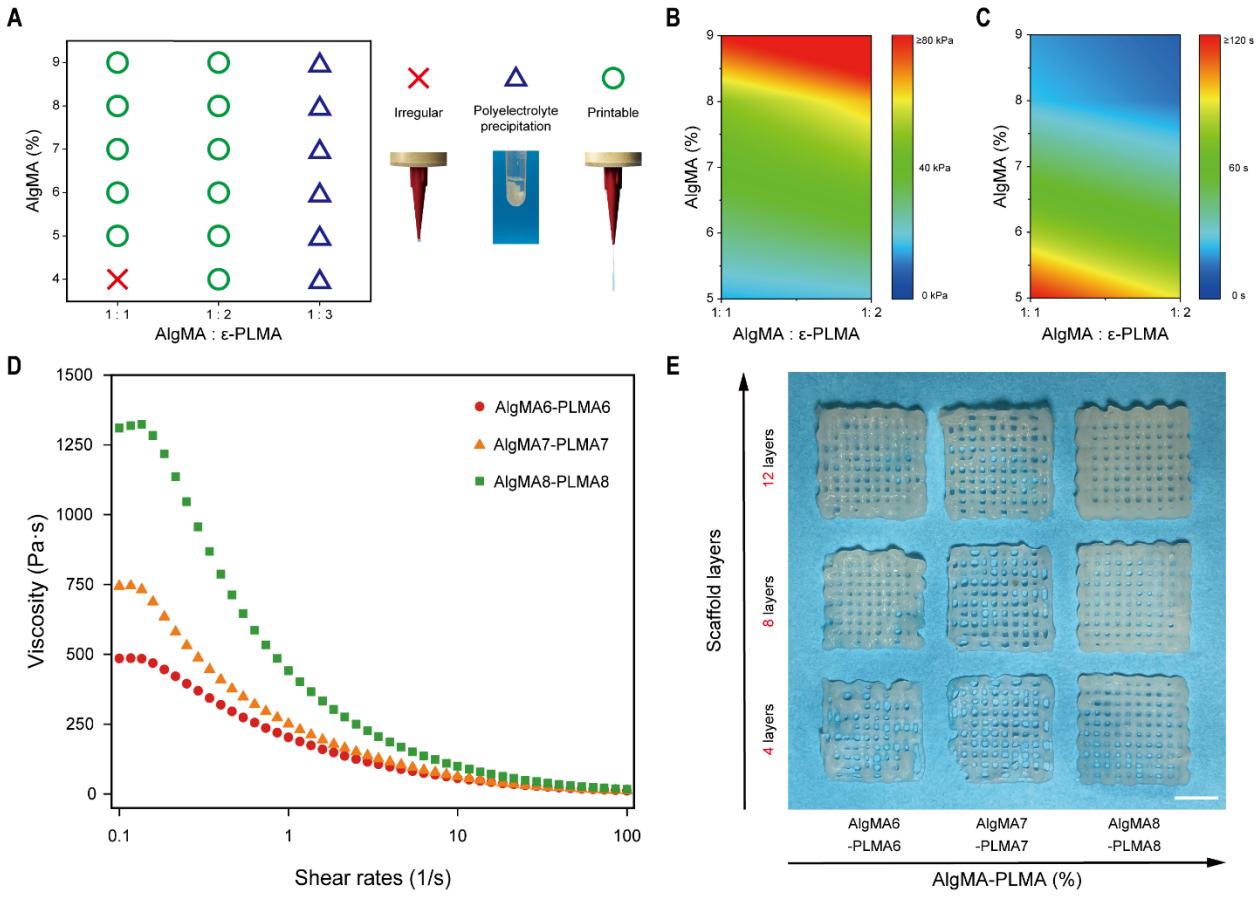

Figure S3. The Printability of Blend Bioink with Series Ratio between AlgMA and ε-PLMA. A) The analysis of extrusion status of different AlgMA/ε-PLMA bioinks. **B)** The printing extrusion pressure of different AlgMA/ε-PLMA bioinks in heat map. **C)** The photo-crosslinking time of different AlgMA/ε-PLMA bioinks in heat map. **D)** The rheological test of shear-thinning behavior of AlgMA/ε-PLMA (1:1) bioinks with different solid contents. **E)** The effect of different solid content on accuracy of structure for AlgMA/ε-PLMA (1:1) scaffolds. Scale bar in **E**, 5 mm.

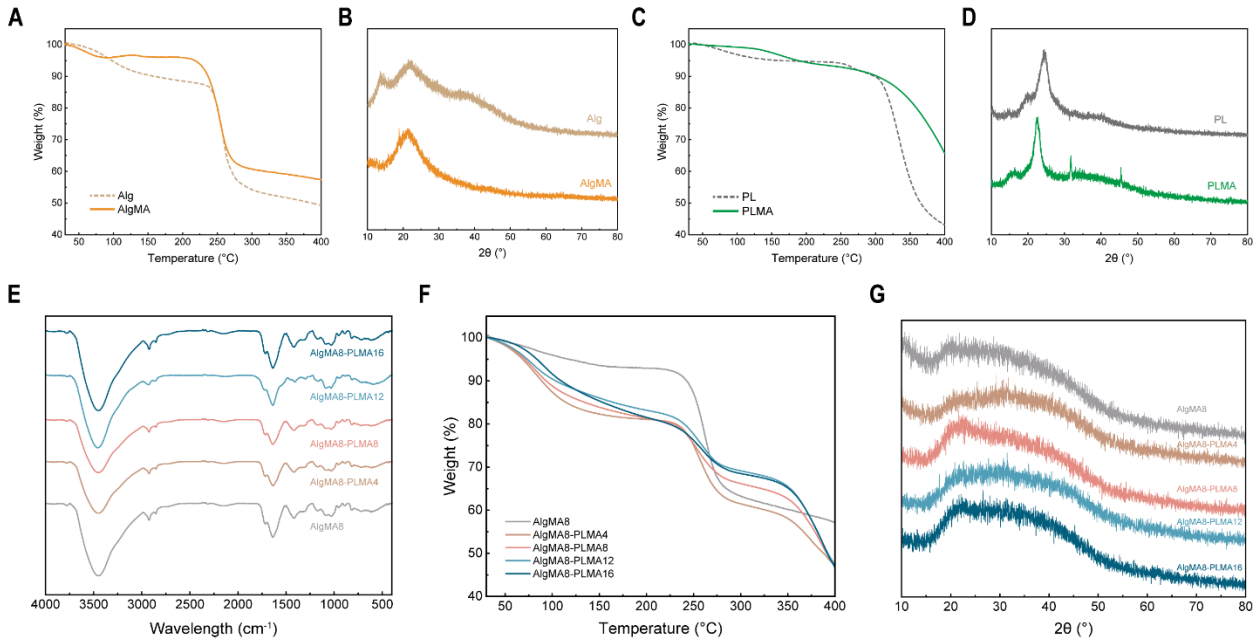

Figure S4. The Chemical Properties of Synthesized AlgMA, ε-PLMA and Blend Ink. **A)** Thermogravimetric analysis of Alg and AlgMA. **B)** X-ray diffraction analysis (XRD) of Alg and AlgMA. **C)** Thermogravimetric analysis of ε-PL and ε-PLMA. **D)** X-ray diffraction analysis (XRD) of ε-PL and ε-PLMA. **E)** FTIR spectrum of different ratio of AlgMA/ε-PLMA. **F)** Thermogravimetric analysis of different ratio of AlgMA/ε-PLMA. **G)** X-ray diffraction analysis (XRD) of different ratio of AlgMA/ε-PLMA.

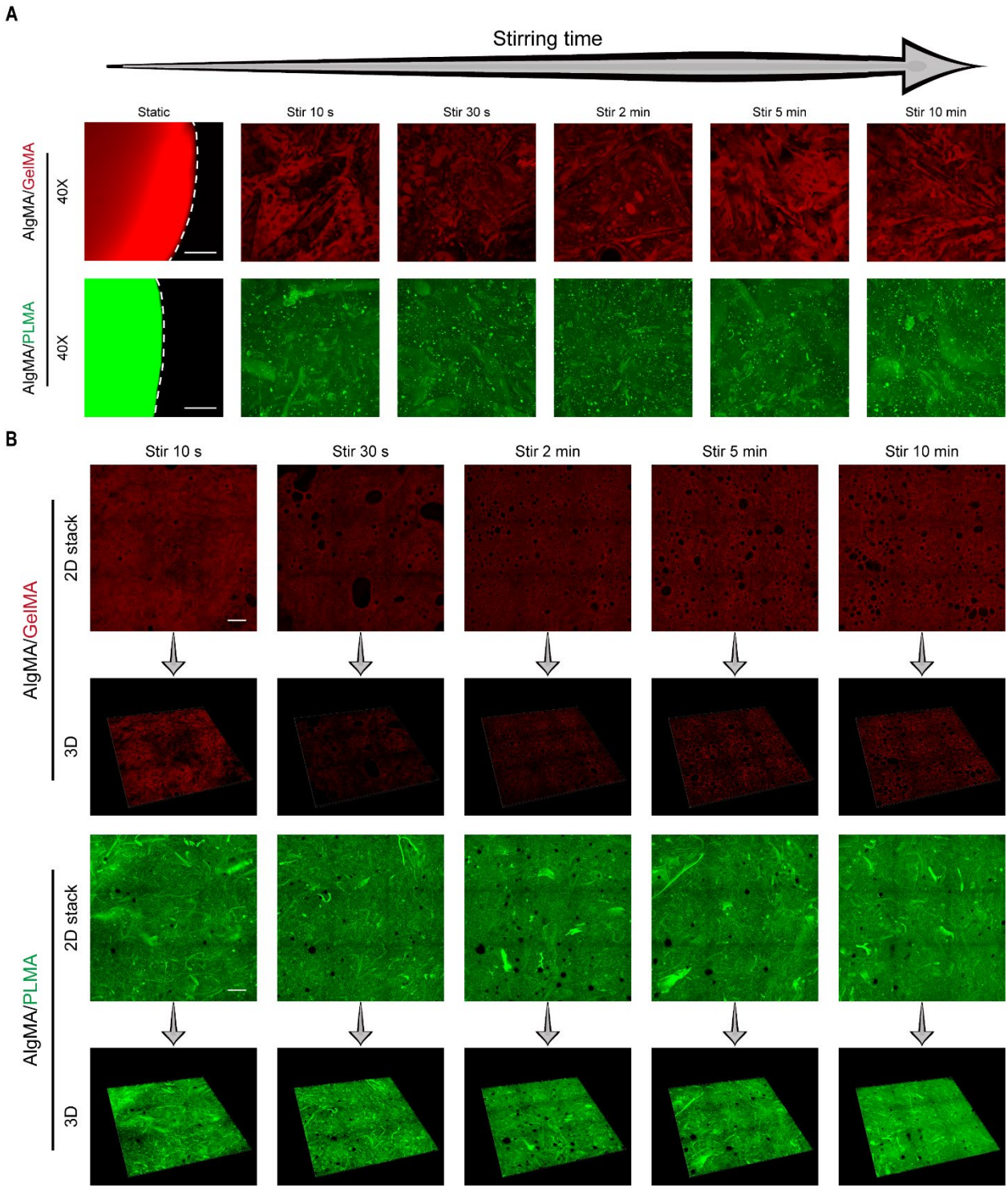

Figure S5. The Comparison of Mixing Behavior between AlgMA/GelMA and AlgMA/ε-PLMA Ink. A) Mixing of AlgMA/GelMA ink and AlgMA/ε-PLMA ink with different stirring time. Scale bar in **A**, 100 μm. **B)** Large view of the mixture of AlgMA/GelMA ink and AlgMA/ε-PLMA ink. Scale bar in **B**, 400 μm.

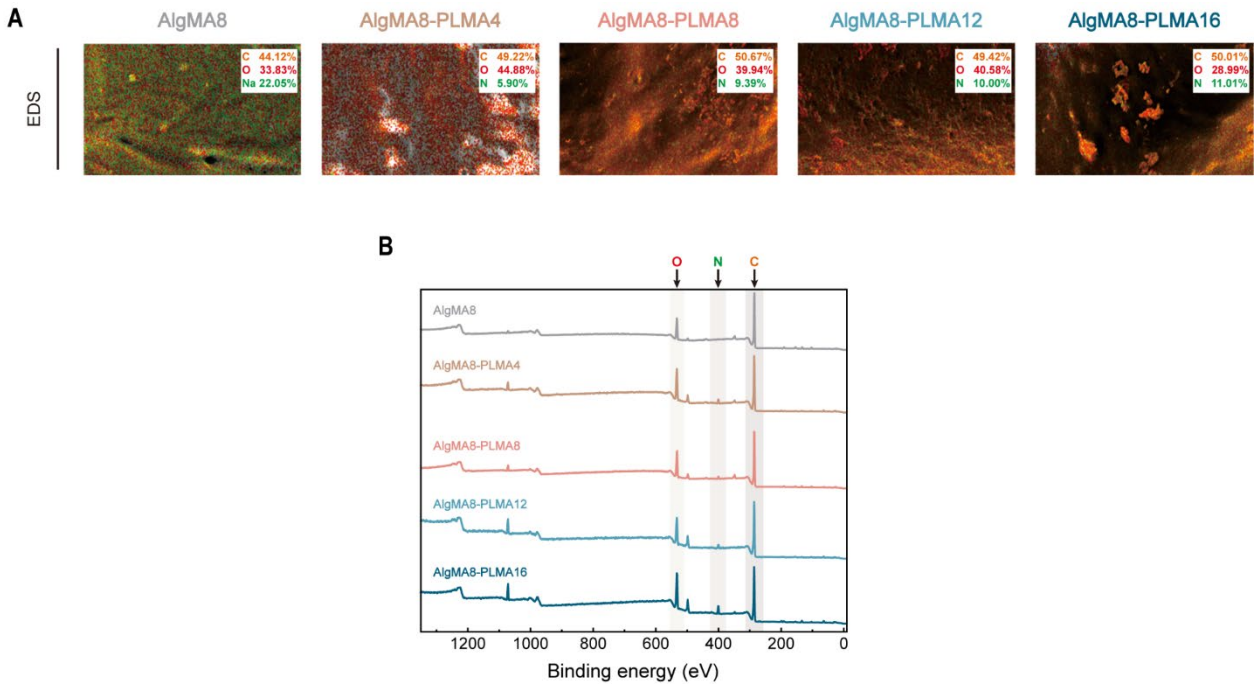

Figure S6. The Elements on Different Ratio of AlgMA/ε-PLMA Material Surface. A) EDS measurement of different ratio of AlgMA/ε-PLMA. **B)** High-resolution spectra of XPS detection for different ratio of AlgMA/ε-PLMA.

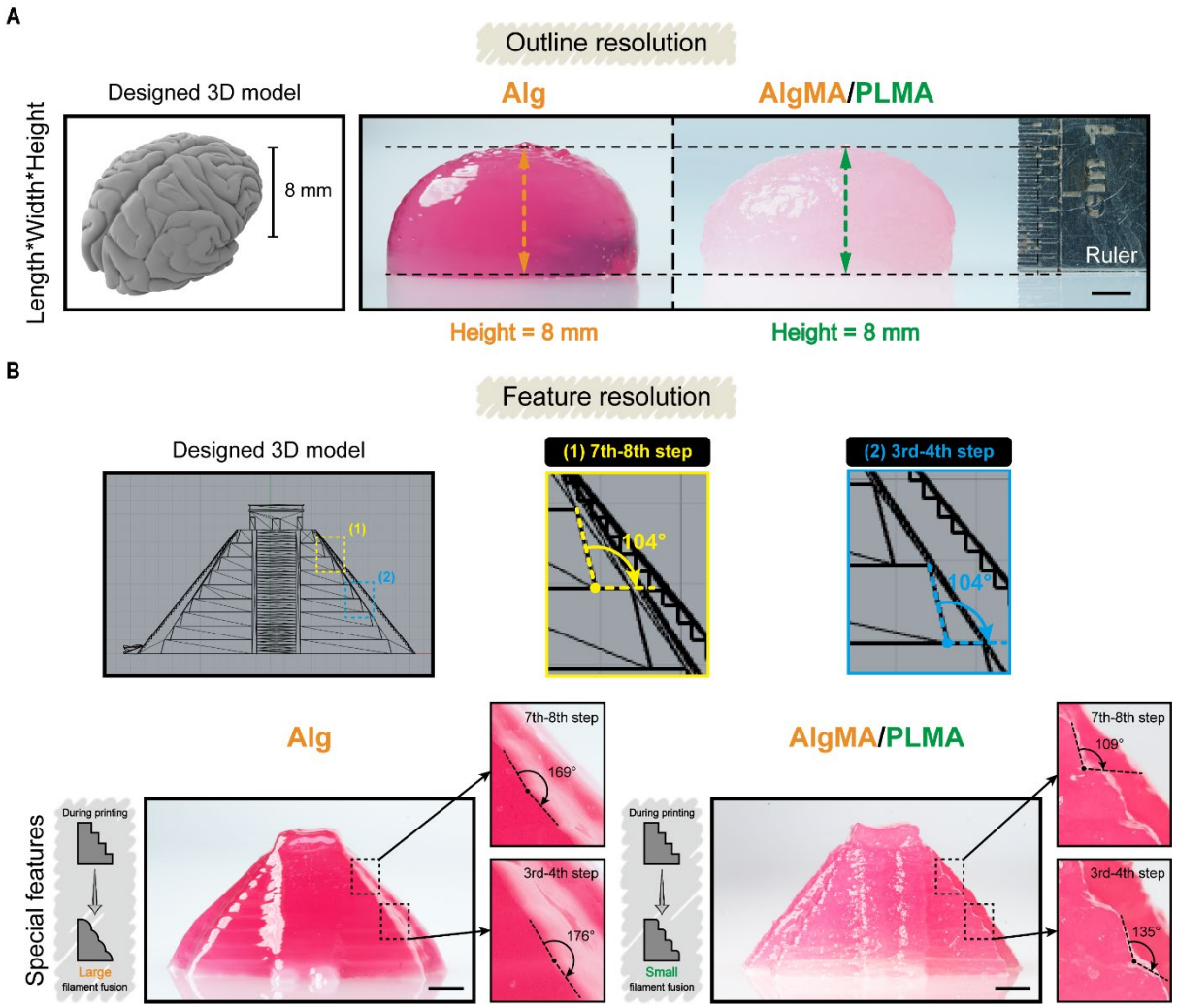

Figure S7. The 3D Printed Structures with Different Resolutions. A) The mimetic brains were printed via Alg ink and AlgMA/PLMA ink to demonstrate the printing Outline resolution. **B)** The steps of the printed pyramid were analyzed to demonstrate the printing Feature resolution. Scale bar, 2.5 mm.

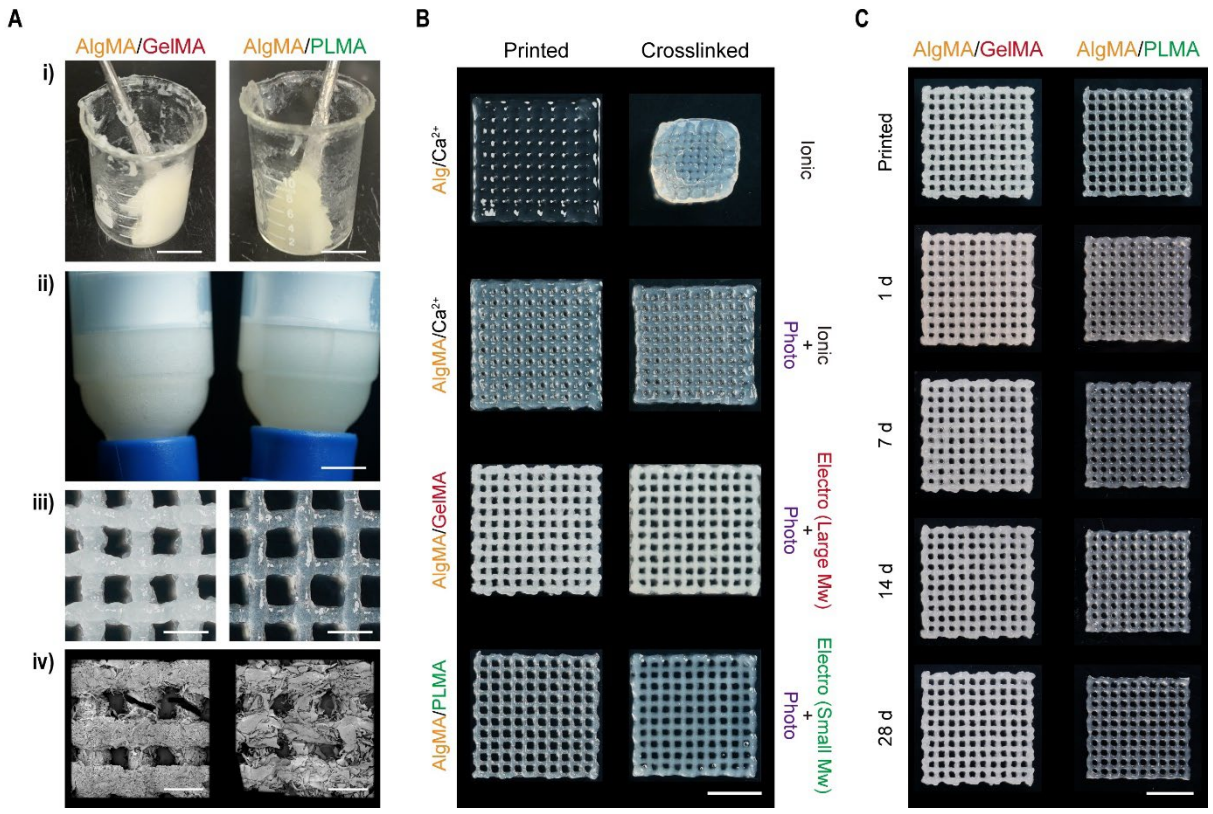

Figure S8. The Comparison between Traditional Alg-based Ink and AlgMA/ε-PLMA Ink. A) i) Preparation of AlgMA/GelMA ink and AlgMA/ε-PLMA ink. Scale bar in **i**, 1 cm. **ii)** Loading and outlook of well-prepared AlgMA/GelMA ink and AlgMA/ε-PLMA ink. Scale bar in **ii**, 5 mm. **iii)** The optical surface of AlgMA/GelMA filaments and AlgMA/ε-PLMA filaments. **iv)** The SEM surface of AlgMA/GelMA filaments and AlgMA/ε-PLMA filaments. Scale bar in **iii** and **iv**, 1 mm. **B)** The shape changing of different crosslinking methods. (Some pictures of **Panel B** have been shown in **Figure 2C**.) **C)** Shape changing of AlgMA/GelMA and AlgMA/ε-PLMA scaffolds during long-time immersion in PBS. Scale bar in **B** and **C**, 5 mm.

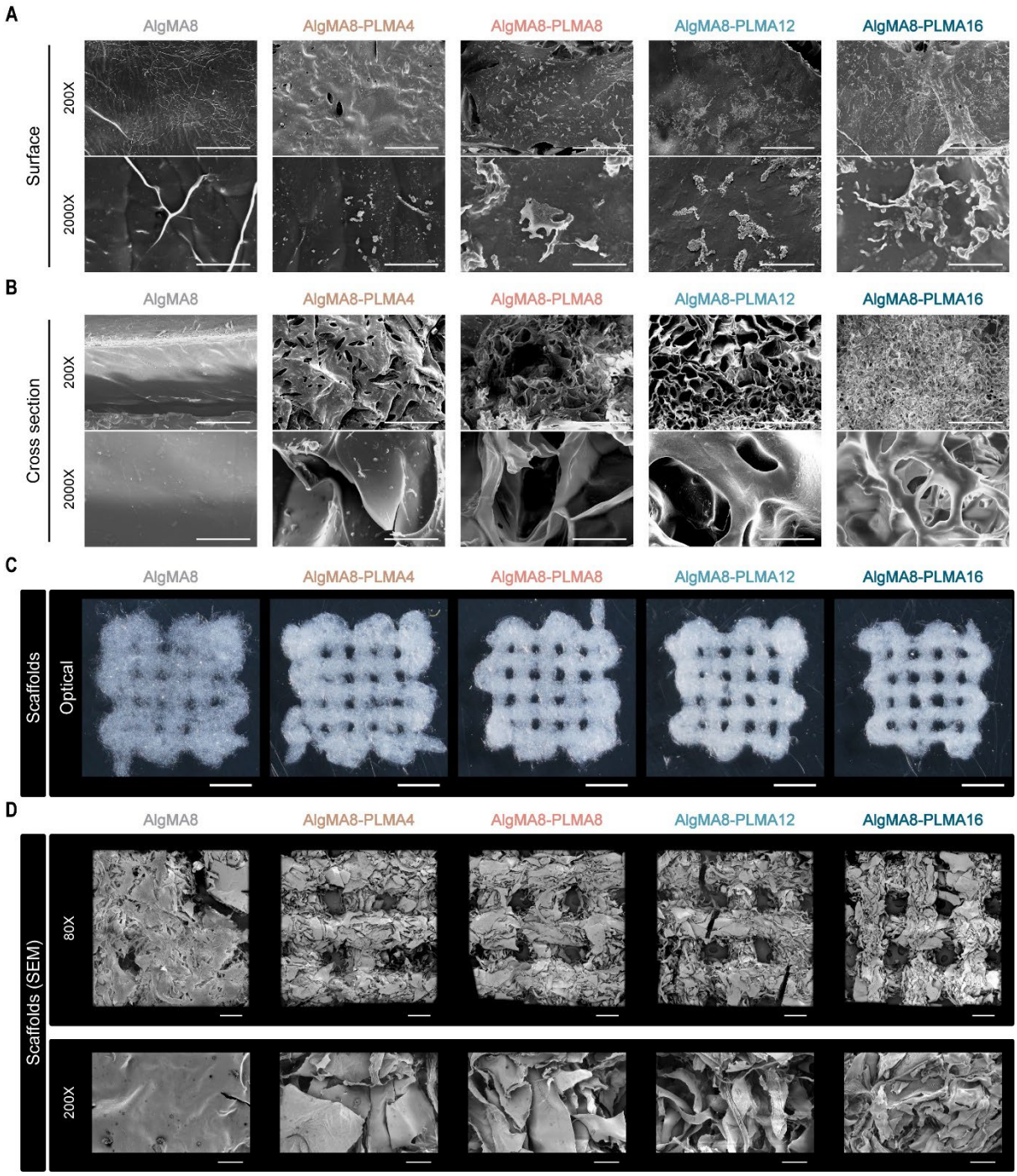

Figure S9. The SEM and Optical Images of Different Ratios of AlgMA/PLMA Materials. A) Surface morphology. **B)** Cross section morphology. "200X" represents magnification of 200 times (scale bar is 200 μm), "2000X" represents magnification of 2000 times (scale bar is 20 μm). **C)** The optical images of AlgMA/PLMA series scaffolds. Scale bar, 2 mm. **D)** The SEM images of AlgMA/PLMA series scaffolds. Scale bars for "80X" and "200X" are 500 μm and 100 μm, respectively. Some data have been shown in **Figure S8A**.

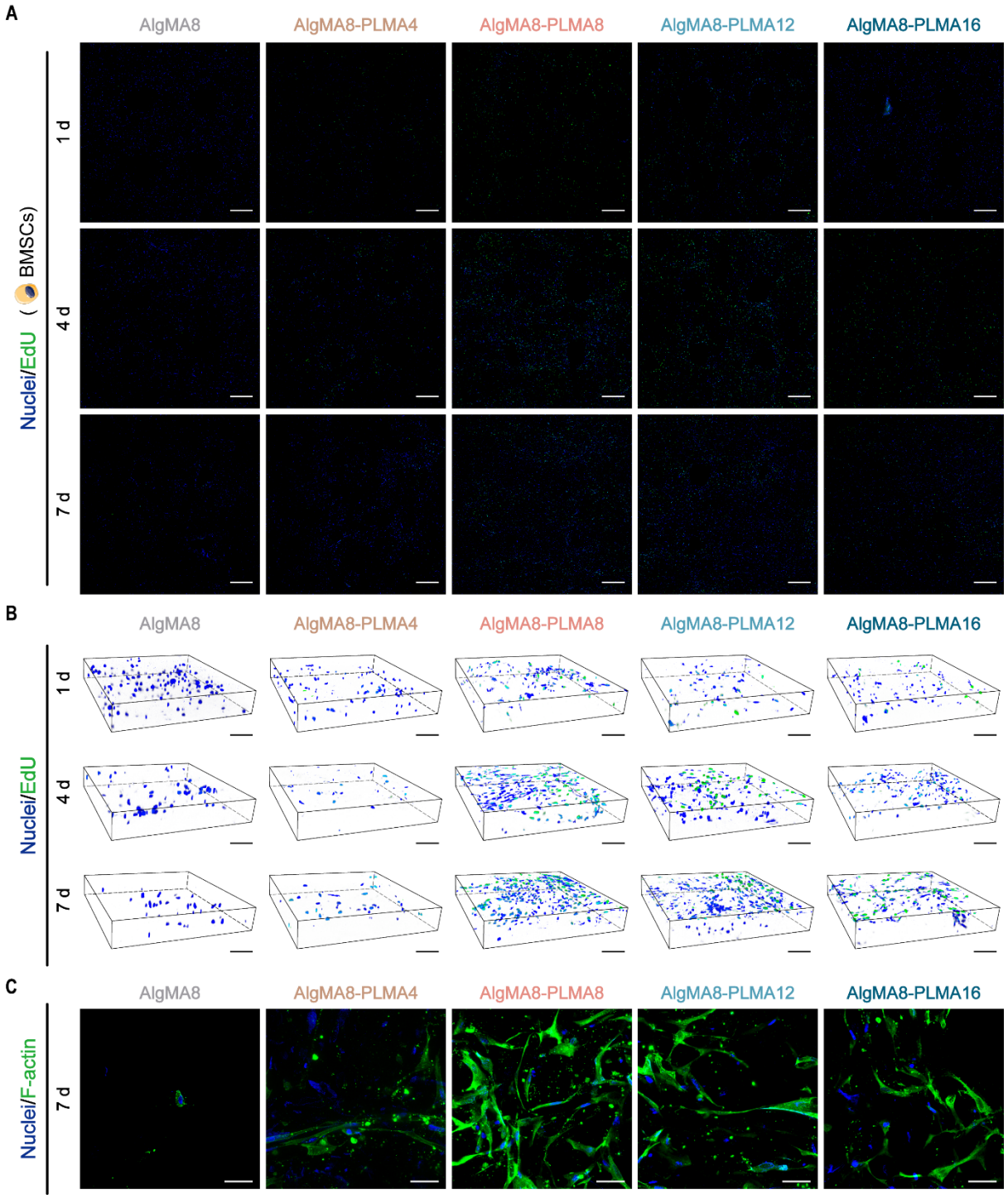

Figure S10. The Proliferation and Spreading of BMSCs in AlgMA/PLMA Series Scaffolds. A) and B) Cell proliferation on day 1, 4 and 7 (**A**, z-stacked images, scale bar, 400 μm; **B**, 3D views, scale bar, 100 μm) (green: EdU; blue: Nuclei). **C)** BMSC morphologies in different ratio of AlgMA/PLMA scaffolds on day 7 (green: F-actin; blue: nucleus). Scale bar, 50 μm. Some data have been shown in **Figure 11**.

Content of AlgMA (w/v)	Content of ε-PLMA (w/v)				
	0 %	**4 %**	**8 %**	**12 %**	**16 %**
0 %	—	PLMA4	PLMA8	PLMA12	PLMA16
4 %	AlgMA4	AlgMA4 -PLMA4	AlgMA4 -PLMA8	AlgMA4 -PLMA12	AlgMA4 -PLMA16
8 %	AlgMA8	AlgMA8 -PLMA4	AlgMA8 -PLMA8	AlgMA8 -PLMA12	AlgMA8 -PLMA16
12 %	AlgMA12	AlgMA12 -PLMA4	AlgMA12 -PLMA8	AlgMA12 -PLMA12	AlgMA12 -PLMA16
16 %	AlgMA16	AlgMA16 -PLMA4	AlgMA16 -PLMA8	AlgMA16 -PLMA12	AlgMA16 -PLMA16

Table S1. Preparation of AlgMA/PLMA hydrogels with varied concentrations.

Cell density: 2×10^6/ml		Printing speed (mm/s)					
		AlgMA8	AlgMA8 -PLMA4	AlgMA8 -PLMA8	AlgMA8 -PLMA12	AlgMA8 -PLMA16	AlgMA8 -GelMA8
Printing pressure (kPa)	45	3.5	6.0	4.0	3.0	2.2	0.6
	60	5.0	9.0	8.0	4.0	3.0	1.5
	80	9.0	14.5	14.0	6.0	4.5	3.0
	100	14.0	19.0	18.0	8.0	7.0	4.5

Table S2. The printing speed of bioinks under given printing pressure (25 °C).

References

[1] J.N. Katz, K.R. Arant, R.F. Loeser, Diagnosis and Treatment of Hip and Knee Osteoarthritis: A Review, JAMA 325(6) (2021) 568-578.

[2] J. Martel-Pelletier, A.J. Barr, F.M. Cicuttini, P.G. Conaghan, C. Cooper, M.B. Goldring, S.R. Goldring, G. Jones, A.J. Teichtahl, J.-P. Pelletier, Osteoarthritis, Nature Reviews Disease Primers 2 (2016) 16072.

[3] J. Martel-Pelletier, L.M. Wildi, J.-P. Pelletier, Future therapeutics for osteoarthritis, Bone 51 (2012) 297–311.

[4] V.B. Kraus, F.J. Blanco, M. Englund, M.A. Karsdal, L.S. Lohmander, Call for standardized definitions of osteoarthritis and risk stratification for clinical trials and clinical use, Osteoarthritis Cartilage 23(8) (2015) 1233-41.

[5] T.D. Spector, C. Cooper, Radiographic assessment of osteoarthritis in population studies: whither Kellgren and Lawrence?, Osteoarthritis and Cartilage 1 (1993) 203-206.

[6] E. Yusuf, R.G. Nelissen, A. Ioan-Facsinay, V. Stojanovic-Susulic, J. DeGroot, G.v. Osch, S. Middeldorp, T.W.J. Huizinga, M. Kloppenburg, Association between weight or body mass index and hand osteoarthritis: a systematic review, Annals of the Rheumatic Diseases 69 (2010) 761–765.

[7] C. Ding, O. Stannus, F. Cicuttini, B. Antony, G. Jones, Body fat is associated with increased and lean mass with decreased knee cartilage loss in older adults: a prospective cohort study, International Journal of Obesity 37 (2013) 822–827.

[8] Y. Wang, J.A. Simpson, A.E. Wluka, A.J. Teichtahl, D.R. English, G.G. Giles, S. Graves, F.M. Cicuttini, Relationship between body adiposity measures and risk of primary knee and hip

replacement for osteoarthritis: a prospective cohort study, Arthritis Research & Therapy 11(2) (2009) R31.

[9] G. Jones, C. Ding, M. Glisson, K. Hynes, D. Ma, F. Cicuttini, Knee Articular Cartilage Development in Children: A Longitudinal Study of the Effect of Sex, Growth, Body Composition, and Physical Activity, Pediatric Research 54 (2003) 230–236.

[10] B. Vanwanseele, H.K. F. Eckstein, E.S. A. Spaepen, Longitudinal analysis of cartilage atrophy in the knees of patients with spinal cord injury, Arthritis & Rheumatism 48(12) (2003) 3377–3381.

[11] Y. Wang, J.A. Simpson, A.E. Wluka, A.J. Teichtahl, D.R. English, G.G. Giles, S. Graves, F.M. Cicuttini, Is Physical Activity a Risk Factor for Primary Knee or Hip Replacement Due to Osteoarthritis? A Prospective Cohort Study, The Journal of Rheumatology 38(2) (2011) 350-357.

[12] T.L. Racunica, A.J. Teichtahl, Y. Wang, A.E. Wluka, D.R. English, G.G. Giles, R. O'Sullivan, F.M. Cicuttini, Effect of physical activity on articular knee joint structures in community-based adults, Arthritis Care & Research 57(7) (2007) 1261–1268.

[13] A.J. Teichtahl, Y. Wang, S. Heritier, A.E. Wluka, B.J. Strauss, J. Proietto, J.B. Dixon, G. Jones, F.M. Cicuttini, The interaction between physical activity and amount of baseline knee cartilage, Rheumatology 55(7) (2016) 1277–1284.

[14] T. T, W.-K. M, W. W, M. J, L. A, Development and remodeling of the hip joint of preterm neonates in sonographic evaluation, Ortopedia, Traumatologia, Rehabilitacja 5(6) (2003) 703-711.

[15] A.S. Nicholls, A. Kiran, T.C.B. Pollard, D.J. Hart, C.P.A. Arden, T. Spector, H.S. Gill, D.W. Murray, A.J. Carr, N.K. Arden, The association between hip morphology parameters and nineteen-year risk of end-stage osteoarthritis of the hip: A nested case–control study, Arthritis & Rheumatism 63(11) (2011) 3392–3400.

[16] K.A. Siebenrock, F. Ferner, P.C. Noble, R.F. Santore, S. Werlen, T.C. Mamisch, The Cam-type Deformity of the Proximal Femur Arises in Childhood in Response to Vigorous Sporting Activity, Clinical Orthopaedics and Related Research 469(11) (2011) 3229-3240.

[17] K.A. Siebenrock, I. Kaschka, L. Frauchiger, S. Werlen, J.M. Schwab, Prevalence of Cam-Type Deformity and Hip Pain in Elite Ice Hockey Players Before and After the End of Growth, The American Journal of Sports Medicine 41(10) (2013) 2308–2313.

[18] R. Agricola, M.P. Heijboer, A.Z. Ginai, P. Roels, A.A. Zadpoor, J.A.N. Verhaar, H. Weinans, J.H. Waarsing, A Cam Deformity Is Gradually Acquired During Skeletal Maturation in Adolescent and Young Male Soccer Players: A Prospective Study With Minimum 2-Year Follow-up, The American Journal of Sports Medicine 42(4) (2014) 798-806.

[19] K.A. Siebenrock, A. Behning, C.T. Mamisch, J.M. Schwab, Growth Plate Alteration Precedes Cam-type Deformity in Elite Basketball Players, Clinical Orthopaedics and Related Research 471(4) (2013) 1084-1091.

[20] L.K. Jensen, Hip osteoarthritis: influence of work with heavy lifting, climbing stairs or ladders, or combining kneeling/squatting with heavy lifting, Occupational & Environmental Medicine 65 (2008) 6-19.

[21] A.J. Teichtahl, S. Smith, Y. Wang, A.E. Wluka, R. O'Sullivan, G.G. Giles, F.M. Cicuttini, Occupational risk factors for hip osteoarthritis are associated with early hip structural abnormalities: a 3.0 T magnetic resonance imaging study of community-based adults, Arthritis Research & Therapy 17 (2015) 19.

[22] C. Bijkerk, J.J. Houwing-Duistermaat, H.A. Valkenburg, I. Meulenbelt, A. Hofman, F.C. Breedveld, H.A.P. Pols, C.M.V. Duijn, P.E. Slagboom, Heritabilities of radiologic osteoarthritis in

peripheral joints and of disc degeneration of the spine, Arthritis & Rheumatism 42(8) (1999) 1729-1735.

[23] T.D. Spector, J. Loughlin, Genetic influences on osteoarthritis in women: a twin study, British Medical Journal 312 (1996) 940–943.

[24] G. Zhai, J. Stankovich, C. Ding, F. Scott, F. Cicuttini, G. Jones, The genetic contribution to muscle strength, knee pain, cartilage volume, bone size, and radiographic osteoarthritis: A sibpair study, Arthritis & Rheumatism 50(3) (2004) 805-810.

[25] C. Rodriguez-Fontenla, M. Calaza, E. Evangelou, A.M. Valdes, N. Arden, F.J. Blanco, A. Carr, K. Chapman, P. Deloukas, M. Doherty, T. Esko, C.M.G. Aletá, J.J.G.-R. Carnota, H. Helgadottir, A. Hofman, I. Jonsdottir, H.J.M. Kerkhof, M. Kloppenburg, A. McCaskie, E.E. Ntzani, W.E.R. Ollier, N. Oreiro, K. Panoutsopoulou, S.H. Ralston, Y.F. Ramos, J.A. Riancho, F. Rivadeneira, P.E. Slagboom, U. Styrkarsdottir, U. Thorsteinsdottir, G. Thorleifsson, A. Tsezou, A.G. Uitterlinden, G.A. Wallis, J.M. Wilkinson, G. Zhai, Y. Zhu, t.a. Consortium, D.T. Felson, J.P.A. Ioannidis, J. Loughlin, A. Metspalu, I. Meulenbelt, K. Stefansson, J.B.v. Meurs, E. Zeggini, T.D. Spector, A. Gonzalez, Assessment of Osteoarthritis Candidate Genes in a Meta-Analysis of Nine Genome-Wide Association Studies, Arthritis & Rheumatology 66(4) (2014) 940-949.

[26] H. Guo, S.A. Maher, P.A. Torzilli, A biphasic finite element study on the role of the articular cartilage superficial zone in confined compression, Journal of Biomechanics 48(1) (2015) 166-170.

[27] T.P. Andriacchi, J. Favre, The Nature of In Vivo Mechanical Signals That Influence Cartilage Health and Progression to Knee Osteoarthritis, Current Rheumatology Reports 16 (2014) 463.

[28] R.E. Wilusz, J. Sanchez-Adams, F. Guilak, The structure and function of the pericellular matrix of articular cartilage, Matrix Biology 39 (2014) 25-32.

[29] R.F. Loeser, Integrins and chondrocyte–matrix interactions in articular cartilage, Matrix Biology 39 (2013) 11-16.

[30] L. Xu, I. Golshirazian, B.J. Asbury, Y. Li, Induction of high temperature requirement A1, a serine protease, by TGF-beta1 in articular chondrocytes of mouse models of OA, Histology and Histopathology 29 (2014) 609-618.

[31] D.B. Burr, M.B. Schaffler, The involvement of subchondral mineralized tissues in osteoarthrosis: Quantitative microscopic evidence, Microscopy Research and Technique 37(4) (1998) 343-357.

[32] I. H, S. I, C.C. Grampp S, Y. S, K. F, Subchondral Bone and Cartilage Disease: A Rediscovered Functional Unit, Investigative Radiology 35(10) (2000) 581-588.

[33] D.B. Burr, Anatomy and physiology of the mineralized tissues: Role in the pathogenesis of osteoarthrosis, Osteoarthritis and Cartilage 12 (2004) 20-30.

[34] D.A. Walsh, D.F. McWilliams, M.J. Turley, M.R. Dixon, R.E. Fransès, P.I. Mapp, D. Wilson, Angiogenesis and nerve growth factor at the osteochondral junction in rheumatoid arthritis and osteoarthritis, Rheumatology 49(10) (2010) 1852–1861.

[35] S. Suri, D.A. Walsh, Osteochondral alterations in osteoarthritis, Bone 51(2) (2012) Bone.

[36] T.S. L S Lohmander, D K Heinegård, Release of cartilage oligomeric matrix protein (COMP) into joint fluid after knee injury and in osteoarthritis, Annals of the Rheumatic Diseases 53 (1994) 8-13.

[37] A.J. Fosang, F. Beier, Emerging Frontiers in cartilage and chondrocyte biology, Best Practice & Research Clinical Rheumatology 25(6) (2011) 751-766.

[38] M. Wang, E.R. Sampson, H. Jin, J. Li, Q.H. Ke, H.-J. Im, D. Chen, MMP13 is a critical target

gene during the progression of osteoarthritis, Arthritis Research & Therapy 15 (2013) R5.

[39] M. Goldring, M. Otero, D. Plumb, C. Dragomir, M. Favero, K.E. Hachem, K. Hashimoto, H. Roach, E. Olivotto, R. Borzì, K. Marcu, Roles of inflammatory and anabolic cytokines in cartilage metabolism: signals and multiple effectors converge upon MMP-13 regulation in osteoarthritis, European Cells & Materials 21 (2011) 202-220.

[40] K.B. Marcu, M. Otero, E. Olivotto, R.M. Borzi, M.B. Goldring, NF-κB Signaling: Multiple Angles to Target OA, Current Drug Targets 11(5) (2010) 599 - 613.

[41] R.F. Loeser, Aging and osteoarthritis: the role of chondrocyte senescence and aging changes in the cartilage matrix, Osteoarthritis and Cartilage 17(8) (2009) 971-979.

[42] L.J. Sandell, Etiology of osteoarthritis: genetics and synovial joint development, Nature Reviews Rheumatology 8 (2012) 77–89.

[43] S.L. Dallas, M. Prideaux, L.F. Bonewald, The Osteocyte: An Endocrine Cell … and More, Endocrine Reviews 34(5) (2013) 658–690.

[44] S.R. Goldring, Role of Bone in Osteoarthritis Pathogenesis, Medical Clinics of North America 93(1) (2009) 25-35.

[45] M.B. Goldring, S.R. Goldring, Articular cartilage and subchondral bone in the pathogenesis of osteoarthritis, Skeletal Biology and Medicine 1192(1) (2010) 230-237.

[46] D.B. Burr, M.A. Gallant, Bone remodelling in osteoarthritis, Nature Reviews Rheumatology 8 (2012) 665–673.

[47] S.R. Goldring, The Role of Bone in Osteoarthritis Pathogenesis, Rheumatic Disease Clinics of North America 34(2) (2008) 561-571.

[48] J.-P. Raynauld, J. Martel-Pelletier, M.-J. Berthiaume, F. Abram, D. Choquette, B. Haraoui, J.F.

Beary, G.A. Cline, J.M. Meyer, J.-P. Pelletier, Correlation between bone lesion changes and cartilage volume loss in patients with osteoarthritis of the knee as assessed by quantitative magnetic resonance imaging over a 24-month period, Annals of the Rheumatic Diseases 67(5) (2008) 683-688.

[49] F.C. Ko, C. Dragomir, D.A. Plumb, S.R. Goldring, T.M. Wright, M.B. Goldring, M.C.H.v.d. Meulen, In Vivo Cyclic Compression Causes Cartilage Degeneration and Subchondral Bone Changes in Mouse Tibiae, Arthritis & Rheumatism 65(6) (2013) 1569-1578.

[50] B. Poulet, R.W. Hamilton, S. Shefelbine, A.A. Pitsillides, Characterizing a novel and adjustable noninvasive murine joint loading model, Arthritis & Rheumatology 63(1) (2011) 137-147.

[51] T.D. Brown, E.L. Radin, R.B. Martin, D.B. Burr, Finite element studies of some juxtarticular stress changes due to localized subchondral stiffening, Journal of Biomechanics 17(1) (1984) 11-21, 23-24.

[52] E. Radin, R. Rose, Role of subchondral bone in the initiation and progression of cartilage damage, Clinical Orthopaedics and Related Research 213 (1986) 34-40.

[53] J.S. Day, M. Ding, J.C.v.d. Linden, I. Hvid, D.R. Sumner, H. Weinans, A decreased subchondral trabecular bone tissue elastic modulus is associated with pre-arthritic cartilage damage, Journal of Orthopaedic Research 19(5) (2001) 914-918.

[54] J.S. Day, Adaptation of subchondral bone in osteoarthritis, Biorheology 41 (2004) 359–368.

[55] C.R. Scanzello, S.R. Goldring, The role of synovitis in osteoarthritis pathogenesis, Bone 51(2) (2012) 249-257.

[56] J.-P. Pelletier, J.-P. Raynauld, F.R.C.P.C., F. Abram, B. Haraoui, D. Choquette, J. Martel-

Pelletier, A new non-invasive method to assess synovitis severity in relation to symptoms and cartilage volume loss in knee osteoarthritis patients using MRI, Osteoarthritis and Cartilage 16(s3) (2008) S8-S13.

[57] F.W. Roemer, A. Guermazi, D.T. Felson, J. Niu, M.C. Nevitt, M.D. Crema, J.A. Lynch, C.E. Lewis, J. Torner, Y. Zhang, Presence of MRI-detected joint effusion and synovitis increases the risk of cartilage loss in knees without osteoarthritis at 30-month follow-up: the MOST study, Annals of the Rheumatic Diseases 70 (2011) 1804-1809.

[58] D.T. Felson, J. Niu, T. Neogi, J. Goggins, M.C. Nevitt, F. Roemer, J. Torner, C.E. Lewis, A. Guermazi, Synovitis and the risk of knee osteoarthritis: the MOST Study, Osteoarthritis and Cartilage 24(3) (2016) 458-464.

[59] K. Baker, A. Grainger, J. Niu, M. Clancy, A. Guermazi, M. Crema, L. Hughes, J. Buckwalter, A. Wooley, M. Nevitt, D.T. Felson, Relation of synovitis to knee pain using contrast-enhanced MRIs, Annals of the Rheumatic Diseases 69 (2010) 1779-1783.

[60] R.F. Loeser, S.R. Goldring, C.R. Scanzello, M.B. Goldring, Osteoarthritis: A disease of the joint as an organ, Arthritis & Rheumatology 64(6) (2012) 1697-1707.

[61] S.Y. Ritter, R. Subbaiah, G. Bebek, J. Crish, C.R. Scanzello, B. Krastins, D. Sarracino, M.F. Lopez, M.K. Crow, T. Aigner, M.B. Goldring, S.R. Goldring, D.M. Lee, R. Gobezie, A.O. Aliprantis, Proteomic Analysis of Synovial Fluid From the Osteoarthritic Knee: Comparison With Transcriptome Analyses of Joint Tissues, Arthritis & Rheumatism 65(4) (2013) 981-992.

[62] M. Kapoor, J. Martel-Pelletier, D. Lajeunesse, J.-P. Pelletier, H. Fahmi, Role of proinflammatory cytokines in the pathophysiology of osteoarthritis, Nature Reviews Rheumatology 7 (2011) 33–42.

[63] Q. Wang, A.L. Rozelle, C.M. Lepus, C.R. Scanzello, J.J. Song, D.M. Larsen, J.F. Crish, G. Bebek, S.Y. Ritter, T.M. Lindstrom, I. Hwang, H.H. Wong, L. Punzi, A. Encarnacion, M. Shamloo, S.B. Goodman, T. Wyss-Coray, S.R. Goldring, N.K. Banda, J.M. Thurman, R. Gobezie, M.K. Crow, V.M. Holers, D.M. Lee, W.H. Robinson, Identification of a central role for complement in osteoarthritis, Nature Medicine 17 (2011) 1674–1679.

[64] C.R. Scanzello, E. Umoh, F. Pessler, C. Diaz-Torne, T. Miles, E. DiCarlo, H.G. Potter, L. Mandl, R. Marx, S. Rodeo, S.R. Goldring, M.K. Crow, Local cytokine profiles in knee osteoarthritis: elevated synovial fluid interleukin-15 differentiates early from end-stage disease, Osteoarthritis and Cartilage 17(8) (2009) 1040–1048.

[65] C.R. Scanzello, B. McKeon, B.H. Swaim, E. DiCarlo, E.U. Asomugha, V. Kanda, A. Nair, D.M. Lee, J.C. Richmond, J.N. Katz, M.K. Crow, S.R. Goldring, Synovial inflammation in patients undergoing arthroscopic meniscectomy: Molecular characterization and relationship to symptoms, Arthritis & Rheumatology 63(2) (2011) 391-400.

[66] K. Takebe, M.F. Rai, E.J. Schmidt, L.J. Sandell, The chemokine receptor CCR5 plays a role in post-traumatic cartilage loss in mice, but does not affect synovium and bone, Osteoarthritis and Cartilage 23(3) (2015) 454-461.

[67] J. Cuellar, G. Scuderi, V. Cuellar, S. Golish, D. Yeomans, Diagnostic utility of cytokine biomarkers in the evaluation of acute knee pain, J. Bone Joint Surg. Am. 91 (2009) 2313–2320.

[68] X. Wang, D. Hunter, J. Xu, C. Ding, Metabolic triggered inflammation in osteoarthritis, Osteoarthritis and Cartilage 23(1) (2015) 22-30.

[69] O.P. Stannus, Y. Cao, B. Antony, L. Blizzard, F. Cicuttini, G. Jones, C. Ding, Cross-sectional and longitudinal associations between circulating leptin and knee cartilage thickness in older adults,

Annals of the Rheumatic Diseases 74 (2015) 82–88.

[70] J. Martel-Pelletier, J.-P. Raynauld, M. Dorais, F. Abram, J.-P. Pelletier, The levels of the adipokines adipsin and leptin are associated with knee osteoarthritis progression as assessed by MRI and incidence of total knee replacement in symptomatic osteoarthritis patients: a post hoc analysis, Rheumatology 55(4) (2016) 680–688.

[71] J.-P. Raynauld, J.-P. Pelletier, C. Roubille, M. Dorais, F. Abram, W. Li, Y. Wang, J. Fairley, F.M. Cicuttini, J. Martel-Pelletier, Magnetic Resonance Imaging–Assessed Vastus Medialis Muscle Fat Content and Risk for Knee Osteoarthritis Progression: Relevance From a Clinical Trial, Arthritis Care & Research 67(10) (2015) 1406-1415.

[72] A.J. Teichtahl, A.E. Wluka, Y. Wang, P.N. Wijethilake, B.J. Strauss, J. Proietto, J.B. Dixon, G. Jones, A. Forbes, F.M. Cicuttini, Vastus medialis fat infiltration – a modifiable determinant of knee cartilage loss, Osteoarthritis and Cartilage 23(12) (2015) 2150-2157.

[73] K. Ching, X. Houard, F. Berenbaum, C. Wen, Hypertension meets osteoarthritis — revisiting the vascular aetiology hypothesis, Nature Reviews Rheumatology 17 (2021) 533-549.

[74] R.A.D. Lorenzo, J.A. Ward, B.S. Jordan, C.E. Hanson, Relationships of Intraosseous and Systemic Pressure Waveforms in a Swine Model, Academic Emergency Medicine 21(8) (2014) 899-904.

[75] M. Beverly, D. Murray, Factors affecting intraosseous pressure measurement, Journal of Orthopaedic Surgery and Research 13 (2018) 187.

[76] R.K. Aaron, J.P. Dyke, D.M. Ciombor, D. Ballon, J. Lee, E. Jung, G.A. Tung, Perfusion Abnormalities in Subchondral Bone Associated with Marrow Edema, Osteoarthritis, and Avascular Necrosis, Annals of the New York Academy of Sciences 1117(1) (2007) 124–137.

[77] T. Kiær, B. Dahl, G.S. Lausten, The relationship between inert gas wash-out and radioactive tracer microspheres in measurement of bone blood flow: Effect of decreased arterial supply and venous congestion on bone blood flow in an animal model, Journal of Orthopaedic Research 11(1) (1993) 28-35.

[78] A. Jaiprakash, I. Prasadam, J.Q. Feng, Y. Liu, R. Crawford, Y. Xiao, Phenotypic Characterization of Osteoarthritic Osteocytes from the Sclerotic Zones: A Possible Pathological Role in Subchondral Bone Sclerosis, International Journal of Biological Sciences 8(3) (2012) 406-417.

[79] G. Zhen, C. Wen, X. Jia, Y. Li, J.L. Crane, S.C. Mears, F.B. Askin, F.J. Frassica, W. Chang, J. Yao, J.A. Carrino, A. Cosgarea, D. Artemov, Q. Chen, Z. Zhao, X. Zhou, L. Riley, P. Sponseller, M. Wan, W.W. Lu, X. Cao, Inhibition of TGF-β signaling in mesenchymal stem cells of subchondral bone attenuates osteoarthritis, Nature Medicine 19 (2013) 704–712.

[80] F. Intema, H.A.W. Hazewinkel, D. Gouwens, J.W.J. Bijlsma, H. Weinans, F.P.J.G. Lafeber, S.C. Mastbergen, In early OA, thinning of the subchondral plate is directly related to cartilage damage: results from a canine ACLT-meniscectomy model, Osteoarthritis and Cartilage 18(5) (2010) 691-698.

[81] S. Priam, C. Bougault, X. Houard, M. Gosset, C. Salvat, F. Berenbaum, C. Jacques, Identification of Soluble 14-3-3∈ as a Novel Subchondral Bone Mediator Involved in Cartilage Degradation in Osteoarthritis, Arthritis & Rheumatism 65(7) (2013) 1831-1842.

[82] F. Fernandez-Madrid, R.L. Karvonen, R.A. Teitge, P.R. Miller, W.G. Negendank, MR features of osteoarthritis of the knee, Magnetic Resonance Imaging 12(5) (1994) 703-709.

[83] A. Vallée, B.L. Lévy, J. Blacher, Interplay between the renin-angiotensin system, the canonical

WNT/β-catenin pathway and PPARγ in hypertension, Current Hypertension Reports 20 (2018) 62.

[84] S.-J. Kim, D.-S. Im, S.-H. Kim, J.-H. Ryu, S.-G. Hwang, J.-K. Seong, C.-H. Chun, J.-S. Chun, β-Catenin regulates expression of cyclooxygenase-2 in articular chondrocytes, Biochemical and Biophysical Research Communications 296(1) (2002) 221-226.

[85] K.J. Catt, P.Z. Zimmet, M.D. Cain, E. Cran, J.B. Best, J.P. Coghlan, Angiotensin II Blood-levels in Human Hypertension, The Lancet 297(7697) (1971) 459-464.

[86] M. Paul, A.P. Mehr, R. Kreutz, Physiology of Local Renin-Angiotensin Systems, Physiological Reviews 86(3) (2006) 747-803.

[87] R.M. Touyz, E.L. Schiffrin, Role of endothelin in human hypertension, Canadian Journal of Physiology and Pharmacology 81(6) (2003) 533–541.

[88] Z. Li, Z. Lin, S. Liu, H. Yagi, X. Zhang, L. Yocum, M. Romero-Lopez, C. Rhee, M.J. Makarcyzk, I. Yu, E.N. Li, M.R. Fritch, Q. Gao, K.B. Goh, B. O'Donnell, T. Hao, P.G. Alexander, B. Mahadik, J.P. Fisher, S.B. Goodman, B.A. Bunnell, R.S. Tuan, H. Lin, Human Mesenchymal Stem Cell-Derived Miniature Joint System for Disease Modeling and Drug Testing, Adv Sci (Weinh) 9(21) (2022) e2105909.

[89] Y.P. Singh, J.C. Moses, N. Bhardwaj, B.B. Mandal, Overcoming the Dependence on Animal Models for Osteoarthritis Therapeutics - The Promises and Prospects of In Vitro Models, Adv Healthc Mater 10(20) (2021) e2100961.

[90] C. Mondadori, S. Palombella, S. Salehi, G. Talo, R. Visone, M. Rasponi, A. Redaelli, V. Sansone, M. Moretti, S. Lopa, Recapitulating monocyte extravasation to the synovium in an organotypic microfluidic model of the articular joint, Biofabrication 13(4) (2021) 045001.

[91] M.R. Nelson, D. Ghoshal, J.C. Mejias, D.F. Rubio, E. Keith, K. Roy, A multi-niche

microvascularized human bone marrow (hBM) on-a-chip elucidates key roles of the endosteal niche in hBM physiology, Biomaterials 270 (2021) 120683.

[92] M. Rothbauer, G. Holl, C. Eilenberger, S.R.A. Kratz, B. Farooq, P. Schuller, I. Olmos Calvo, R.A. Byrne, B. Meyer, B. Niederreiter, S. Kupcu, F. Sevelda, J. Holinka, O. Hayden, S.F. Tedde, H.P. Kiener, P. Ertl, Monitoring tissue-level remodelling during inflammatory arthritis using a three-dimensional synovium-on-a-chip with non-invasive light scattering biosensing, Lab on a chip 20(8) (2020) 1461-1471.

[93] L. Banh, K.K. Cheung, M.W.Y. Chan, E.W.K. Young, S. Viswanathan, Advances in organ-on-a-chip systems for modelling joint tissue and osteoarthritic diseases, Osteoarthritis Cartilage 30(8) (2022) 1050-1061.

[94] S.K. O'Connor, D.B. Katz, S.J. Oswald, L. Groneck, F. Guilak, Formation of Osteochondral Organoids from Murine Induced Pluripotent Stem Cells, Tissue Eng Part A 27(15-16) (2021) 1099-1109.

[95] M. Au, Z. Liu, L. Rong, Y. Zheng, C. Wen, Endothelin-1 induces chondrocyte senescence and cartilage damage via endothelin receptor type B in a post-traumatic osteoarthritis mouse model, Osteoarthritis and Cartilage 28(12) (2020) 1559-1571.

[96] M.W.A. Kleuskens, J.F. Crispim, C.C. van Donkelaar, R.P.A. Janssen, K. Ito, Evaluating Initial Integration of Cell-Based Chondrogenic Constructs in Human Osteochondral Explants, Tissue Eng Part C Methods 28(1) (2022) 34-44.

[97] Z. Lin, Z. Li, E.N. Li, X. Li, C.J. Del Duke, H. Shen, T. Hao, B. O'Donnell, B.A. Bunnell, S.B. Goodman, P.G. Alexander, R.S. Tuan, H. Lin, Osteochondral Tissue Chip Derived From iPSCs: Modeling OA Pathologies and Testing Drugs, Front Bioeng Biotechnol 7 (2019) 411.

[98] C. O'Connor, E. Brady, Y. Zheng, E. Moore, K.R. Stevens, Engineering the multiscale complexity of vascular networks, Nature Reviews Materials 3 (2022) 1-15.

[99] M.A. Skylar-Scott, J. Mueller, C.W. Visser, J.A. Lewis, Voxelated soft matter via multimaterial multinozzle 3D printing, Nature 575(7782) (2019) 330-335.

[100] D.B. Kolesky, K.A. Homan, M.A. Skylar-Scott, J.A. Lewis, Three-dimensional bioprinting of thick vascularized tissues, Proceedings of the National Academy of Sciences of the United States of America 113(12) (2016) 3179-3184.

[101] M.A. Skylar-Scott, J.Y. Huang, A. Lu, A.H.M. Ng, T. Duenki, S. Liu, L.L. Nam, S. Damaraju, G.M. Church, J.A. Lewis, Orthogonally induced differentiation of stem cells for the programmatic patterning of vascularized organoids and bioprinted tissues, Nature Biomedical Engineering 6(4) (2022) 449-462.

[102] J.S. Miller, K.R. Stevens, M.T. Yang, B.M. Baker, D.H. Nguyen, D.M. Cohen, E. Toro, A.A. Chen, P.A. Galie, X. Yu, R. Chaturvedi, S.N. Bhatia, C.S. Chen, Rapid casting of patterned vascular networks for perfusable engineered three-dimensional tissues, Nature materials 11(9) (2012) 768-774.

[103] I.S. Kinstlinger, S.H. Saxton, G.A. Calderon, K.V. Ruiz, D.R. Yalacki, P.R. Deme, J.E. Rosenkrantz, J.D. Louis-Rosenberg, F. Johansson, K.D. Janson, D.W. Sazer, S.S. Panchavati, K.D. Bissig, K.R. Stevens, J.S. Miller, Generation of model tissues with dendritic vascular networks via sacrificial laser-sintered carbohydrate templates, Nature Biomedical Engineering 4(9) (2020) 916–932.

[104] B. Grigoryan, S.J. Paulsen, D.C. Corbett, D.W. Sazer, C.L. Fortin, A.J. Zaita, P.T. Greenfield, N.J. Calafat, J.P. Gounley, A.H. Ta, F. Johansson, A. Randles, J.E. Rosenkrantz, J.D. Louis-

Rosenberg, P.A. Galie, K.R. Stevens, J.S. Miller, Multivascular networks and functional intravascular topologies within biocompatible hydrogels, Science 364(6439) (2019) 458–464.

[105] N. Brandenberg, M.P. Lutolf, In Situ Patterning of Microfluidic Networks in 3D Cell-Laden Hydrogels, Advanced Materials 28(34) (2016) 7450-7456.

[106] M. Nikolaev, O. Mitrofanova, N. Broguiere, S. Geraldo, D. Dutta, Y. Tabata, B. Elci, N. Brandenberg, I. Kolotuev, N. Gjorevski, H. Clevers, M.P. Lutolf, Homeostatic mini-intestines through scaffold-guided organoid morphogenesis, Nature 585(7826) (2020) 574-578.

[107] P. Jiang, Z. Ji, D. Liu, S. Ma, X. Wang, F. Zhou, Growing Hydrogel Organ Mannequins with Interconnected Cavity Structures, Advanced Functional Materials 32(13) (2021) 2108845.

[108] T. Bhattacharjee, S.M. Zehnder, K.G. Rowe, S. Jain, R.M. Nixon, W.G. Sawyer, T.E. Angelini, Writing in the granular gel medium, Science Advances 1(8) (2015) e1500655.

[109] T.J. Hinton, Q. Jallerat, R.N. Palchesko, J.H. Park, M.S. Grodzicki, H.-J. Shue, M.H. Ramadan, A.R. Hudson, A.W. Feinberg, Three-dimensional printing of complex biological structures by freeform reversible embedding of suspended hydrogels, Science Advances 1(9) (2015) e1500758.

[110] W. Wu, A. DeConinck, J.A. Lewis, Omnidirectional printing of 3D microvascular networks, Advanced Materials 23(24) (2011) H178-H183.

[111] D.B. Kolesky, R.L. Truby, A.S. Gladman, T.A. Busbee, K.A. Homan, J.A. Lewis, 3D bioprinting of vascularized, heterogeneous cell-laden tissue constructs, Advanced Materials 26(19) (2014) 3124-3130.

[112] J.A. Brassard, M. Nikolaev, T. Hubscher, M. Hofer, M.P. Lutolf, Recapitulating macro-scale tissue self-organization through organoid bioprinting, Nature materials 20(1) (2021) 22-29.

[113] A.K. Miri, A. Khalilpour, B. Cecen, S. Maharjan, S.R. Shin, A. Khademhosseini, Multiscale bioprinting of vascularized models, Biomaterials 198 (2019) 204-216.

[114] Q. Dasgupta, L.D.B. III, A FRESH SLATE for 3D bioprinting, Science 365(6452) (2019) 446-447.

[115] M. Wang, W. Li, L.S. Mille, T. Ching, Z. Luo, G. Tang, C.E. Garciamendez, A. Lesha, M. Hashimoto, Y.S. Zhang, Digital Light Processing Based Bioprinting with Composable Gradients, Advanced Materials 34(1) (2022) e2107038.

[116] A. Lee, A.R. Hudson, D.J. Shiwarski, J.W. Tashman, T.J. Hinton, S. Yerneni, J.M. Bliley, P.G. Campbell, A.W. Feinberg, 3D bioprinting of collagen to rebuild components of the human heart, Science 365(6452) (2019) 482-487.

[117] Q. Gao, Y. He, J.Z. Fu, A. Liu, L. Ma, Coaxial nozzle-assisted 3D bioprinting with built-in microchannels for nutrients delivery, Biomaterials 61 (2015) 203-215.

[118] P. Occhetta, A. Mainardi, E. Votta, Q. Vallmajo-Martin, M. Ehrbar, I. Martin, A. Barbero, M. Rasponi, Hyperphysiological compression of articular cartilage induces an osteoarthritic phenotype in a cartilage-on-a-chip model, Nature Biomedical Engineering 3 (2019) 545–557.

[119] M.R. Nelson, D. Ghoshal, J.C. Mejías, D.F. Rubio, E. Keith, K. Roy, A multi-niche microvascularized human bone marrow (hBM) on-a-chip elucidates key roles of the endosteal niche in hBM physiology, Biomaterials 270 (2021).

[120] C. Mondadori, S. Palombella, S. Salehi, G. Talò, R. Visone, M. Rasponi, A. Redaelli, V. Sansone, M. Moretti, S. Lopa, Recapitulating monocyte extravasation to the synovium in an organotypic microfluidic model of the articular joint, Biofabrication 13(4) (2021).

[121] Z. Li, Z. Lin, S. Liu, H. Yagi, X. Zhang, L. Yocum, M. Romero-Lopez, C. Rhee, M.J.

Makarcyzk, I. Yu, E.N. Li, M.R. Fritch, Q. Gao, K.B. Goh, B. O'Donnell, T. Hao, P.G. Alexander, B. Mahadik, J.P. Fisher, S.B. Goodman, B.A. Bunnell, R.S. Tuan, H. Lin, Human Mesenchymal Stem Cell-Derived Miniature Joint System for Disease Modeling and Drug Testing, Advanced Science 9(21) (2022).

[122] T. Hodgkinson, D.C. Kelly, C.M. Curtin, F.J. O'Brien, Mechanosignalling in cartilage: an emerging target for the treatment of osteoarthritis, Nature Reviews Rheumatology 18 (2022) 67–84.

[123] R.L. Truby, J.A. Lewis, Printing soft matter in three dimensions, Nature 540(7633) (2016) 371-378.

[124] A.C. Daly, M.E. Prendergast, A.J. Hughes, J.A. Burdick, Bioprinting for the Biologist, Cell 184(1) (2021) 18-32.

[125] P. Wang, H. Rui, C. Gao, C. Wen, H. Pan, W. Liu, C. Ruan, W.W. Lu, Bioprinting living organs: The next milestone in organ transplantation?, The Innovation Life 1(2) (2023) 100019.

[126] N.E. Fedorovich, J.R. Dewijn, A.J. Verbout, J. Alblas, W.J.A. Dhert, Three-dimensional fiber deposition of cell-laden, viable, patterned constructs for bone tissue printing, Tissue Engineering Part A 14(1) (2008) 127-133.

[127] O. Jeon, Y. Bin Lee, T.J. Hinton, A.W. Feinberg, E. Alsberg, Cryopreserved cell-laden alginate microgel bioink for 3D bioprinting of living tissues, Mater Today Chem 12 (2019) 61-70.

[128] Y. Zhang, Y. Yu, A. Akkouch, A. Dababneh, F. Dolati, I.T. Ozbolat, In Vitro Study of Directly Bioprinted Perfusable Vasculature Conduits, Biomater Sci 3(1) (2015) 134-43.

[129] A. Schulz, M.M. Gepp, F. Stracke, H. von Briesen, J.C. Neubauer, H. Zimmermann, Tyramine-conjugated alginate hydrogels as a platform for bioactive scaffolds, J Biomed Mater Res

A 107(1) (2019) 114-121.

[130] J.A. Rowley, G. Madlambayan, D.J. Mooney, Alginate hydrogels as synthetic extracellular matrix materials, Biomaterials 20 (1999) 45—53.

[131] Q. Pi, S. Maharjan, X. Yan, X. Liu, B. Singh, A.M.v. Genderen, F. Robledo-Padilla, R. Parra-Saldivar, Ning Hu, W. Jia, C. Xu, J. Kang, S. Hassan, H. Cheng, X. Hou, A. Khademhosseini, Y.S. Zhang, Digitally Tunable Microfluidic Bioprinting of Multilayered Cannular Tissues, Advanced Materials 30(43) (2018) 1706913.

[132] G.L. Ying, N. Jiang, S. Maharjan, Y.X. Yin, R.R. Chai, X. Cao, J.Z. Yang, A.K. Miri, S. Hassan, Y.S. Zhang, Aqueous Two-Phase Emulsion Bioink-Enabled 3D Bioprinting of Porous Hydrogels, Adv Mater 30(50) (2018) e1805460.

[133] L. Ouyang, J.P.K. Armstrong, Y. Lin, J.P. Wojciechowski, C. Lee-Reeves, D. Hachim, K. Zhou, J.A. Burdick, M.M. Stevens, Expanding and optimizing 3D bioprinting capabilities using complementary network bioinks, Science Advances 6 (2020) eabc5529.

[134] A.P. Dhand, J.H. Galarraga, J.A. Burdick, Enhancing Biopolymer Hydrogel Functionality through Interpenetrating Networks, Trends in biotechnology 39(5) (2021) 519-538.

[135] U. Hersel, C. Dahmen, H. Kessler, RGD modified polymers: biomaterials for stimulated cell adhesion and beyond, Biomaterials 24(24) (2003) 4385-415.

[136] J.P. Gong, Y. Katsuyama, T. Kurokawa, Y. Osada, Double-Network Hydrogels with Extremely High Mechanical Strength, Advanced Materials 15(14) (2003) 1155-1158.

[137] W. Jia, P.S. Gungor-Ozkerim, Y.S. Zhang, K. Yue, K. Zhu, W. Liu, Q. Pi, B. Byambaa, M.R. Dokmeci, S.R. Shin, A. Khademhosseini, Direct 3D bioprinting of perfusable vascular constructs using a blend bioink, Biomaterials 106 (2016) 58-68.

[138] G. Kretzmer, K. Schiigerl, Response of mammalian cells to shear stress, Applied Microbiology and Biotechnology 34 (1991) 613–616.

[139] H. Nulwala, A. Mirjafari, X. Zhou, Ionic liquids and poly(ionic liquid)s for 3D printing – A focused mini-review, European Polymer Journal 108 (2018) 390-398.

[140] H. Wang, M.B. Hansen, D.W. Lowik, J.C. van Hest, Y. Li, J.A. Jansen, S.C. Leeuwenburgh, Oppositely charged gelatin nanospheres as building blocks for injectable and biodegradable gels, Adv Mater 23(12) (2011) H119-24.

[141] Z. Lin, M. Wu, H. He, Q. Liang, C. Hu, Z. Zeng, D. Cheng, G. Wang, D. Chen, H. Pan, C. Ruan, 3D Printing of Mechanically Stable Calcium-Free Alginate-Based Scaffolds with Tunable Surface Charge to Enable Cell Adhesion and Facile Biofunctionalization, Advanced Functional Materials 29(9) (2019) 1808439.

[142] K.S. Lim, J.H. Galarraga, X. Cui, G.C.J. Lindberg, J.A. Burdick, T.B.F. Woodfield, Fundamentals and Applications of Photo-Cross-Linking in Bioprinting, Chem Rev 120(19) (2020) 10662-10694.

[143] Q. Pi, S. Maharjan, X. Yan, X. Liu, B. Singh, A.M. van Genderen, F. Robledo-Padilla, R. Parra-Saldivar, N. Hu, W. Jia, C. Xu, J. Kang, S. Hassan, H. Cheng, X. Hou, A. Khademhosseini, Y.S. Zhang, Digitally Tunable Microfluidic Bioprinting of Multilayered Cannular Tissues, Adv Mater 30(43) (2018) e1706913.

[144] G. Tang, Z. Luo, L. Liana, J. Guo, S. Maharjan, C.E. Garciamendez-Mijares, M. Wang, W. Li, Z. Zhang, D. Wang, M. Xie, H. Ravanbakhsh, C. Zhou, X. Kuang, Y. Hou, X. Yu, Y.S. Zhang, Liquid-embedded (bio)printing of alginate-free, standalone, ultrafine, and ultrathin-walled cannular structures, Proceedings of the National Academy of Sciences 120(7) (2023) e2206762120.

[145] D. Wang, S. Maharjan, X. Kuang, Z. Wang, L.S. Mille, M. Tao, P. Yu, X. Cao, L. Lian, L. Lv, J.J. He, G. Tang, H. Yuk, C.K. Ozaki, X. Zhao, Y.S. Zhang, Microfluidic bioprinting of tough hydrogel-based vascular conduits for functional blood vessels, Science Advances 8 (2022) eabq6900.

[146] A. Schwab, R. Levato, M. D'Este, S. Piluso, D. Eglin, J. Malda, Printability and Shape Fidelity of Bioinks in 3D Bioprinting, Chem Rev 120(19) (2020) 11028-11055.

[147] Y.S. Zhang, G. Haghiashtiani, T. Hübscher, D.J. Kelly, J.M. Lee, M. Lutolf, M.C. McAlpine, W.Y. Yeong, M. Zenobi-Wong, J. Malda, 3D extrusion bioprinting, Nature Reviews Methods Primers 1(1) (2021).

[148] K. Song, A.M. Compaan, W. Chai, Y. Huang, Injectable Gelatin Microgel-Based Composite Ink for 3D Bioprinting in Air, ACS Applied Materials & Interfaces 12(20) (2020) 22453-22466.

[149] Q. Liang, F. Gao, Z. Zeng, J. Yang, M. Wu, C. Gao, D. Cheng, H. Pan, W. Liu, C. Ruan, Coaxial Scale-Up Printing of Diameter-Tunable Biohybrid Hydrogel Microtubes with High Strength, Perfusability, and Endothelialization, Advanced Functional Materials 30(43) (2020) 2001485.

[150] L. Ouyang, R. Yao, Y. Zhao, W. Sun, Effect of bioink properties on printability and cell viability for 3D bioplotting of embryonic stem cells, Biofabrication 8(3) (2016) 035020.

[151] O. Jeon, K.H. Bouhadir, J.M. Mansour, E. Alsberg, Photocrosslinked alginate hydrogels with tunable biodegradation rates and mechanical properties, Biomaterials 30(14) (2009) 2724-34.

[152] X. Wang, J. Qi, W. Zhang, Y. Pu, R. Yang, P. Wang, S. Liu, X. Tan, B. Chi, 3D-printed antioxidant antibacterial carboxymethyl cellulose/epsilon-polylysine hydrogel promoted skin wound repair, Int J Biol Macromol 187 (2021) 91-104.

[153] A.G. Tabriz, M.A. Hermida, N.R. Leslie, W. Shu, Three-dimensional bioprinting of complex cell laden alginate hydrogel structures, Biofabrication 7(4) (2015) 045012.

[154] L. Ouyang, Pushing the rheological and mechanical boundaries of extrusion-based 3D bioprinting, Trends in biotechnology 40(7) (2022) 891-902.

[155] J. Gong, C.C.L. Schuurmans, A.M.V. Genderen, X. Cao, W. Li, F. Cheng, J.J. He, A. Lopez, V. Huerta, J. Manriquez, R. Li, H. Li, C. Delavaux, S. Sebastian, P.E. Capendale, H. Wang, J. Xie, M. Yu, R. Masereeuw, T. Vermonden, Y.S. Zhang, Complexation-induced resolution enhancement of 3D-printed hydrogel constructs, Nat Commun 11(1) (2020) 1267.

[156] W. Liu, Y. Li, X. Ding, Cell adhesion pattern created by OSTE polymers, Biofabrication 9(2) (2017) 025006.

[157] H. Liu, Y. Wang, Y. Yu, W. Chen, L. Jiang, J. Qin, Simple fabrication of inner chitosan-coated alginate hollow microfiber with higher stability, J Biomed Mater Res B Appl Biomater 107(8) (2019) 2527-2536.

[158] R.A. Hartvig, M. van de Weert, J. Ostergaard, L. Jorgensen, H. Jensen, Protein adsorption at charged surfaces: the role of electrostatic interactions and interfacial charge regulation, Langmuir 27(6) (2011) 2634-43.

[159] F. Tan, X. Xu, T. Deng, M. Yin, X. Zhang, J. Wang, Fabrication of positively charged poly(ethylene glycol)-diacrylate hydrogel as a bone tissue engineering scaffold, Biomed Mater 7(5) (2012) 055009.

[160] J.H. Lee, G. Khang, J.W. Lee, H.B. Lee, Interaction of Different Types of Cells on Polymer Surfaces with Wettability Gradient, Journal of Colloid and Interface Science 205(2) (1998) 323-330.

[161] K. Webb, V. Hlady, P.A. Tresco, Relative importance of surface wettability and charged functional groups on NIH 3T3 fibroblast attachment, spreading, and cytoskeletal organization, Journal of Biomedical Materials Research 41(3) (1998) 422-430.

[162] Y. Arima, H. Iwata, Effect of wettability and surface functional groups on protein adsorption and cell adhesion using well-defined mixed self-assembled monolayers, Biomaterials 28(20) (2007) 3074-82.

[163] M. Mohammadalipour, M. Asadolahi, Z. Mohammadalipour, T. Behzad, S. Karbasi, Plasma surface modification of electrospun polyhydroxybutyrate (PHB) nanofibers to investigate their performance in bone tissue engineering, Int J Biol Macromol 230 (2023) 123167.

[164] T. Hyphantis, K. Kotsis, P.V. Voulgari, N. Tsifetaki, F. Creed, A.A. Drosos, Diagnostic accuracy, internal consistency, and convergent validity of the Greek version of the patient health questionnaire 9 in diagnosing depression in rheumatologic disorders, Arthritis Care Res (Hoboken) 63(9) (2011) 1313-1321.

[165] M.C. Laiguillon, A. Courties, X. Houard, M. Auclair, A. Sautet, J. Capeau, B. Feve, F. Berenbaum, J. Sellam, Characterization of diabetic osteoarthritic cartilage and role of high glucose environment on chondrocyte activation: toward pathophysiological delineation of diabetes mellitus-related osteoarthritis, Osteoarthritis Cartilage 23(9) (2015) 1513-22.

[166] A. Hernandez-Segura, J. Nehme, M. Demaria, Hallmarks of Cellular Senescence, Trends Cell Biol 28(6) (2018) 436-453.

[167] J.C. Rousseau, P.D. Delmas, Biological markers in osteoarthritis, Nat Clin Pract Rheumatol 3(6) (2007) 346-56.

[168] M. Takahashi, K. Naito, M. Abe, T. Sawada, A. Nagano, Relationship between radiographic

grading of osteoarthritis and the biochemical markers for arthritis in knee osteoarthritis, Arthritis Res Ther 6(3) (2004) R208-12.

[169] M. SHINOHARA, R. NISHIDA, T. AOYAMA, H. KAMONO, H. BANDO, M. NISHIZAWA, Comparison of guluronate contents of alginates determined by different methods, Fisheries science 66 (2000) 616–617.